

UC San Diego

UC San Diego Electronic Theses and Dissertations

Title

Constraining the Dust Direct Radiative Effect over Source Regions via Observations and Models

Permalink

<https://escholarship.org/uc/item/2rx8q1zz>

Author

Kuwano, Alexandra Meiko

Publication Date

2023

Peer reviewed|Thesis/dissertation

UNIVERSITY OF CALIFORNIA SAN DIEGO

Constraining the Dust Direct Radiative Effect over Source Regions via Observations and Models

A dissertation submitted in partial satisfaction of the
requirements for the degree Doctor of Philosophy

in

Oceanography

by

Alexandra Meiko Kuwano

Committee in charge:

Amato Evan, Chair
Sarah Aarons
Jennifer Burney
Robert Frouin
Kate Ricke

2023

Copyright

Alexandra Meiko Kuwano, 2023

All rights reserved.

The Dissertation of Alexandra Meiko Kuwano is approved, and it is acceptable in quality and form for publication on microfilm and electronically.

University of California San Diego

2023

TABLE OF CONTENTS

Dissertation Approval Page	iii
Table of Contents	iv
List of Figures	vi
List of Tables	x
List of Abbreviations	xi
List of Symbols	xiv
Acknowledgements	xvi
Vita	xvii
Abstract of the Dissertation	xviii
Chapter 1 Introduction	1
Chapter 2 A Method to Account for the Impact of Water Vapor on Observation-Based Estimates of the Clear-Sky Shortwave Direct Radiative Effect of Mineral Dust	5
2.1 Introduction	6
2.2 Data and Model	9
2.2.1 Data	9
2.2.2 Radiative Transfer Model	11
2.3 Background and Motivation	13
2.3.1 Old Method	13
2.3.2 Correlation in Dust and Water Vapor	14
2.3.3 New Method to Estimate the Forcing Efficiency	16
2.4 Evaluating the New Forcing Efficiency in an Idealized Framework	17
2.4.1 Linear Model	18
2.4.2 Two-stream model	21
2.4.3 Streamer Radiative Transfer Model	23
2.5 Sample Size and Forcing Efficiency Uncertainty	24
2.6 Application to Real Data	27
2.6.1 Instantaneous Forcing Efficiency	27
2.6.2 Comparison to Other Work	32
2.7 Conclusion	33
2.8 Appendix: A	38
2.8.1 Old Theory	38
2.8.2 New Theory	39

2.9	Appendix: B	40
2.9.1	Streamer Radiative Transfer Model	40
2.9.2	Forcing Efficiency	41
2.10	Acknowledgments	44
Chapter 3	Quantifying the Dust Direct Radiative Effect in the Southwestern United States: Findings from Novel Measurements	45
3.1	Introduction	46
3.2	Data Sets and Products	50
3.2.1	Field Site Description, Instruments, and Products	50
3.2.2	Satellite Data	60
3.2.3	Other Data Sets	62
3.2.4	Identifying Dust Events	63
3.2.5	Surface Soil Mineralogy	65
3.3	Radiative Transfer Model	66
3.4	Methods	76
3.4.1	Theory	78
3.4.2	Observational Method Description and Justification	79
3.4.3	Model Method Description	81
3.5	Results	82
3.5.1	Observation-based Shortwave Instantaneous Forcing Efficiency	82
3.5.2	Modeled Instantaneous Forcing Efficiency	85
3.5.3	Diurnally Averaged Forcing Efficiency	87
3.5.4	Comparison to Other Studies	89
3.6	Conclusion	97
3.7	Acknowledgements	101
3.8	Supplemental	102
Chapter 4	Conclusions	104
4.1	Summary of Key Findings and Novelty	104
4.2	Remaining Questions	107
	Glossary	109
	Bibliography	112

LIST OF FIGURES

Figure 2.1:	Temporally averaged vertical profiles of temperature (teal), mixing ratio (blue), and dust extinction coefficient (orange) at In Salah, Algeria for the summer months of July and August 2010–2015.	12
Figure 2.2:	The potential scatter between S^\uparrow and τ when a) $r_{\tau,q} < 0$ and b) $r_{\tau,q} > 0$, where τ increases to the right on the x-axis and S^\uparrow increases upwards on the y-axis. The potential linear fits of S^\uparrow as a function of τ are depicted by the blue dashed line when $r_{\tau,q} < 0$, the red dashed line when $r_{\tau,q} > 0$, and	15
Figure 2.3:	Correlation between atmospheric moisture and dust over northern Africa. Plotted in 2.3a is a map of the correlation coefficients $r_{\tau,q}$ for monthly mean values of aerosol optical depth and total precipitable water using data for the time period 2010–2018. Shown in 2.3b are similar correlation	16
Figure 2.4:	Plotted are the output from the (a) linear, (b) two-stream, and (c) Streamer idealized models showing the impact of a correlation between dust and water vapor on observational estimates of the forcing efficiency η . Shown is the model dust forcing efficiency η_t (black circles), the forcing efficiency	21
Figure 2.5:	Shown are estimates of the number of observations required to generate estimates of the dust forcing efficiency with uncertainty less than 10%, N_{10} , as a function of the correlation between dust and water vapor optical depth r_{τ_d,τ_q} for η_o (blue line) and η_n (red line). Values are constructed using output	25
Figure 2.6:	Maps of η_o estimated using τ and τ_d (a, c, respectively) and η_n estimated using τ and τ_d (b, d, respectively) for $\mu > 0.9$ (shading). The thin gray line indicates $\eta = 0$ and the grids enclosed by light gray boxes denote areas with undefined η values due to an insufficient number of available	28
Figure 2.7:	The a) spatially averaged η_o (red, open circle) and η_n (blue, closed circle) estimated with τ over the Sahara Desert as a function of the μ bin center for each μ interval. The η uncertainty for each μ interval are plotted in b) for the old (red, open circle) and new (blue, closed circle) methods. Also .	31
Figure 2.8:	Maps of (a) η_t , (b) η_o , and (c) η_n over all land grid-boxes within 8–38°N, 20°W–40°E. All of the estimated values of η ($\text{W m}^{-2}\tau^{-1}$) are represented by the same color scale. White depicts areas where the η is equal to the spatial mode of η_t ($-26.0 \text{ W m}^{-2}\tau^{-1}$).	41
Figure 2.9:	Shown is a (a) map of the η_o bias (colors, in $\text{W m}^{-2}\tau^{-1}$). The gray contour line indicates areas where the η_o bias is equal to zero. Also shown is a (b) scatter plot of the η_o bias ($\text{W m}^{-2}\tau^{-1}$) as a function of the correlation coefficient between τ and q ($r_{\tau,q}$).	42

Figure 2.10:	Shown is a (a) map of the η_n bias (colors, in $\text{W m}^{-2}\tau^{-1}$) with the same colorbar as Figure 2.9a. The gray contour line indicates where the η bias is equal to zero. Also shown is a (b) scatter plot of the η_n bias ($\text{W m}^{-2}\tau^{-1}$) as a function of the correlation coefficient between τ and q ($r_{\tau,q}$). Note that	43
Figure 3.1:	A map of (a) California and the (b) regions surrounding the Salton Sea. Also plotted is the location of the field site (white square). The red, yellow, green, and blue closed circles represent the locations of the monitoring stations Sonny Bono, Naval Test Base, Niland-English Road, and Salton	51
Figure 3.2:	The instrumentation available at the Scripps Institution of Oceanography (SIO) field site (white square, Figure 3.1) in the Salton Basin. The instruments marked with an “A” represent the radiometers (“1A” = CGR4 pyrgeometer, “2A” = CG4 pyrgeometer, and “3A” = CM21 pyranometer).	53
Figure 3.3:	A scatter plot of the GPS (y-axis) and AERONET (x-axis) retrieved q (cm) before the correction was applied to the AERONET retrieved q . The black, solid line represents the 1:1 ratio of GPS and AERONET q while the red, solid line is the best-fit line between AERONET and GPS q .	57
Figure 3.4:	Nadir-looking points of the CERES SSF data used in this study. Shown are CERES SSF footprints (blue, closed circles) within approximately 25 km (shaded white circle) of the field site (white square). Shown are 1302 data points during clear-sky and daytime conditions.	61
Figure 3.5:	Shown is a time series of the (a) backscatter BS profile generated from the CL51 Vaisala ceilometer at the SIO field site during a dust storm on April 22, 2022. Times enclosed by the magenta dashed rectangles are identified as being dusty. Also shown are time series of (b) f (c) AE , (d) τ , and (e)	64
Figure 3.6:	Roundshot images at (a) 6:10 PT, (b) 8:00 PT, and (c) 16:00 PT on April 22, 2022. Roundshot images are from a camera owned by the Imperial Irrigation District (IID) at the Anza-Borrego Station (accessed at: https://iid.roundshot.com/anza-borrego/#/), depicted as the	65
Figure 3.7:	NASA Worldview True Color imagery on April 22, 2022 from Aqua (~13:30 PT). World view images can be accessed at: https://worldview.earthdata.nasa.gov/ .	66
Figure 3.8:	Mineral abundances of the surface soil and dust, based on AVIRIS-C retrieved mineral abundance averaged over the polygon in Figure 3.1.	69
Figure 3.9:	Shown are plots of the (a) real n and (b) imaginary k parts of the dust CRI calculated from the AVIRIS-C surface soil mineralogy over the 0.4–15 μm spectral range.	70

Figure 3.10:	Dust single scatter properties used in RRTM and based on the <i>CRI</i> derived from AVIRIS-C (Figure 3.9). Plotted are the (a) single scatter albedo ω , (b) asymmetry parameter g , and (c) extinction coefficient β_e over the 0.4–15 μm spectral range.	71
Figure 3.11:	Shown is a scatter plot of the observed (y-axis) and modeled (x-axis) surface net SW flux. These simulations are run under clear-sky conditions with inputs obtained from 13 radiosonde launches during dust storms at the SIO field site from 2020–2022. The black line represents the 1:1 ratio.	73
Figure 3.12:	Shown is a scatter plot of the Observed (y-axis) and modeled (x-axis) surface LW net flux. These simulations are run under clear-sky conditions with inputs obtained from 13 radiosonde launches during dust storms at the SIO field site from 2020–2022. The black line represents the 1:1 ratio.	74
Figure 3.13:	Shown are scatter plots of the observed (y-axis) and modeled (x-axis) SW flux at the (a) surface (net) and (b) TOA (upward). Each model run is simulated under clear-sky and dusty conditions, as described in Sections 3.2.1 and 3.2.4, respectively. The black line represents the 1:1 ratio and all	75
Figure 3.14:	Shown are scatter plots of observed (y-axis) and modeled (x-axis) LW fluxes at the (a) surface (net) and (b) TOA (upward). All RRTM LW output are simulated under clear-sky and dusty conditions. The black line represents the 1:1 ratio and the colors represent AERONET retrieved τ at	77
Figure 3.15:	Shown are scatter plots of the observed (y-axis) and linearized (x-axis) SW flux at the (a) surface (net) and (b) TOA (upward). The black, solid-line represents the 1:1 ratio of the observed and linearized SW fluxes. All linearized and observed fluxes are collocated to AERONET measurements	80
Figure 3.16:	Observation (teal and orange) and model-based (blue) estimates of the clear-sky instantaneous SW η of dust at the surface (left), TOA (middle), and atmosphere (right). All observation-based estimates of SW η_∞ are estimated with the collocated satellite dataset (teal). For the surface, the teal	84
Figure 3.17:	Shown are the best estimates of the clear-sky instantaneous SW (a) ζ and (b) η of dust at the surface, TOA, and atmosphere. The abbreviations “OBS” and “RTM” represent the observational and model methods, respectively. All uncertainties are reported as the 95% confidence interval. The η_∞	85
Figure 3.18:	Shown are estimates of the clear-sky instantaneous LW η of dust at the surface (left), TOA (middle), and atmosphere (right) via the model method, described in Section 3.4.3. Error bars represent the 95% confidence interval of the instantaneous LW η	87

Figure 3.19:	Shown is the clear-sky annual and diurnally averaged SW (blue), LW (red), and net (teal) η of dust at the surface (left), TOA (middle), and atmosphere (right). Error bars represent the 95% confidence interval of η	89
Figure 3.20:	Shown are estimates of the clear-sky instantaneous SW η of dust at the surface (solid colored bar, solid line), TOA (clear bar, solid line), and atmosphere (solid colored bar, dashed-dot line) from this study (blue), Di Biagio et al. (2010) (orange), Di Sarra et al. (2013) (red), and Kuwano and	91
Figure 3.21:	Shown are estimates of the clear-sky instantaneous LW η (left) and ζ (right) of dust at the surface (solid colored bar, solid line), TOA (clear bar, solid line), and atmosphere (solid colored bar, dotted line) from this and other studies. Black, closed circles denote the locations of the various	94
Figure 3.22:	Clear-sky annual and diurnally averaged SW η at the surface (shaded colored bars, solid line), TOA (clear bars, solid line), and atmosphere (shaded colored bars, dot-dashed line) from this (blue) and other studies. Locations marked with an open black circle or black \times denote a surface . .	96
Figure 3.23:	Scatter plots of the observed surface SW downward flux (S^{\downarrow}) from the factory-calibrated pyranometer (y-axis, W m^{-2}) and the voltage output V from the field-calibrated pyranometer (x-axis, mV). Each color denotes the data during each calibration period (i.e. orange for the calibration period in	102
Figure 3.24:	Shown are scatter plots of the (a) voltage output V from the factory (y-axis) and field-calibrated (x-axis) pyrgeometers and the (b) body temperature of the factory (y-axis) and field-calibrated (x-axis) pyrgeometers during each calibration period. Each color denotes the data during each calibration . . .	103

LIST OF TABLES

Table 2.1:	Regional clear-sky TOA SW η of dust estimated with τ over the Sahara Desert from this and other studies.	34
Table 3.1:	<i>In-situ</i> (top) and space-borne (bottom) instrumentation with their corresponding measurements, retrievals, and uncertainties used in this study. ...	59
Table 3.2:	Days and start times for each radiosonde launch considered in RRTM SW and LW.....	103

LIST OF ABBREVIATIONS

ADM	Angular distribution model
AE	Angstrom exponent
AER	Atmospheric and Environmental Research
AERONET	Aerosol Robotic Network
AGL	Above ground level
AVIRIS-C	Airborne Visible Infrared Imaging Spectroradiometer - Classic
BS	Ceilometer backscatter
CERES	Clouds and Earth's Radiant Energy System
CRI	Complex Refractive Index
DISORT	Discrete Ordinate Radiative Transfer
DRE	Direct radiative effect
FE	Forcing efficiency
GEOS-5	Goddard Earth Observing System Model version 5.4.1
GMAO	Global Modeling and Assimilation Office
IID	Imperial Irrigation District

JMA	Japan Meteorological Agency
LBLRTM	Line-by-line radiative transfer model
LW	Longwave
MODIS	Moderate Resolution Imaging Spectroradiometer
NCAR	National Center for Atmospheric Research
NKX	Miramar MCAS (Joe Foss Field) airport
NPP	National polar-orbiting partnership
OLR	Outgoing longwave radiation
PM ₁₀	Particulate Matter less than 10 μ m
RH	Relative humidity
RMSE	Root-mean squared error
RTM	Radiative transfer model
SHADE	Sahara Dust Experiment
SIO	Scripps Institution of Oceanography
SSF	Single scanner footprint
SW	Shortwave

TAMUdust2020 Texas A&M University dust 2020 database

TOA Top of the Atmosphere

VIIRS Visible Infrared Imaging Radiometer Suite

LIST OF SYMBOLS

\uparrow	Upward flux (superscript)
\downarrow	Downward flux (superscript)
η	Forcing efficiency
μ	Cosine of the solar zenith angle
θ	Solar zenith angle
α	Surface albedo
σ	Standard deviation
λ	Wavelength
ζ	Direct radiative effect
ω	Single scatter albedo
τ	Aerosol optical depth
ε	Surface longwave emissivity
β_e	Extinction coefficient
A	Particle projected area
D	Dust particle diameter
P	Pressure
Q_e	Volume extinction coefficient
Q_s	Volume scattering coefficient
S	Shortwave flux
T	Temperature
f	Fine-mode fraction
f_c	Fractional abundances of clay in the soil
f_s	Fractional abundances of silt in the soil

g	Asymmetry parameter
k	Imaginary part of the complex refractive index
m_c	Soil mineral abundances of clay sizes
m_s	Soil mineral abundances of silt sizes
n	Real part of the complex refractive index
p	Pristine-sky (subscript)
q	Total precipitable water vapor
r	Correlation coefficient
$r_{\tau,q}$	Correlation coefficient between aerosol optical depth and total precipitable water
r_m	Ratio of mineral abundance
w	Water vapor mixing ratio
z	Height

ACKNOWLEDGEMENTS

I would like to extend my profound gratitude to all those who have supported me during the completion of my thesis. First and foremost, I would like to extend my deepest appreciation to my advisor and chair of my committee, Dr. Amato Evan, for his unwavering patience and support during these past six years. His mentorship and guidance have been instrumental in my growth as a scientist. I am also deeply grateful to my committee member, Dr. Robert Frouin, for his assistance in preparing and collecting data, specifically with surface observations, launching of weather balloons, and frequent maintenance of instrumentation at our field site. I would also like to acknowledge the invaluable guidance and support of my committee members: Dr. Sarah Aarons, thank you for your assistance with data collection; Dr. Jennifer Burney, your research insights and broader perspective have been invaluable to my research; Dr. Kate Ricke, I appreciate your newly joined expertise; and Dr. Dan Rubin, thank you for your helpful guidance regarding instrumentation.

I would like to acknowledge the countless contributions and support from Evan Lab members, both past and present, for frequent trips to the Salton Sea and for assistance with weather balloon launches and data collection.

Lastly, I would like to express my deepest gratitude to my parents, for their unconditional love and support, and to my friends, home and away, for their support.

Chapter 2, in part, is a reprint of the material as it appears in *Journal of Geophysical Research: Atmospheres*. Kuwano, A., and Evan, A. (2022). A method to account for the impact of water vapor on observation-based estimates of the clear-sky shortwave direct radiative effect of mineral dust. *Journal of Geophysical Research: Atmospheres*, 127 (17), doi:<https://doi.org/10.1029/2022JD036620>. The dissertation author was the primary author of this paper.

Chapter 3, in part, is currently being prepared for submission for publication of the material. A. M. Kuwano; A. T. Evan; B. C. Walkowiak; R. Frouin. The dissertation author was the primary investigator and author of this material.

VITA

- 2017 B.S. in Atmospheric Science, University of California, Davis
- 2019–2023 Teaching Assistant, Scripps Institution of Oceanography
University of California San Diego
- 2017–2023 Graduate Student Researcher, University of California San Diego
- 2023 Ph.D in Oceanography, University of California San Diego

PUBLICATIONS

“A method to account for the impact of water vapor on observation-based estimates of the clear-sky shortwave direct radiative effect of mineral dust.” *Journal of Geophysical Research: Atmospheres*, vol. 127, pp e2022JD036620, 2022

ABSTRACT OF THE DISSERTATION

Constraining the Dust Direct Radiative Effect over Source Regions via Observations and Models

by

Alexandra Meiko Kuwano

Doctor of Philosophy in Oceanography

University of California San Diego, 2023

Amato Evan, Chair

Mineral aerosols (i.e. dust) perturb the Earth's energy budget by scattering and absorbing shortwave (SW) and longwave (LW) radiation. Generally dust has a net (SW + LW) negative direct radiative effect (*DRE*) at the surface and top of the atmosphere (i.e. cooling of the Earth's climate system). A few studies found that the net top of the atmosphere (TOA) *DRE* of dust, the difference between the net radiative flux in clear-sky (cloud-free) and pristine-sky (aerosol and cloud free) conditions, can be near zero or positive over desert regions. It is important to constrain the net *DRE* of dust over source regions since biases in this parameter can lead to errors in estimates of the global average. In Chapter 2 an observation-based method to estimate the dust SW forcing efficiency (*FE*), the *DRE* normalized by the aerosol optical depth, is developed

and validated. Associated uncertainties in this method are further investigated. By accounting for the relationship between dust and water vapor, biases in the TOA SW *FE* of dust are reduced and estimates of the TOA SW *FE* of dust over the Sahara Desert range from -26.4 ± 17.6 to $2.35 \pm 139 \text{ W m}^{-2}$ per optical depth. In Chapter 3 this method is applied to observations and retrievals from a small dust source region in southeastern California to estimate the surface and TOA dust SW *FE*. These results are compared with the dust SW *FE* estimated with the output from a radiative transfer model. After validating the model, modeled and observed estimates of the instantaneous SW *FE* are statistically similar and therefore the model is used to estimate the instantaneous dust LW *FE* and the diurnally averaged net dust *FE*. Values of the net *FE* of dust are -29 ± 10 , -10 ± 11 , and $19 \pm 15 \text{ W m}^{-2}$ per optical depth at the surface, TOA, and atmosphere, respectively, over the small dust source region. The findings presented in this dissertation contribute towards the breadth of observational estimates of the SW dust *FE* over dust source regions which is critical to constrain model-based estimates of regional and global values of the dust SW *FE*.

Chapter 1

Introduction

Mineral aerosols (i.e. aeolian dust) reduce air quality and visibility in desert communities, which can lead to increased hospitalizations for asthma (Kanatani et al., 2010) or hazardous roads (e.g. Davis, 2017). Dust can also carry bacteria, viruses, or fungi over long distances (Weir-Brush, Garrison, Smith, & Shinn, 2004; Schweitzer et al., 2018; Pappagianis & Einstein, 1978) thereby affecting local terrestrial and ocean ecosystems. For example it has been theorized that dust storms increase the risk of acquiring Valley Fever (Tong, Wang, Gill, Lei, & Wang, 2017; Pappagianis & Einstein, 1978), a disease caused by fungi the *Coccidioides immitis* and *Coccidioides pasadasii* (Kollath, Mihaljevic, & Barker, 2022).

From a climate perspective dust is a source of iron and phosphorous in the ocean (Hand et al., 2004; Jickells et al., 2005; Moore & Braucher, 2008) and on land (Okin, Mahowald, Chadwick, & Artaxo, 2004; Das, Evan, & Lawrence, 2013), and thus has the potential to alter the global carbon cycle. Dust also affects the Earth's climate by altering the Earth's Energy budget. Dust directly affects the Earth's energy budget by scattering and absorbing shortwave (SW) and longwave (LW) radiation (Sokolik & Toon, 1996). Indirectly dust can alter cloud optical properties (i.e. cloud albedo) by acting as ice cloud condensation nuclei (DeMott et al., 2003; Sassen, DeMott, Prospero, & Poellot, 2003; DeMott et al., 2010). Dust semi-directly affects the Earth's energy budget by altering the atmospheric temperature profile (Johnson, Shine, & Forster, 2004) and as a result can change local atmospheric stability and dynamics. Changes to

local atmospheric stability can lead to conditions that favor or inhibit dust emission (Kok, 2011). These effects can be further exasperated in regions undergoing desertification (Mirzabaev et al., in press).

The main focus of this dissertation is the direct radiative effect *DRE* of dust, the difference between the net radiative flux in clear-sky (cloud-free) and pristine-sky (aerosol and cloud-free) conditions, in the SW and LW electromagnetic spectrums. Generally in the SW spectrum dust tends to induce a cooling effect at the surface and top of the atmosphere (TOA) by increasing the amount of solar radiation scattered to space and reducing the amount of solar radiation absorbed by the surface (Liao & Seinfeld, 1998). In the LW spectrum dust tends to induce a warming effect (Tegen, Lacis, & Fung, 1996) at the surface and TOA because dust reduces the amount of outgoing longwave radiation (OLR) at the TOA. Recent work has estimated the globally averaged SW and LW *DRE* of dust at the TOA to be -0.25 ± 0.22 and $0.22 \pm 0.15 \text{ W m}^{-2}$, respectively, which produces an overall negative net (SW + LW) TOA *DRE* of dust of -0.03 (-0.29 to 0.23) W m^{-2} (Di Biagio, Balkanski, Albani, Boucher, & Formenti, 2020). Yet the sign of the globally averaged net TOA *DRE* of dust is unconstrained (Di Biagio et al., 2020; Kok et al., 2017) and thus it is uncertain whether or not dust cools or warms the Earth's climate system. On a broader note the magnitude and sign of the dust *DRE* may potentially alter the magnitude and sign of the total aerosol forcing at the TOA, which is thought to primarily counteract much of the warming induced by greenhouse gases.

A reason that the sign and magnitude of the globally averaged net *DRE* of dust is unconstrained is due to the traditional methods to estimate and a shortage of observational estimates of the *DRE* of dust. In order to estimate the globally averaged net *DRE* of dust one must utilize a radiative transfer model (RTM) to estimate the spatial variation of LW and SW dust *DRE* across the globe (e.g. Song et al., 2022; Balkanski, Schulz, Claquin, & Guibert, 2007; Helmert, Heinold, Tegen, Hellmuth, & Wendisch, 2007; Highwood & Ryder, 2014). The inputs to such a model require knowledge of the microphysical and optical properties of dust, of which are highly uncertain and variable in space and time. For example the complex refractive index

must be retrieved for all wavelengths for which radiative transfer (RT) is simulated and is highly dependent on dust mineralogy (Scanza et al., 2015) that varies across source regions (Journet, Balkanski, & Harrison, 2014; Di Biagio et al., 2017; Di Biagio et al., 2019). As such, uncertain and inaccurate estimations of the complex refractive index can lead to biases in RTM output (L. Li et al., 2021) and high spatial variation in the complex refractive index can lead to high spatial variation in the dust *DRE*. Model-based estimations of dust *DRE* are also dependent on dust size. Kok et al. (2017) found that most global climate models classified dust as being smaller ($< 10\mu\text{m}$) than in reality, which led to under and overestimations of the magnitude of the LW and SW *DRE* of dust, respectively. Additionally there is a lack of understanding of the change in dust size distribution as dust is transported through the atmosphere (van der Does, Knippertz, Zschenderlein, Harrison, & Stuut, 2018). A lack of understanding of how dust size distribution changes in the vertical atmospheric column can lead to misclassifications of dust found downwind of dust source regions (Song et al., 2018). Another important factor is the asphericity of dust (Kandler et al., 2007) which can affect the retrieval of dust optical properties and representation of dust emission in models.

In order to avoid the uncertainties associated with using an RTM to estimate the dust *DRE*, several studies estimated the dust *DRE* with only observations and retrievals (e.g. Conant, 2000; Hsu, Herman, & Weaver, 2000; Di Biagio et al., 2009; Di Biagio, Di Sarra, & Meloni, 2010; Brindley, 2007; Kuwano & Evan, 2022). Challenges with estimating the SW and LW *DRE* solely from observations include instrumentation and retrieval error, uncertainty associated with dust being correlated with other atmospheric or environmental constituents, uncertainty associated with sample size, and limitations related to temporal and spatial resolution of measurements. In regards to the latter source of error most satellites with radiometric instrumentation are sun synchronous polar orbiting satellites that obtain measurements only twice a day (night + day) and at spatial resolutions within approximately 0.1–1 km. Radiometric data from geostationary satellites may be a reasonable alternative because the temporal resolution is higher; however, this data is often difficult to access, store, and work with. It is also challenging to estimate the LW

DRE of dust solely from observations and retrievals because LW fluxes are highly dependent on surface temperature, humidity, and the vertical distribution of temperature and dust (Zhang & Christopher, 2003; Brindley, 2007; Brindley & Russell, 2009; Hsu et al., 2000).

This dissertation is structured as follows. In Chapter 2 the uncertainties associated with an observational method to estimate the TOA SW *DRE* of dust (e.g. Satheesh & Ramanathan, 2000; Hsu et al., 2000; F. Li, Vogelmann, & Ramanathan, 2004) are investigated. Next we describe a modification to this method to estimate the TOA SW *DRE* of dust and apply the modified observation-based method to satellite observations over the Sahara Desert, one of Earth's major dust source regions (Goudie & Middleton, 2001). In Chapter 3 we apply this observational method and use RTM output to estimate the SW *DRE* of dust at the surface, TOA, and atmosphere over the western Sonoran Desert in southeastern California, an area that experiences frequent dust storms (A. T. Evan, 2019). The advantage to using both observations and an RTM to estimate the SW *DRE* of dust is that both methods are independent from one another and if we find statistically similar results then the RTM can be used to estimate the instantaneous LW *DRE* of dust and the diurnally averaged SW, LW, and net (LW + SW) *DRE* of dust. In Chapter 4 key findings from each chapter are highlighted and remaining questions from this work are summarized.

Chapter 2

A Method to Account for the Impact of Water Vapor on Observation-Based Estimates of the Clear-Sky Shortwave Direct Radiative Effect of Mineral Dust

The shortwave direct radiative effect of dust, the difference between net shortwave radiative flux in a cloud free and cloud and aerosol free atmosphere, is typically estimated using forward calculations made with a radiative transfer model. However, estimates of the direct radiative effect made via this initial method can be highly uncertain due to difficulty in accurately describing the relevant optical and physical properties of dust used in these calculations. An alternative approach to estimate this effect is to determine the forcing efficiency, or the direct radiative effect normalized by aerosol optical depth. While this approach avoids the uncertainties associated with the initial method for calculating the direct effect, random errors and biases associated with this approach have not been thoroughly examined in literature. Here we explore biases in this observation-based approach that are related to atmospheric water vapor. We use observations to show that over the Sahara Desert dust optical depth and column-integrated atmospheric water vapor are positively correlated. We use three idealized radiative models of varying complexity to demonstrate that a positive correlation between dust and water vapor produces a positive bias in the dust forcing efficiency estimated via the observation-based method. We describe a simple modification to the observation-based method that correctly accounts for

the correlation between dust and water vapor when estimating the forcing efficiency and use this method to estimate the instantaneous forcing efficiency of dust over the Sahara Desert using satellite data, obtaining -20.9 ± 11.9 to -12.3 ± 6.68 W m^{-2} per unit optical depth.

2.1 Introduction

Mineral aerosols (i.e., aeolian dust) are the most abundant aerosol by mass in the Earth's atmosphere and have a profound effect on the climate system. Dust directly affects the climate system by scattering and absorbing shortwave (SW) and longwave (LW) radiation (Sokolik & Toon, 1996). Dust also affects the climate system indirectly by acting as nuclei for the formation of ice clouds (DeMott et al., 2003; Sassen et al., 2003; DeMott et al., 2010). Deposited dust is a source of iron and phosphorous to remote ecosystems, and thus can alter biogeochemical cycles in the ocean (Hand et al., 2004; Jickells et al., 2005; Moore & Braucher, 2008) and on land (Okin et al., 2004; Das et al., 2013). Dust also affects human and animal health by carrying bacteria, viruses, or fungi over long distances (Weir-Brush et al., 2004; Schweitzer et al., 2018) while also increasing the risk of lung disease (Schweitzer et al., 2018) and hospitalizations for asthma (Kanatani et al., 2010).

In this study we consider the direct radiative effect ζ of dust in the shortwave (SW) part of the electromagnetic spectrum, which is defined as the difference between the SW net flux for clear-sky (cloud free) and pristine-sky (aerosol and cloud free) conditions. It is well known that the SW ζ at TOA is negative (Tegen et al., 1996) and recent work has estimated the global SW ζ at TOA to be -0.5 ± 0.35 W m^{-2} (Kok et al., 2017) and -0.25 ± 0.22 W m^{-2} (Di Biagio et al., 2020). The sign of the regional TOA SW ζ of dust, however, is dependent on the region's surface albedo because dust is more absorbing over brighter surfaces (i.e. desert and snow) (Tegen et al., 1996; Yang, Gupta, & Christopher, 2009; Ansell, Brindley, Pradhan, & Saunders, 2014). Here, we focus on one of the major dust source regions, the Sahara Desert (Goudie & Middleton, 2001) which is characterized by high surface albedo (Yang et al., 2009; Ansell et al., 2014). In

an observation-based study, Hsu et al. (2000) estimated the monthly clear-sky TOA SW ζ of dust from February–July 1985 over both the Sahara Desert and the ocean off the coast of North and West Africa. Hsu et al. (2000) was unable to estimate the TOA SW ζ of dust over land due to challenges with retrieving the aerosol optical thickness (AOT) over land, but estimated the range of TOA SW ζ of dust over the ocean as -10 to -50 W m^{-2} . Using a similar methodology, Yang et al. (2009) used satellite observations and retrievals to estimate the spatially averaged TOA SW forcing efficiency η , the ζ of dust normalized by the aerosol optical depth τ , of dust over the Sahara Desert as $1.6 \pm 11.3 \text{ W m}^{-2}$ per AOT. Additionally, Yang et al. (2009) found that negative TOA SW η of dust occur in locations with surface albedo less than 0.32 whereas in locations with surface albedo greater than 0.36, the TOA SW η of dust is near zero or slightly positive.

The typical method to estimate ζ of dust is via calculations with a radiative transfer model (e.g. Helmert et al., 2007; Highwood & Ryder, 2014). However, such calculations require precise knowledge of several parameters that are highly uncertain. For example, the complex index of refraction must be defined across all wavelengths for which the radiative transfer calculations are performed, which requires knowledge of the mineralogy of the aerosols (Scanza et al., 2015). Furthermore, the composition of dust varies among the discrete source regions (Journet et al., 2014), resulting in variations in the complex index of refraction (Di Biagio et al., 2017; Di Biagio et al., 2019) that are large enough to significantly alter the resulting radiative transfer calculations (L. Li et al., 2021). Next, radiative transfer calculations of the ζ requires knowledge of the dust size distribution. Although there is a theoretical description of the emitted size distribution for particle sizes less than $10 \mu\text{m}$ (Kok, 2011), the emitted distribution of larger sized particles is less certain, as is the dependence of those larger sizes in the state of the atmosphere (Shao et al., 2020). Dust particles are also highly aspherical (Kandler et al., 2007), which both complicates the calculation of the aerosol's single scatter properties (e.g. Saito & Yang, 2021a) and causes biases in in-situ measurements of the size distribution (Huang, Adebisi, Formenti, & Kok, 2021). Further complicating matters is a poor understanding of changes in the size distribution with

atmospheric residence time (van der Does et al., 2018), which contributes to the underestimation of large ($> 10\mu\text{m}$) dust particles in the Earth' atmosphere (Kok et al., 2017; Adebisi & Kok, 2020; Di Biagio et al., 2020).

It is possible to estimate the ζ solely from observations of the SW radiative flux and aerosol optical depth τ at some reference wavelength Conant (2000), which circumvents the uncertainty associated with radiative transfer calculations and provides an independent estimate of ζ against which calculations with a radiative transfer model can be compared. One challenge in estimating ζ of dust from observations alone is obtaining pristine-sky SW fluxes since rarely, if ever, is τ equal to 0. To overcome this obstacle, a few studies approximated pristine-sky SW fluxes as observed clear-sky SW fluxes that correspond to τ retrievals less than a specific threshold value (Conant, 2000; Christopher & Zhang, 2002; Helmert et al., 2007). Other studies approximated the pristine-sky SW flux by extrapolating clear-sky SW flux observations as a linear function of τ (Huttunen et al., 2014; Loeb & Kato, 2002). A more commonly used observational method involves using linear least squares regression to estimate the dust SW forcing efficiency η , which is the change in ζ per unit change in τ , i.e., $\eta = \partial\zeta/\partial\tau$ (Di Biagio et al., 2009, 2010; Hsu et al., 2000; Satheesh & Ramanathan, 2000), and where ζ averaged over some period of time can be estimated from η and an averaged value of τ , $\langle\zeta\rangle = \eta\langle\tau\rangle$. The advantage of these observational methods to calculate ζ of dust is that they do not require information about dust properties like the size distribution, index of refraction, particle shape, etc. However, there are potential sources of uncertainty in these observational methods, including retrieval error (F. Li et al., 2004) and the necessity to obtain a large collocated sample of flux and optical depth measurements (Di Biagio et al., 2010). A possible limitation in this method is identifying cloud cover, which we assume to be minimal in this study because we apply more conservative cloud filtering criteria to our dataset. Another potential source of uncertainty arises if other atmospheric constituents are correlated to dust. Hsu et al. (2000) showed that dust and water vapor are anti-correlated over the ocean and off the coast of northwestern Africa, which they indicated could produce a bias in calculations of ζ , such that they estimated a “dry” dust ζ

per unit aerosol index by limiting their analysis to observations with corresponding low values of precipitable water.

The main goals of this study are to detail how a correlation between dust and water vapor bias observation-only estimates of η and develop a simple method to account for such a correlation, thus improving the quality of η estimates derived from observations. We do so via an analysis of 9 years of satellite data over the Sahara, the world's largest source of airborne dust (Goudie & Middleton, 2001). The paper is structured as follows. In Section 2.2 we discuss the satellite data and radiative transfer model used in this study. In Section 2.3 we summarize the theory underlying the commonly used method to estimate η from only observations and develop a new method to do so that accounts for a potential correlation between dust and water vapor. We next demonstrate the utility of this new method via idealized experiments performed with a hierarchy of radiative transfer models of varying complexity (Section 2.4). In section 2.5, we estimate the minimum sample size required in order to obtain an uncertainty of less than 10% in η estimates. Next, in Section 2.6 we apply these methods, using 9 years of satellite observations and retrievals to estimate the clear-sky TOA SW η of dust over the Sahara Desert. Lastly, we conclude with a summary and discussion in Section 2.7.

2.2 Data and Model

2.2.1 Data

In this study we utilize data from the Clouds and the Earth's Radiant Energy System (CERES) Single Scatter Footprint (SSF) level 2, edition 4 data product (Wielicki et al., 1996) on-board the Aqua (NASA/LARC/SD/ASDC, 2014a) and Terra satellites (NASA/LARC/SD/ASDC, 2014f), which are near-polar and sun-synchronous orbiting satellites in the Earth Observing System (EOS) National Aeronautics and Space Administration (NASA) program. Aqua passes over the equator while traveling northward and southward at 1:30 pm and 1:30 am local time, respectively, while Terra correspondingly passes over the equator at 10:30 am and pm local time

(Loeb et al., 2018; Parkinson, 2003). CERES is a space-borne instrument that provides estimates of the TOA SW (0.2–5 μm), window (8–12 μm), and total (0.2–100 μm) flux with a footprint nadir spatial resolution of 20 km. The CERES SSF level 2 data product reports instantaneous data along the CERES footprint. In this study we utilize instantaneous footprint measurements of TOA SW upward flux (Su, Corbett, Eitzen, & Liang, 2015a), from 2010-2019 and over North Africa (8-38°N and 20°W-40°E).

The CERES SSF data product includes collocated Moderate-Resolution Imaging Spectroradiometer (MODIS) data and data from the Global Modeling and the Assimilation Office (GMAO) reanalysis product from the Goddard Earth Observing System Model version 5.4.1 (GEOS-5) (Su et al., 2015a). GEOS-5 provides meteorological parameters that serve as inputs for CERES algorithms (Su et al., 2015a). MODIS is a radiometer that measures radiation at 36 wavelength channels within 0.4–14.5 μm at 1 km, 500 m, and 250 m nadir spatial resolutions (Parkinson, 2003). Here, we use the over-land deep-blue 550 nm aerosol optical depth τ from MODIS Collection 5.1 (MOD04.L2 and MYD04.L2) (Levy et al., 2013) and total precipitable water q from GEOS-5 in the CERES SSF data product (NASA/LARC/SD/ASDC, 2014a, 2014f; Wielicki et al., 1996). The MODIS τ from the CERES SSF level 2 dataset differs from the standard aerosol MODIS τ dataset in that former dataset is collocated with CERES data, which for the level 2 data product is reported instantaneously (i.e. along-track of the CERES footprint).

The CERES SSF data product also includes surface solar zenith angle and clear-sky fraction information. In order to determine which data are cloud free (clear-sky), we obtain the clear/layer/overlap condition percent coverage parameter (Minnis et al., 2008; Minnis, Sun-Mack, Young, et al., 2011; Minnis, Sun-Mack, Chen, et al., 2011). This parameter depicts the percentage of the following four cloud coverages: 1) clear-sky, 2) lower clouds only, 3) upper clouds only, and 4) upper over lower clouds. The sum of all cloud coverages must be equal 100. In this analysis, we only include data for which the clear/layer/overlap condition parameter is 100% clear-sky (100 for cloud coverage 1). Because we are interested in daytime data we exclude data with solar zenith angle greater than 90°. After filtering the satellite data for clear-sky and

daytime conditions, we calculate daily averaged MODIS total τ , GOES-5 total precipitable water, CERES solar zenith angle θ , and CERES TOA SW upward flux data over 1° grid-boxes within $8\text{-}38^\circ\text{N}$, $20^\circ\text{W}\text{-}40^\circ\text{E}$, and for each satellite.

Because it is possible that dust is not the only aerosol species that comprises the total aerosol optical depth in the regions surrounding the Sahara Desert, we also utilize estimates of dust optical depth generated from MODIS Aqua and Terra (Voss & Evan, 2020, 2019). This dust optical depth τ_d dataset contains daily, global dust optical depth estimates at a 1° horizontal resolution derived from deep-blue MODIS Aqua and Terra aerosol optical depth, 470–670 nm Angstrom Exponent, and 412 and 660 nm Single Scatter Albedo (Voss & Evan, 2020). In order to estimate daily τ_d for each grid-box, Voss and Evan (2020) only included clear-sky and daytime MODIS aerosol optical depth retrievals that satisfied the following conditions: 1) 470–670 nm Angstrom Exponent less than 1, 2) 412 nm Single Scatter Albedo less than 0.95, and 3) 660 nm Single Scatter Albedo greater than that at 412 nm. If these conditions were not met, τ_d was set to zero (Voss & Evan, 2020). Here, we obtain τ_d over land within $8\text{-}38^\circ\text{N}$ and $20^\circ\text{W}\text{-}40^\circ\text{E}$ from 2010-2019 (Voss & Evan, 2019).

2.2.2 Radiative Transfer Model

In this study we use the Streamer radiative transfer model (Key & Schweiger, 1998, 2013) in order to evaluate observation-only methods for estimating the clear-sky TOA SW η of dust. Streamer calculates upwelling and downwelling TOA SW fluxes at 24 spectral bands ($0.28\text{-}4\ \mu\text{m}$); here, four streams are used and thus, the radiative transfer equation is solved via the discrete ordinate solver (Stamnes, Tsay, Wiscombe, & Jayaweera, 1988). In Streamer gaseous absorption is due to water vapor, oxygen, ozone, and carbon dioxide. Gaseous data is from Tsay, Stamnes, and Jayaweera (1989) and water vapor absorbs in the following SW wavelengths (μm): 0.69-0.75, 0.78-0.87, 0.87-1, 1.1-1.19, 1.28-1.53, 1.64-2.13, 2.13-2.38, 2.38-2.91, 2.91-3.42, and 3.42-4.

We run Streamer with a purely desert surface with an average surface albedo equal to 0.23

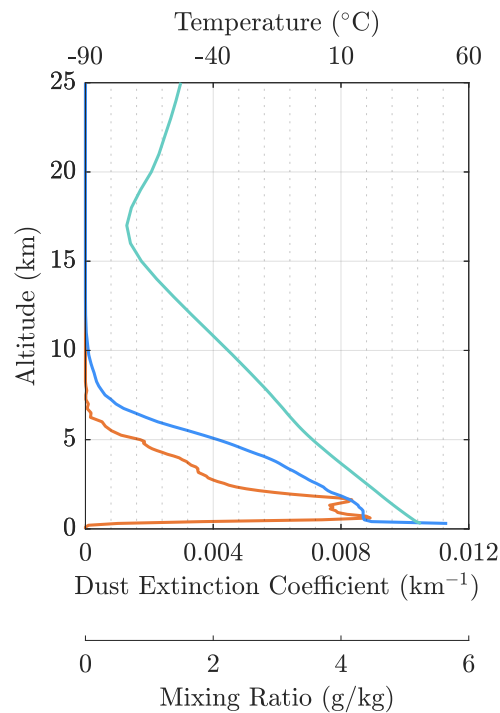


Figure 2.1: Temporally averaged vertical profiles of temperature (teal), mixing ratio (blue), and dust extinction coefficient (orange) at In Salah, Algeria for the summer months of July and August 2010–2015.

(Tanre, 1986) and with dust optical properties from A. T. Evan and Mukhopadhyay (2010), which are based on measurements made during the Saharan Dust Experiment (SHADE) campaign in west Africa. We run Streamer with a constant vertical profile of temperature (turquoise line, Figure 2.1), which is generated from an average of summer and daytime soundings made at In Salah, Algeria over the time period 2005–2010 (A. T. Evan, Flamant, Lavaysse, Kocha, & Saci, 2015). Within Streamer we vary dust optical depth and total precipitable water by scaling climatological profiles of water vapor mixing ratio (blue line, Figure 2.1) and the dust extinction coefficient (orange line, Figure 2.1), where the mixing ratio profile is also an average of soundings made at In Salah and the extinction profile is from an average of Cloud-Aerosol Lidar and Infrared Pathfinder Satellite Observation (CALIPSO) data made over the same time period and for the same location as the soundings (W. Wang, Evan, Lavaysse, & Flamant, 2017). The extinction profile was forced to zero above 8 km and smoothed below this height with a 180

m boxcar filter.

2.3 Background and Motivation

In this Section we describe the old method used to estimate the TOA clear-sky SW dust forcing efficiency η from only observations (i.e., not using a radiative transfer model) and then provide a brief discussion of how a non-zero correlation between dust and moisture can affect the estimated η . We then present new results demonstrating that dust and moisture are significantly correlated over much of North Africa, which motivates a subsequent presentation of a new version of this observational method that can account for such correlations.

2.3.1 Old Method

At the TOA η can be estimated using observations of the clear-sky upwelling SW flux S^\uparrow and retrievals of aerosol optical depth τ ,

$$\eta_o = -\frac{dS^\uparrow}{d\tau} \quad (2.1)$$

where the subscript o refers to the old method for defining η (see 2.8.1 for a complete derivation).

This method implicitly assumes that S^\uparrow is a linear function of τ ,

$$S^\uparrow = \frac{dS^\uparrow}{d\tau} \tau + S_p^\uparrow \quad (2.2)$$

where S_p^\uparrow is the upward SW flux at TOA for a pristine-sky atmosphere (i.e., $\tau = 0$) and that the pristine-sky fluxes are not correlated to dust (2.8.1). Given values of τ and S^\uparrow Eq. 2.2 can be solved for $dS^\uparrow/d\tau$, and thus η , via linear regression. As previously mentioned, a number of studies have used this approach to estimate η (e.g., Hsu et al., 2000). Further, S^\uparrow from Eq. 2.2 is also highly dependent on surface albedo α and solar zenith angle θ ; we do not account for α in Eq. 2.2 because the effects of the surface albedo on S^\uparrow are out of scope for this study. To account for θ we estimate η_o via linear least square regression of Eq. 2.2 for several μ intervals,

where $\mu = \cos \theta$, ranging from 0 to 1. Note that Eq. 2.1 is not the definition of η but rather an estimation of η .

2.3.2 Correlation in Dust and Water Vapor

Why would a positive or negative correlation between dust and total precipitable water $r_{\tau,q}$ affect an estimate of η generated via Eq. 2.2? Since water vapor absorbs light at several wavelengths in the solar part of the spectrum, if temporal changes in the concentration of atmospheric dust and water vapor are correlated, at a given location, an observed change in S^\uparrow per unit change in τ would include dust-forced and vapor-forced components, resulting in a biased estimate of η via Eq. 2.2 where the sign of the bias depends on the sign of the correlation. For example, since in general the presence of dust increases S^\uparrow and the presence of water vapor decreases this value, if changes in dust and water vapor are negatively correlated ($r_{\tau,q} < 0$) the dust-forced increase in S^\uparrow will be greater than it would be if $r_{\tau,q} = 0$ (Figure 2.2a), resulting in a larger magnitude of η calculated via Eq. 2.2 and thus an estimate of η that is biased negative. Conversely, if dust and water vapor are positively correlated ($r_{\tau,q} > 0$) the dust forced-increase in S^\uparrow will be offset by an increase in atmospheric absorption of solar radiation by water vapor (Figure 2.2b), resulting in a smaller magnitude of η estimated via Eq. 2.2 and thus an estimate of η that is biased positive.

Are dust and total precipitable water over North Africa correlated? Results from prior studies would suggest this may be the case. Previous work has shown that the high wind speed events that generate dust outbreaks in northern Africa are oftentimes associated with convective downdrafts from mesoscale convective systems (Flamant et al., 2007; Karam et al., 2008; Knippertz & Todd, 2010; Roberts & Knippertz, 2014) or frontal cyclones (Knippertz & Todd, 2010), both processes that could simultaneously produce positive anomalies in atmospheric moisture. Additionally, Marsham et al. (2013) observed that at Bordj-Badji Mokhtar (21.4°N, 0.9°E) dust is often coupled with moisture advection with both associated with cold pool outflows (haboobs) generated within monsoonal flows and calculated a positive correlation of 0.3 between

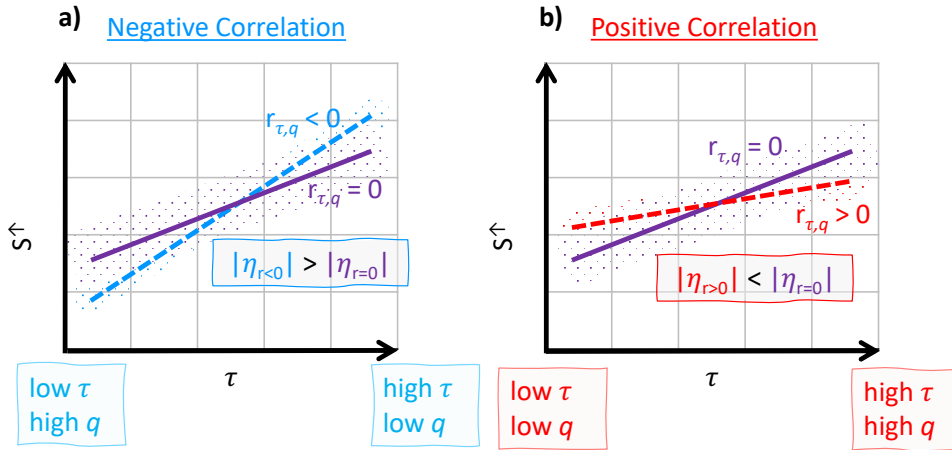


Figure 2.2: The potential scatter between S^\uparrow and τ when a) $r_{\tau,q} < 0$ and b) $r_{\tau,q} > 0$, where τ increases to the right on the x-axis and S^\uparrow increases upwards on the y-axis. The potential linear fits of S^\uparrow as a function of τ are depicted by the blue dashed line when $r_{\tau,q} < 0$, the red dashed line when $r_{\tau,q} > 0$, and the solid purple line when $r_{\tau,q} = 0$. The relative magnitudes of η when dust and water vapor are anti-correlated, correlated, and uncorrelated are depicted by the subscripts $r < 0$ (blue), $r < 0$ (red), and $r = 0$ (purple), respectively.

optical depth and water vapor there.

In order to evaluate whether or not dust and total precipitable water over northern Africa are correlated we calculated the correlation coefficient between monthly mean values of aerosol optical depth τ from MODIS and total precipitable water q from GEOS-5 using over-land data for the years 2010–2018 (Figure 2.3a). Positive and significant correlation coefficients are broadly found north of 12°N , with the highest values (> 0.6) found around 23°N between -15° and 5°E . We find a small area of significant and negative values of correlation coefficients equatorward of the Sahara that is centered on 10°N and between -5° and 20°E . Since dust is not the only aerosol present in the atmosphere over northern Africa we also calculated the correlation using a record of dust optical depth (Voss & Evan, 2020, 2019). The correlation coefficients using the dust optical depth data (Figure 2.3b) are similar to those using the aerosol optical depth (Figure 2.3a), which is not entirely surprising since both are derived from the MODIS instruments flying on the Aqua and Terra satellites, with the main difference being that the magnitudes of the correlations calculated using the dust optical depth data are larger by approximately 20%

over the Sahara. We obtain qualitatively similar results using daily mean values to calculate the correlation coefficients in Figures 2.3ab (not shown). A more in-depth investigation of the physical causes of the correlation between dust and water vapor over northern Africa is outside the scope of this paper.

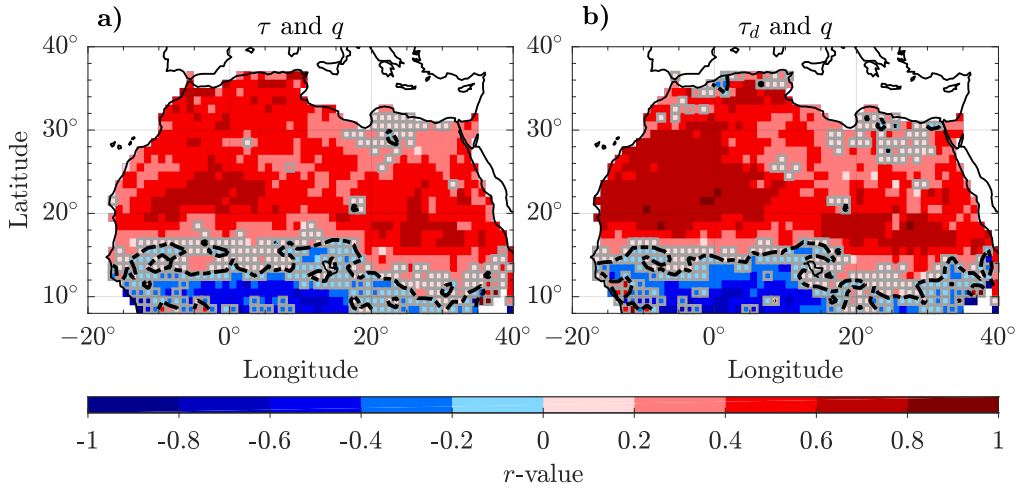


Figure 2.3: Correlation between atmospheric moisture and dust over northern Africa. Plotted in 2.3a is a map of the correlation coefficients $r_{\tau,q}$ for monthly mean values of aerosol optical depth and total precipitable water using data for the time period 2010–2018. Shown in 2.3b are similar correlation coefficients that are calculated using estimates of the dust optical depth. Only statistically significant values (p -value < 0.05) are shaded, with regions of non-significant correlations indicated by light gray squares. The black, dashed contour line indicates correlation coefficients equal to zero.

2.3.3 New Method to Estimate the Forcing Efficiency

Given the significant correlation between dust and water vapor over the Sahara (Figure 2.3) and the impact such a correlation can have on an observational method to estimate the forcing efficiency (Figure 2.2), we propose a modification to Eq. 2.1 in order to account for correlation related biases in the forcing efficiency. Assuming that S^\uparrow is a linear function of aerosol optical depth τ and total precipitable water q the equation for the upwelling solar radiation at

TOA S^\uparrow is

$$S^\uparrow = \left(\frac{\partial S^\uparrow}{\partial \tau} \right)_q \tau + \left(\frac{\partial S^\uparrow}{\partial q} \right)_\tau q + S_{p,dry}^\uparrow \quad (2.3)$$

where $(\)_q$ and $(\)_\tau$ indicate partial derivatives with q or τ held constant, respectively, and $S_{p,dry}^\uparrow$ is the upward SW flux at the TOA for a pristine and completely dry atmosphere. We define a new estimate of the forcing efficiency η_n for atmospheric moisture held constant,

$$\eta_n = - \left(\frac{\partial S^\uparrow}{\partial \tau} \right)_q \quad (2.4)$$

which can be estimated via multivariate linear regression with measurements of S^\uparrow , τ , and q via Eq. 2.3 (see 2.8.2 for a complete derivation). Note that similarly to the old method, S^\uparrow from Eq. 2.3 is also highly dependent on surface albedo α and θ and as a result we estimate η_n via multivariate linear regression of Eq. 2.3 for several μ intervals. Note that Eq. 2.4 is not an explicit definition for η but rather an estimate of η .

2.4 Evaluating the New Forcing Efficiency in an Idealized Framework

In this Section we quantify the bias in η_o (Eq. 2.1) associated with a non-zero correlation between water vapor and dust and demonstrate that η_n (Eq. 2.4) effectively accounts for such a correlation. To do so we generate output from a hierarchy of radiative transfer models of increasing complexity with which we can estimate a true forcing efficiency η_t for each model by varying dust optical depth τ_d in the model and comparing the TOA SW fluxes against a case where $\tau_d = 0$.

We first generate a synthetic time series of τ_d of length 10,000 by randomly sampling positive values from a Gaussian distribution of mean 0 and standard deviation 1. This synthetic time series of τ_d is initially generated with a mean of 0 and standard deviation of 1 such that

the corresponding synthetic time series of column integrated water vapor optical depth τ_q with correlation r_{τ_d, τ_q} can be quantified via the expression

$$\tau_q = r_{\tau_d, \tau_q} \times \tau_d + \varepsilon \sqrt{1 - r_{\tau_d, \tau_q}^2} \quad (2.5)$$

where ε is a time series of length 10,000 drawn from a Gaussian distribution of mean 0 and standard deviation 1. The resulting synthetic time series of τ_q is then normalized to an arbitrary mean and standard deviation of 0.1 and 0.025, respectively. Additionally, we normalize the initial synthetic time series of τ_d with an arbitrary mean of 0.5 and standard deviation of 0.125. We repeat this procedure for values of r_{τ_d, τ_q} spanning -1 to 1 at increments of 0.01. We then force the three idealized models described below with the synthetic time series of τ_d and the corresponding set of τ_q synthetic time series, and estimate η_t , η_o , and η_n in the manners described above. The output from these idealized model simulations are not meant to precisely simulate the dust direct radiative forcing in the real world, but rather are intended to provide a consistent framework within which we can test the utility of the new observational method to estimate η .

2.4.1 Linear Model

We start with the most simple model, which is a highly idealized linear radiative transfer model. We assume homogeneous dust and water vapor layers in the atmosphere with reflectances R_d and R_q and transmittances T_d and T_q , respectively. We assume a surface of albedo α of 23%, which is the average solar surface albedo of a generic desert surface in the Streamer model at a solar zenith angle θ of 32.8°. We allow no multiple scattering between the dust layer and the surface.

Given this formulation, the reflectance of the dust layer R_d can be written as a linear function of its single scatter properties.

$$R_d = \tau_d \omega_d \frac{1 - g_d}{2} \quad (2.6)$$

where ω_d is the single scatter albedo and g_d is the asymmetry parameter of dust. Here we apply a simplified linearization to the two-stream solution from Meador and Weaver (1980) and have assumed that $(1 - e^{-\tau_d}) \approx \tau_d$ which is then equivalent to the probability that a photon will undergo an extinction event when passing through the dust layer, ω_d is the probability that this event will result in photon scattering, and $(1 - g_d)/2$ is the probability that scattering is in the backward direction. We choose representative values of 550 nm ω_d and g_d of dust from J. Haywood et al. (2003) ($\omega_d = 0.95$ and $g_d = 0.74$). The absorption of the dust layer A_d is given by

$$A_d = \tau_d(1 - \omega_d) \quad (2.7)$$

with similar rationale as that described for R_d , and the dust layer transmittance T_d is then

$$T_d = 1 - A_d - R_d \quad (2.8)$$

We assume a similar set of expressions for the absorptivity A_q and transmittance T_q of the water vapor layer, which is non-scattering,

$$A_q = \tau_q \quad (2.9)$$

and

$$T_q = 1 - A_q \quad (2.10)$$

The total scene reflectance \tilde{R} is the linear sum of the dust and water vapor forced components

$$\tilde{R} = R_d + \alpha(T_d^2 + T_q^2) \quad (2.11)$$

where we have summed the transmittance terms in order to maintain linearity in the model solution for η . We define the model dust direct effect ζ as

$$\zeta = -S_0 (R_d + \alpha T_d^2) \quad (2.12)$$

which is the difference between the upwelling pristine-sky solar flux S_p^\uparrow and the upwelling clear-sky solar flux S^\uparrow at the TOA. The model dust forcing efficiency η_t is then calculated as the slope of the regression of ζ onto τ_d . The model S^\uparrow is

$$S^\uparrow = S_0 \tilde{R} \quad (2.13)$$

and the corresponding S_p^\uparrow is

$$S_p^\uparrow = S_0 \tilde{R}_p \quad (2.14)$$

where \tilde{R}_p is the scene reflectance in pristine-sky conditions (i.e. when solar fluxes only interact with the water vapor layer).

We force the model with the synthetic time series of τ_d and τ_q , spanning all possible correlations between total precipitable water and dust optical depth. We choose a value of S_0 so that η_t is $-20 \text{ W m}^{-2} \tau^{-1}$ when dust and water vapor are uncorrelated (Figure 2.4a, circles). Using the model output we estimate η_o and η_n via the linear regression of the model output S^\uparrow onto τ_d (Eq. 2.1) and the multivariate linear regression of S^\uparrow onto τ_d and τ_q (Eq. 2.4), respectively. We find that biases in η_o are of the same sign as r_{τ_d, τ_q} and increase in magnitude for increasing values of r_{τ_d, τ_q} (Figure 2.4a, red line), which is consistent with our proposed mechanism (Figure 2.2). In contrast, η_n exactly reproduces η_t (Figure 2.4a, blue line) as Eq. 2.4 explicitly accounts for the correlation between moisture and dust. Since η_t is equal to η_n (Eq. 2.4), we derive an expression for the bias in η_o as $-\left(\frac{\partial S^\uparrow}{\partial q}\right)_\tau \frac{dq}{d\tau}$ and assuming that $dq/d\tau$ is directly proportional to r_{τ_d, τ_q} find that the bias in η_o is a linear function of r_{τ_d, τ_q} .

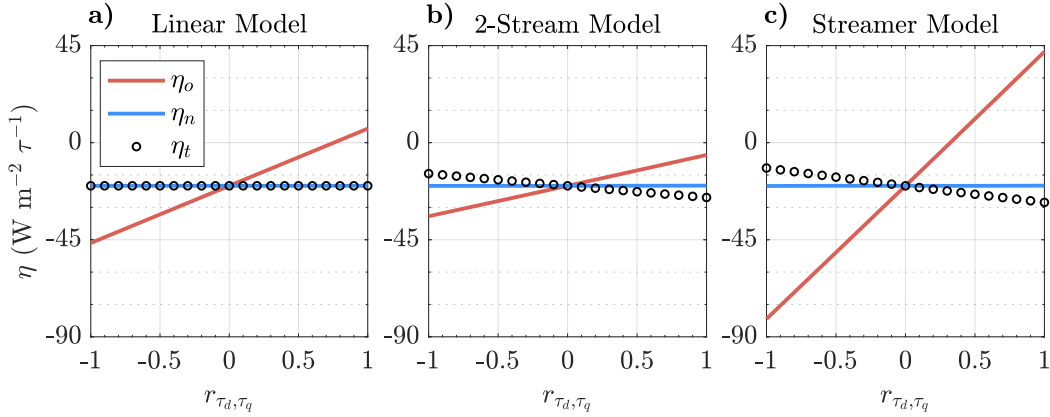


Figure 2.4: Plotted are the output from the (a) linear, (b) two-stream, and (c) Streamer idealized models showing the impact of a correlation between dust and water vapor on observational estimates of the forcing efficiency η . Shown is the model dust forcing efficiency η_t (black circles), the forcing efficiency estimated via Eq. 2.4 η_n (blue line), and the forcing efficiency estimated via Eq. 2.1 η_o (red line), as a function of the correlation between water vapor and dust optical depth r_{τ_d, τ_q} .

2.4.2 Two-stream model

We again test the utility of estimating the forcing efficiency via Eq. 2.4 but this time via the two-stream solution to the radiative transfer equation (Meador & Weaver, 1980), which offers a more realistic representation of radiative processes than does the linear model. Here the most relevant differences between the linear and two-stream radiative transfer models are that the two-stream model accounts for interaction between the dust and water vapor layers (e.g., photons can be scattered off the dust layer but then absorbed within the water vapor layer) and that multiple scattering can occur between the dust layer and surface. We note that the effect of the vertical distribution of dust (Liao & Seinfeld, 1998) and less absorbing aerosol particles (Meloni, di Sarra, Di Iorio, & Fiocco, 2005) is second order in the SW spectrum (Meloni et al., 2005; Liao & Seinfeld, 1998) and thus do not vary the vertical distribution of dust in the two-stream model. We assume a homogeneous dust layer suspended above a homogeneous water vapor layer and again a surface with $\alpha = 23\%$. For this model the total scene and pristine-sky reflectances are calculated according to Meador and Weaver (1980), utilizing the same optical properties of dust

and water vapor used in the linear radiative transfer model, and taking a single value of each property to represent the entire solar spectrum (i.e., a single “band” model). Identical to the linear radiative transfer model, the model direct effect ζ is calculated as the difference between the TOA upwelling solar fluxes in pristine-sky and clear-sky conditions, and the corresponding forcing efficiency η_t is estimated via linear regression of ζ onto τ_d . We again choose a value of S_0 such that $\eta_t = -20 \text{ W m}^{-2} \tau^{-1}$ at $r_{\tau_d, \tau_q} = 0$. We use the model output S^\uparrow to estimate η_o and η_d via Eqs. 2.1 and 2.4, respectively.

In the two-stream model (Figure 2.4b), η_o exhibits a similar dependence on r_{τ_d, τ_q} as does η_o from the linear model (Figure 2.4a); more specifically, biases in η_o are the same sign as r_{τ_d, τ_q} , which is consistent with Figure 2.2, and the magnitude of these biases increases as magnitude of r_{τ_d, τ_q} increases. In contrast to the linear model (Figure 2.4a), we find that there are biases in η_n estimated from the output of the two-stream model and that the magnitude of these biases vary as a function of r_{τ_d, τ_q} (Figure 2.4b). Additionally, we find that η_t exhibits a weak dependence on r_{τ_d, τ_q} . Small biases in η_n and variable η_t arise due to how η_t is estimated. In the idealized models presented here, we estimate η_t as the linear regression of the true ζ and τ_d , where the true ζ is equal to the difference between S_p^\uparrow and S^\uparrow . If the true ζ is instead estimated as the difference between \bar{S}_p^\uparrow and S^\uparrow , where \bar{S}_p^\uparrow is the TOA SW upward flux for mean water vapor conditions, biases in η_n are equal to zero. This finding is in contrast to the linear model because $S_p^\uparrow = \bar{S}_p^\uparrow$ and non-linearities arise since the dust and water vapor layers do not interact with one another. Biases in η_n also occur because the key assumption made when deriving η_n is not met in the two-stream model; more specifically, in the two-stream model $(\partial S^\uparrow / \partial q)_\tau$ is not equal to $\partial \bar{S}_p^\uparrow / \partial q$ unless dust and water vapor are uncorrelated. Nonetheless, when using an idealized model with slightly more complete physics, we still find that the old observational method to estimate the forcing efficiency, η_o , may produce a biased estimate unless water vapor is explicitly accounted for.

2.4.3 Streamer Radiative Transfer Model

Lastly we examine the effect of a correlation between dust and water vapor on the old and new observational methods to estimate η in a comprehensive radiative transfer model forced with realistic environmental conditions. More specifically, Streamer differs from the two-stream model by including gaseous absorption, quantifying SW fluxes with four streams, and allowing spectral variation of the optical properties of dust and atmospheric gases. Here we force the Streamer model (Key & Schweiger, 1998, 2013) configured as described in Section 2.2.2 with the same synthetic time series of τ_d and τ_q as described for the other models and with a constant and arbitrary value of the solar zenith angle θ (32.8°). Similar to the two-stream model, we do not vary the vertical distribution of dust since this effect on the η is second order in the SW spectrum (Meloni et al., 2005; Liao & Seinfeld, 1998). We estimate the model ζ and η_t in a manner identical to that for the linear and two-stream models and scale the model S_0 so that η_t has a value of $-20 \text{ W m}^{-2} \tau^{-1}$ when $r_{\tau_d, \tau_q} = 0$. We estimate η_o and η_n using the model output values of S^\uparrow via Eqs. 2.1 and 2.4, respectively.

The results from the Streamer simulations (Figure 2.4c) are nearly identical to those from the linear and two-stream cases (Figures 2.4a,b), where η_n is constant for all values of r_{τ_d, τ_q} and η_o exhibits a bias that is proportional to r_{τ_d, τ_q} . The magnitudes of the biases in η_o in the Streamer model, however, are larger than those for the linear and two-stream model; in the linear and two-stream models the magnitude of the biases at $|r_{\tau_d, \tau_q}| = 1$ are within 77-138% of the η_t at the same r_{τ_d, τ_q} . For the same values of r_{τ_d, τ_q} in the Streamer model the magnitudes of the η_o bias are greater than 250% of the corresponding η_t values. Compared to the η_o bias from the two-stream model the biases in the Streamer model are larger due to the more comprehensive treatment of water vapor, resulting in a stronger sensitivity of S^\uparrow to changes in q . To a smaller extent the biases in η_o in the linear model are larger than that of the two-stream model due to its inherent simplicity. Similar to the two-stream model, η_n estimated from the Streamer model also exhibits a small bias that is linearly dependent on r_{τ_d, τ_q} and biases in η_n are greatly reduced.

For example, when $|r_{\tau_d, \tau_q}| = 1$ the η_n biases are approximately 23-75% of the corresponding η_t . One limitation to this study is that since the Streamer code has been created, some studies have found that water vapor absorbs at more SW wavelengths than previously thought (i.e. in the near ultraviolet radiative spectrum near $0.3 \mu\text{m}$ in Gordon et al., 2022). Nonetheless, based on these results the proposed method to account for a correlation between dust and water vapor when estimating η observationally is both effective and warranted.

2.5 Sample Size and Forcing Efficiency Uncertainty

Before we apply these results and estimate η using measurements of τ , q , and S^\uparrow , we quantify improvement in uncertainty when utilizing this new method for estimating the forcing efficiency. To do so we use the Streamer model forced with the synthetic time series of τ_d and τ_q to evaluate the relationship between observation sample size N and measurement uncertainty σ on the total uncertainty in η calculated from observations. More specifically, we estimate the minimum sample size N required so that the relative uncertainty in η_o or η_n is $< 10\%$, N_{10} . We define a 10% uncertainty in η as a 95% confidence interval around the regression coefficient calculated via Eqs. 2.1 and 2.4 (i.e., regression slopes) that is of magnitude $0.1 \times \eta$. We accomplish this by using the output from the Streamer model described in Section 2.2.2. For each set of Streamer simulations corresponding to a specific value of r_{τ_d, τ_q} (increments of 0.05) we estimate values of N_{10} separately for η_o and η_n by calculating the 95% confidence intervals around the regression slopes. In order to generate robust results we calculate the confidence intervals for each value of N for 10,000 random samples of the data, averaging the results. We note that the choice of the arbitrary mean and standard deviations of the synthetic time series of τ_d and τ_q affect the results presented here, but the relationship between N_{10} estimated via the two observation-based methods remains the same. We also note that we make the assumption that retrieval uncertainties in τ_q are not so large as to negate the advantage of estimating η via the new method.

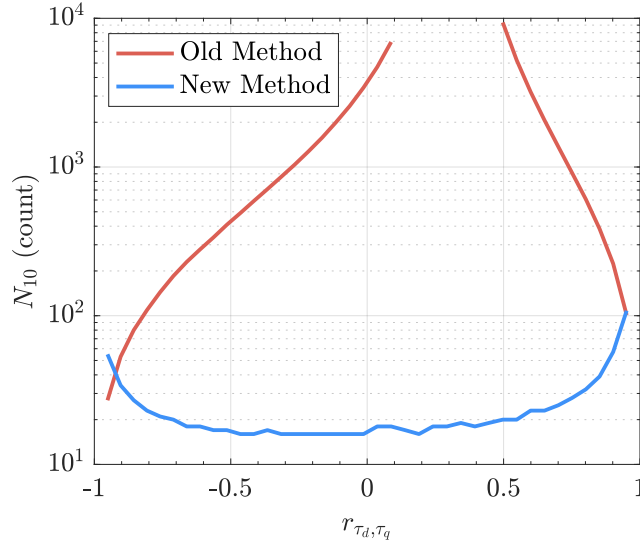


Figure 2.5: Shown are estimates of the number of observations required to generate estimates of the dust forcing efficiency with uncertainty less than 10%, N_{10} , as a function of the correlation between dust and water vapor optical depth r_{τ_d, τ_q} for η_o (blue line) and η_n (red line). Values are constructed using output from the Streamer model and synthetic time series of τ_d and τ_q .

For the old method, N_{10} (red line in Figure 2.5) increases and decreases approximately exponentially with r_{τ_d, τ_q} for $r_{\tau_d, \tau_q} < 0.1$ and $r_{\tau_d, \tau_q} > 0.5$, respectively. Note that N_{10} estimated with η_o is undefined for $0.1 \leq r_{\tau_d, \tau_q} \leq 0.5$ because at these r_{τ_d, τ_q} values, the uncertainty is always greater than 10% even though all available synthetic data of τ_d and τ_q were used to estimate η_o . The distribution of N_{10} estimated from η_o as a function of r_{τ_d, τ_q} is dependent on the scatter between S^\uparrow and the optical depths of dust and water vapor. More specifically, the magnitude of the covariances of S^\uparrow and both τ_d and τ_q are greatest when $|r_{\tau_d, \tau_q}| \approx 1$. Thus, less measurements of τ_d and S^\uparrow are required in order for the relative uncertainty of η_o to be less than 10%. One would then expect that the most scatter between S^\uparrow and the dust and water vapor optical depths would occur when dust and water vapor are uncorrelated; we find, however, that the shape of N_{10} estimated from η_o is asymmetrical around r_{τ_d, τ_q} (Figure 2.5) because there is more scatter between S^\uparrow and both τ_d and τ_q when r_{τ_d, τ_q} is positive but less than 1. This asymmetry arises due to the opposite radiative effects of dust and water vapor on S^\uparrow when dust and water vapor are positively correlated. As a result, more measurements of τ_d and S^\uparrow are needed in order to more

precisely determine the influence of dust on S^\dagger .

In the new method, N_{10} (blue line in Figure 2.5) has an approximate value of 18 observations for $|r_{\tau_d, \tau_q}| < 0.5$, meaning that given 18 observations of τ_q , τ_d , and S^\dagger , the relative uncertainty in η_n is 10% for a majority of r_{τ_d, τ_q} values. The convex shape of N_{10} estimated via η_n as a function of r_{τ_d, τ_q} (Figure 2.5) arises due to decreased precision in the regression slope in the multivariate regression from the new method (Eq. 2.4). More specifically, two strongly correlated predictor variables in multivariate regression (τ_d and τ_q) can add redundant information about the predictand (S^\dagger) to the analysis and as a result, the 95% confidence interval of the regression coefficients can increase. Thus, if r_{τ_d, τ_q} approaches 1 more measurements of τ_d , τ_q , and S^\dagger are required in order to decrease the relative uncertainty of η_n .

The main difference between N_{10} estimated via the old and new methods is that for $|r_{\tau_d, \tau_q}| \neq 1$ the N_{10} estimated from η_o is 1–2 orders of magnitude greater than N_{10} estimated from η_n . We note that N_{10} estimated via the old and new methods are somewhat dependent on the relative means and standard deviations of τ_d and τ_q . To ensure the robustness of Figure 2.5, we conducted a sensitivity analysis of N_{10} estimated via the old and new methods while varying the means and standard deviations of τ_d and τ_q . The main differences between these model runs are that the symmetry of N_{10} about r_{τ_d, τ_q} and the relative magnitude of N_{10} change (not shown). The main similarity is that N_{10} estimated via the old method is generally always larger than N_{10} estimated via the new method. Note that the most common N_{10} estimated via both observation-based methods across all r_{τ_d, τ_q} presented in this study may not equal the corresponding most common N_{10} estimated in a more complex environment (i.e. the real world) due to instrumental and retrieval uncertainty in S^\dagger , τ , and q . It is likely that in a more complex environment, however, N_{10} estimated via the old method will generally be greater than N_{10} estimated via the new method. Based on these results (Figure 2.5), we conclude that accounting for water vapor and dust when estimating η observationally (Eq. 2.4) reduces the number of retrievals and observations needed to more accurately estimate η .

2.6 Application to Real Data

Thus far we have used physical reasoning (Figure 2.2), theory (Section 2.3.3), and idealized experiments (Figure 2.4) to demonstrate that a non-zero correlation between water vapor and dust will generate a biased estimate of the dust forcing when only using observations and that this bias can be accounted for by estimating the forcing efficiency via multivariate linear regression (Eq. 2.4). We also showed that in the assumption that the uncertainty in τ_d and τ_q are unsubstantial accounting for the correlation between dust and water vapor can reduce the number of observations and retrievals needed to more accurately estimate the forcing efficiency (Figure 2.5). We next apply these findings and estimate the clear-sky SW forcing efficiency η of dust over North Africa using the CERES SSF data.

2.6.1 Instantaneous Forcing Efficiency

Here we utilize measurements of aerosol optical depth τ , total precipitable water q , solar zenith angle θ , and clear-sky TOA SW upward flux S^\uparrow from the CERES SSF data products from the Terra and Aqua satellites. Because it is likely that dust is not the sole contributor to the total τ we separately use estimates of dust optical depth τ_d from Voss and Evan (2020, 2019). Since the τ_d dataset only extends to 2019 we also only use CERES data for the 2010-2019 time period.

As η depends on θ we estimate η for 6 discrete intervals of μ (where $\mu = \cos \theta$) of equal width (0.1) from 0.4 to 1. Small changes to the width of the bins had no qualitative effect on the results shown here. The spatial distributions of η_o estimated using both τ (Figure 2.6a) and τ_d (Figure 2.6c) for $\mu > 0.9$ exhibit similar results. The maps of η_o are positive within roughly 10-28°N, 20-35°E; 16-34°N, 5°W-15°E; 16-24°N, 12°W-0°E; and 16-21°N, 10-20°E. Negative values of η_o for both maps occur within roughly 20-30°N, 15-20°E; 10-16°N, 17°W-10°E; 24-27°N, 0-13°E; and 24-31°N, 30-33°E. It is expected that the spatial distributions of η_o estimated with τ and τ_d within the Sahara Desert (19-30°N, 10°W-30°E) are similar because dust is the primary aerosol within this region. Here, we define the Sahara Desert within 19-30°N,

10°W-30°E in order to remain consistent with Voss and Evan (2020). The two maps of η_o differ in that there are more grid-boxes within the Sahara Desert that contain positive values of η_o estimated with τ_d than η_o estimated with τ . For example, within the northeastern region of the Sahara Desert η_o estimated with τ is more negative than η_o estimated with τ_d (Figures 2.6a,c). The differences in η_o estimated from both optical depth datasets may be due to more insignificant, low positive $r_{\tau_d,q}$ than $r_{\tau,q}$ in the northeastern Sahara (Figure 2.3). We note that the spatial structure of η_o for other μ intervals is similar to that shown in Figures 2.6a and c.

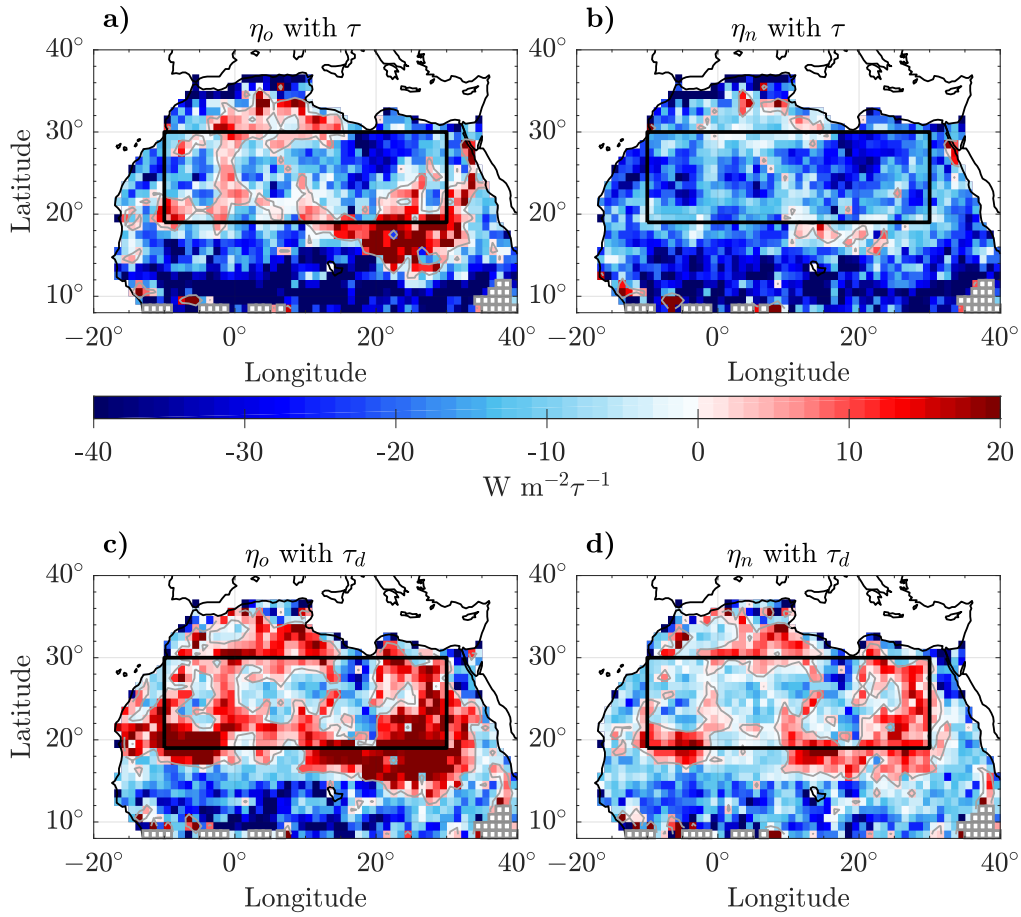


Figure 2.6: Maps of η_o estimated using τ and τ_d (a, c, respectively) and η_n estimated using τ and τ_d (b, d, respectively) for $\mu > 0.9$ (shading). The thin gray line indicates $\eta = 0$ and the grids enclosed by light gray boxes denote areas with undefined η values due to an insufficient number of available observations. The thick black line denotes the area used for averaging (e.g. in Figure 2.7).

Maps of η_n estimated using τ and τ_d (Figures 2.6b and d, respectively) for $\mu > 0.9$ show

somewhat distinct results. Both maps show regions where $\eta_n < 0$ south of 16°N , along nearly all coastlines, and in various locations between 16 and 30°N and west of 20°E . However, η_n estimated using τ exhibits far fewer locations where $\eta_n > 0$; 94% of the η_n values in Figure 2.6b are < 0 , whereas only in 67.6% are < 0 in Figure 2.6d. Given that the correlation between total precipitable water and optical depth is very similar for both τ and τ_d (Figure 2.3), the differences in η_n for these two data sets is likely due to the correlation with S^\uparrow , where τ is more strongly correlated with S^\uparrow than is τ_d (not shown). Differences in the gradient of S^\uparrow with each optical depth are due to outliers (extreme values of τ_d) present in the τ_d dataset, which is primarily due to different MODIS data products and spatial averaging being used in this study and that used in Voss and Evan (2020). Other explanations for the differences between η_n estimated with τ and τ_d are that other aerosols (i.e. smoke) that affect the TOA η may have been advected into the Sahara Desert and that the τ_d dataset filtered out cases of polluted dust. Additionally we cannot claim with absolute confidence that the τ_d dataset is 100% accurate in terms of identifying dusty cases. Though the sign and magnitude of η_n estimated with τ and τ_d differ, the relative relationship between η_o and η_n estimated with both optical depth datasets are similar to one another. Additionally, the pattern between η_o and η_n is also similar to the relationship between η_o and η_n estimated in the three idealized models (Sections 2.4.1, 2.4.2, and 2.4.3), where locations with positive correlation between τ and q correspond to locations where η_o is more positive than η_n . We note that the spatial structure of η_n for other μ intervals is similar to that shown in Figures 2.6b and d.

Averaging over a broad region of the Sahara Desert (Figure 2.6, black boxes), values of η_n estimated with τ and τ_d are -16.6 ± 5.35 and $-1.41 \pm 4.74 \text{ W m}^{-2} \tau^{-1}$, respectively. In contrast, η_o estimated with the same data and averaged over the same region are -7.85 ± 6.05 and $4.11 \pm 5.34 \text{ W m}^{-2} \tau^{-1}$, for τ and τ_d respectively. The uncertainties in the spatially averaged η are quantified as the absolute value of the difference between the best estimate of η and the spatially averaged upper 95% confidence bound of the slope of the linear least squares regression of Eqs. 2.2 and 2.3 in the assumption that the absolute difference between the best estimate and

each upper and lower bound are equal. Positive biases in η_o relative to η_n are due to positive correlation between dust and water vapor over the Sahara Desert (Figure 2.3). Differences in the estimates of the spatially averaged η_o and η_n estimated from both optical depth datasets strikingly differ. It is possible that these differences occur due to biases between the optical depth datasets. The magnitude of the bias of the temporally averaged τ and τ_d averaged over the Sahara Desert is $|0.043|$ while the maximum magnitude of this bias over the same region is $|0.13|$ (not shown). Since there is not a large discrepancy between the temporally averaged τ and τ_d datasets these results suggest that optical depth outliers and hence changes to the correlation between S^\uparrow and each optical depth, as described previously, can cause considerable changes to the magnitude and sign of η .

Figure 2.7a is a plot of the regionally averaged η_o and η_n estimated with τ for each μ interval over the Sahara Desert. The magnitude of η_o is smallest for $\mu = 0.55$, whereas η_n is smallest for $\mu = 0.45$ (Figure 2.7a). The magnitudes of η_o and η_n are both greatest at $\mu = 0.65$ or $\theta = 49.5^\circ$. The relationship between η and μ arises due to the scattering phase function of dust (Meloni et al., 2005). More specifically, dust primarily scatters in the forward direction so that when μ decreases (θ increases) more SW radiation is scattered in the direction of the upward TOA SW flux. At a low enough μ , the magnitude of η starts to decrease due to reduced solar radiation at these lower μ values (Meloni et al., 2005). Another interesting feature of this figure is that for nearly all μ η_o is more positive than η_n and is consistent with our theory; η_o underestimates the magnitude of η (Figure 2.7) within the Sahara Desert, a region with predominantly positive $r_{\tau,q}$ and $r_{\tau_d,q}$ (Figure 2.3a). The η estimated with τ_d as a function of μ exhibit a similar pattern as η estimated with τ with the exception that the magnitude of η_o and η_n estimated with τ_d are smallest for $\mu = 0.95$ (not shown). Note that the uncertainty in η_o and η_n is largest for $\mu < 0.6$ (Figure 2.7b). The uncertainty is greatest for these μ values because there are less observations available in a majority of the grid-boxes within the Sahara desert for $\mu < 0.6$ (Figure 2.7c). In addition, note that η is undefined for $\mu < 0.45$ because the CERES SSF data only contains θ values that are less than 70° ($\mu > 0.34$). Due to a lack of CERES data

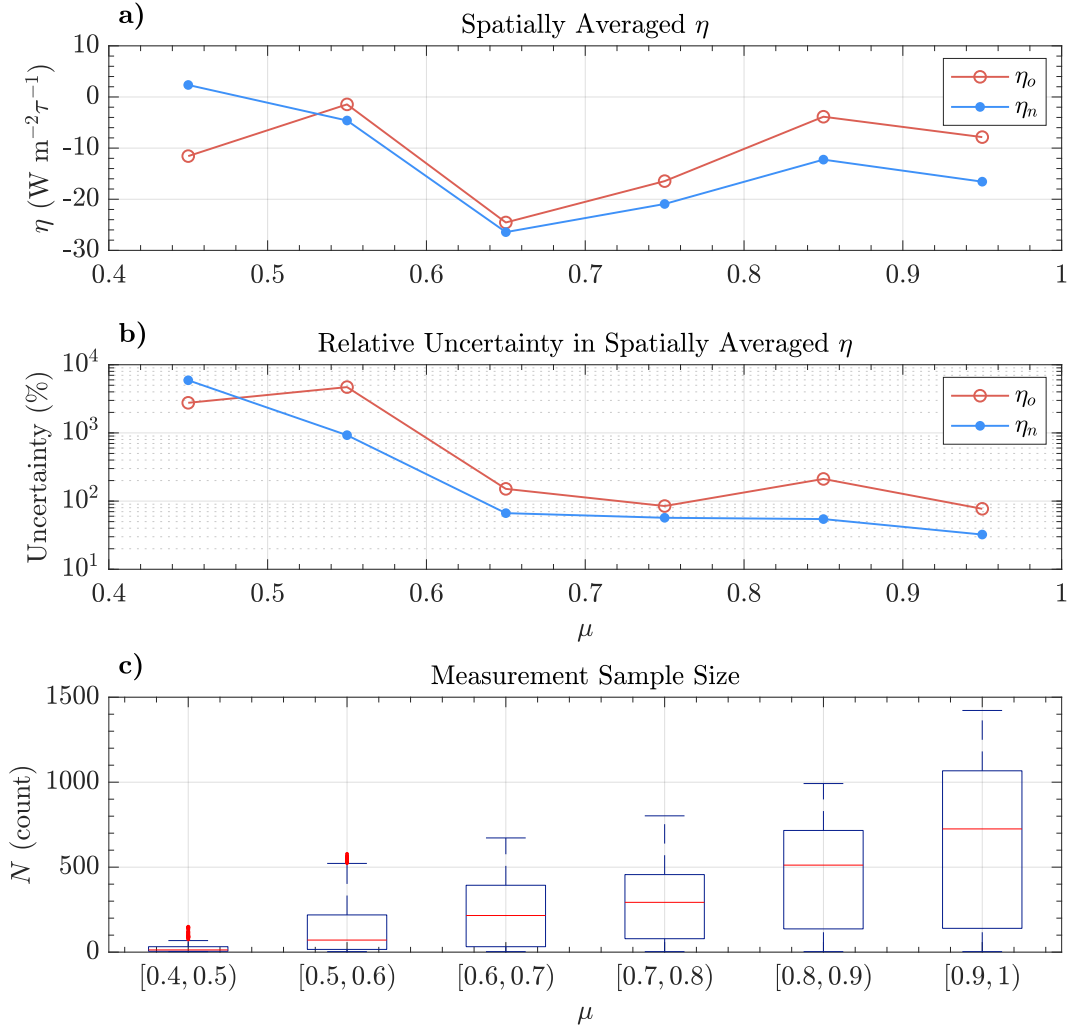


Figure 2.7: The a) spatially averaged η_o (red, open circle) and η_n (blue, closed circle) estimated with τ over the Sahara Desert as a function of the μ bin center for each μ interval. The η uncertainty for each μ interval are plotted in b) for the old (red, open circle) and new (blue, closed circle) methods. Also plotted are the c) box and whisker plots for the sample size (N , count) for each μ interval, which show the median N (red line), outliers (red, closed circles), the 25th and 75th percentiles (bottom and top edges of the boxes, respectively), and the maximum and minimum N (top and bottom whiskers, respectively and excluding outliers). Note that the μ interval labels “[” and “)” represent closed and open intervals, respectively.

corresponding to $\mu > 0.34$ and consequential increase in uncertainty, we do not quantify the diurnally averaged η_o and η_n over the Sahara Desert.

Though there are improvements in the estimation of η via the new method, the relative uncertainties in η_o and η_n are much greater than 10% of the best estimate. It is possible

that uncertainties in the regionally averaged η_o and η_n are high due to the presence of other atmospheric constituents that are correlated to dust (i.e. ozone). Additionally, uncertainties in η may arise due to our methodology, such as uncertainties when using a μ bin width equal to 0.1. Another potential source of uncertainty is the surface albedo α , which may increase the spread between τ and S^\uparrow and thus, increase the magnitude of the uncertainty in the regional η (Yang et al., 2009; Ansell et al., 2014). Further, high surface albedo can cause η to become more positive (Ansell et al., 2014). Note that the seasonal variation of the surface albedo over the Sahara Desert is minimal (Pinty et al., 2000) and that our methodology implicitly averages over seasonal variations in the surface albedo.

2.6.2 Comparison to Other Work

We estimated the regional clear-sky TOA SW η_n over the Sahara Desert for a variety of μ intervals (Table 2.1). In comparison to other studies, Helmert et al. (2007) used a radiative transfer model to estimate the TOA SW η for the southern (10–22°N, 20W–20°E) and northern (22–35°N, 20W–20°E) Sahara Desert as -121 to -94 $\text{W m}^{-2} \text{AOT}^{-1}$, where AOT is the aerosol optical thickness at 500nm, and -55 to -41 $\text{W m}^{-2} \text{AOT}^{-1}$, respectively, for a case study in October of 2001 at 1200 UTC. Our results are more similar to the TOA SW η estimated in Helmert et al. (2007) for the more absorbing dust aerosols (-41 $\text{W m}^{-2} \text{AOT}^{-1}$) over the northern Sahara Desert (Table 2.1). Yang et al. (2009) estimated the TOA SW η over the Sahara Desert (15–20°N, 10°W–30°E) using only observations for June to September 2005–2006 as 1.6 ± 11.3 $\text{W m}^{-2} \text{AOT}^{-1}$, for AOT retrieved at 558nm (Table 2.1). Yang et al. (2009) found a strong relationship between the TOA SW η and the surface albedo, but stated that the relationship is nearly insignificant over surfaces with surface albedo that are extremely high, such as the Sahara Desert. In an effort to reduce the uncertainty in η due to the surface albedo and θ , Tian, Chen, Zhang, and Bi (2021) estimated the TOA SW η for a select number of case studies and grid-boxes within the Sahara Desert. Tian et al. (2021) found that the instantaneous TOA SW η of dust was -39.6 ± 10 $\text{W m}^{-2} \tau^{-1}$ estimated via observations and -32.2 to -44.3 $\text{W m}^{-2} \tau^{-1}$

estimated from both observations and a radiative transfer model. While taking into consideration the η_n uncertainties, our estimates of η_n are not statistically different from those of Yang et al. (2009); though Yang et al. (2009) uses CERES TOA SW fluxes in their analysis and therefore estimate η at similar solar zenith angle θ values as presented in this study, Yang et al. (2009) do not account for θ so a quantitative comparison between the results from Yang et al. (2009) and this study is not possible. The results presented here suggest that η estimated from other studies that do not account for positive water vapor and dust correlation may be more positive than the true η ; yet, Helmert et al. (2007); Tian et al. (2021) obtain more negative values of η than that estimated here. It is unclear why this discrepancy occurs but it is possible that the optical properties used in Helmert et al. (2007); Tian et al. (2021) may not be representative of dust throughout the Sahara Desert. For example the dust optical properties used in Tian et al. (2021) are from only one region in the Sahara Desert. Another possible explanation is that while the η estimated in this study is found using 9 years of satellite data, the radiative transfer and dust model simulations in Helmert et al. (2007) were based on a case study in October 2001 and as a result the estimates of η from Helmert et al. (2007) are not a long term estimate of the clear-sky TOA η of dust. Additionally, these studies do not seem to account for the dependence of the clear-sky TOA SW η of dust on surface albedo and water vapor. Following this limitation η would need to be estimated while holding all other parameters that are correlated to dust constant. The results presented here suggest that it is possible that η estimated from these other studies may need to be re-evaluated. At the least, a more extensive investigation into the correlation between dust and water vapor over the Sahara desert over a long period of time is required in order to make such a comment.

2.7 Conclusion

In this paper, we verified two observation-based methods to estimate the clear-sky TOA SW forcing efficiency η of dust within 8-38° and 20°W-40°E. The old method, based on Satheesh

Table 2.1: Regional clear-sky TOA SW η of dust estimated with τ over the Sahara Desert from this and other studies.

Studies	Time or μ Interval	η ($\text{W m}^{-2}\tau^{-1}$)
This study ^{<i>o</i>} (New method)	$0.9 \leq \mu < 1$	-16.6 ± 5.35
	$0.8 \leq \mu < 0.9$	-12.3 ± 6.68
	$0.7 \leq \mu < 0.8$	-20.9 ± 11.9
Helmert et al. (2007)*	12 UTC	-121 to -94 -55 to -41
Yang et al. (2009) ^{<i>o</i>}	Instantaneous	1.6 ± 11.3
Tian et al. (2021)*, ^{<i>o</i>}	$0.788 \leq \mu \leq 0.848$	-39.6 ± 10 -32.2 to -44.3

super scripts * and *o* denote studies that have used radiative transfer models or observations in their estimations of the η , respectively.

and Ramanathan (2000), involves using linear least squares regression to estimate the clear-sky TOA SW η of dust and assumes that dust is uncorrelated to other atmospheric constituents. We describe the theory of this old method and the physical reasoning for the dependence of the clear-sky TOA SW η of dust on the correlation between dust and water vapor, which is generally due to the competing direct radiative effects of dust and water vapor at the TOA. With this justification, we described the theory of a new method to estimate the clear-sky TOA SW η of dust with the assumption that dust is correlated to water vapor. Next, we applied both observation-based methods to three idealized radiative transfer models. The value in such a method is that we were able to estimate the clear-sky TOA SW η of dust estimated via the old and new methods and compare these estimates to the “true” clear-sky TOA SW η of dust. Further, we applied both observation-based methods in three idealized environments, each with differing levels of complexity. Finally, we used both methods to estimate the instantaneous and regional clear-sky SW η of dust at the TOA over the Sahara Desert (19-30°N, 10°W-30°E).

In order to justify the application of the new method over the Sahara Desert, we used retrievals of daily aerosol optical depth τ and total precipitable water vapor q from the CERES SSF data product and estimates of daily dust optical depth τ_d from Voss and Evan (2020, 2019) from Aqua and Terra to estimate the correlation coefficient between monthly averaged τ and q ($r_{\tau,q}$) and monthly averaged τ_d and q ($r_{\tau_d,q}$) over the Sahara Desert (Figure 2.3). We found

that for a majority of grid-boxes within the Sahara Desert, $r_{\tau,q}$ and $r_{\tau_d,q}$ are significantly and positively correlated (Figure 2.3). The significance of these results is that to our knowledge, the results presented in Figure 2.3 are the first estimates of $r_{\tau,q}$ and $r_{\tau_d,q}$ estimated via a multi-year dataset of τ and q over northern Africa. Since we did not fully investigate the physical causes for a correlation between dust and water vapor over the Sahara Desert, we suggest further study to determine why dust and water vapor would be correlated or anti-correlated over northern Africa. Additionally, we suggest investigation into the dependence of the correlation between dust and water vapor on interannual and intraannual time scales. These possible studies are especially important because water vapor not only impacts the SW part of the electromagnetic spectrum, but it also heavily impacts the clear-sky LW η of dust at the TOA as well; the globally averaged LW η of dust at the TOA is currently thought to be positive and counterbalance the globally averaged TOA SW η of dust (Kok et al., 2017; Di Biagio et al., 2020).

Application of the old and new methods in the linear, two-stream, and Streamer idealized models (Section 2.4) support our hypothesis. More specifically, we found that the old method underestimates the magnitude of the clear-sky TOA SW η of dust when the correlation between dust and water vapor is positive. Additionally, we found that negative biases in the clear-sky TOA SW η of dust estimated via the old method η_o arise when the correlation between dust and water vapor is negative (Figure 2.4). We also found that the magnitude of the biases in the clear-sky TOA SW η of dust estimated via the new method η_n are much less than that of η_o . For example, in the Streamer model the maximum magnitude of the η_o bias is roughly 9-10 times that of η_n (Figure 2.4c). These results suggest that in regions where dust and water vapor are correlated, the magnitude of the observed clear-sky TOA SW η of dust may be underestimated and may need to be re-estimated. It is possible that if these previous estimates are not re-visited, the clear-sky net (i.e. SW + LW) η of dust at the TOA estimated via observations may be more negative than previously thought and, as a result, would contrast with results from more recent studies that found that the global net ζ is weakly negative or near zero (Kok et al., 2017; Di Biagio et al., 2020).

In the Streamer model, we also investigated the relationship between sample size N and the uncertainty of η_o and η_n by estimating the sample size required in order to estimate η_o and η_n with uncertainty less than 10% (N_{10}). We found that for a majority of correlation coefficients between τ_d and water vapor optical depth τ_q (r_{τ_d, τ_q}), N_{10} estimated from the new method is much less than N_{10} estimated from the old method (Figure 2.5). Further, we found that the variation of N_{10} is asymmetrical around r_{τ_d, τ_q} due to the competing direct radiative effects of dust and water vapor at the TOA when $r_{\tau_d, \tau_q} \approx 0.2$ for the old method and due to the overall multivariate linear least squared regression method for the new method.

After verifying the two observation-based methods, we estimated the instantaneous clear-sky SW TOA η of dust over the Sahara Desert from observations and retrievals from the CERES SSF data product and estimates of τ_d from Voss and Evan (2020, 2019) from Aqua and Terra. One main result is that for a majority of grid-boxes over the Sahara Desert for $0.9 \leq \mu < 1$, η_n estimated with τ and τ_d is more negative than η_o estimated with both optical depth datasets (Figure 2.6, Table 2.1) and is consistent with the results from the three idealized radiative transfer models (Figure 2.4). Further, we estimated the variation of the spatially averaged η_o and η_n as a function of μ and found that for all $\mu > 0.5$ the magnitude of η_o is smaller than that of η_n (Figure 2.7a). We also found that the uncertainty of η_n is greater than the uncertainty of η_o , with the exception of $\mu < 0.5$ (Figure 2.7b) and that the η uncertainty increases as the sample size available for each μ interval decreases (Figure 2.7c). The sample size for each μ interval increases as μ increases due to a reduction in the number of measurements from the CERES SSF data product from Aqua and Terra near sunrise and sunset ($\theta > 70^\circ$) over the Sahara Desert. We cannot obtain data near sunrise and sunset because Aqua and Terra are polar orbiting satellites that cross over the Sahara Desert twice a day (i.e. Terra in the morning and Aqua in the afternoon) and as a result, it is difficult to precisely quantify the diurnally averaged η_o and η_n without making assumptions about the variation of η as a function of μ for $0 < \mu < 0.45$. In light of these limitations we suggest further study to estimate the diurnally averaged clear-sky TOA SW η of dust over the Sahara Desert via the old and new methods when more satellite

data is available; for example, recently CERES data onboard the Suomi National Polar-orbiting Partnership (NPP) and NOAA-20 satellites have become available online. Additionally an analysis using clear-sky SW fluxes and optical depths from geostationary satellites could further improve the temporal resolution of the TOA η throughout the day. While taking into account the stated uncertainties in η_n , our results are not statistically different from those published in Yang et al. (2009) ($1.6 \pm 11.3 \text{ W m}^{-2} \tau^{-1}$ over the Sahara Desert). In order to reduce the uncertainty in the instantaneous and spatially averaged η_n presented in this study, we suggest further investigation into the correlation between dust and other atmospheric constituents and estimation of non-linear terms to approximate the clear-sky TOA SW upward flux (i.e. Eq. 2.3).

In this study, we limit our analysis to the regional clear-sky TOA SW η of dust because challenges arise when estimating the global dust SW η . One limitation is that the aerosol contributors to the total τ include aerosols other than dust (i.e. black carbon and sea salt). In order to estimate the global SW η at the TOA for dust only, we would need estimates of τ_d (e.g. Voss & Evan, 2020, 2019). Another challenge is accounting for complications with estimating the dust TOA SW η over land (i.e. surface albedo as described in Yang et al., 2009; Ansell et al., 2014), where τ can be challenging to retrieve over bright surfaces (Hsu et al., 2000). We therefore suggest future work to estimate the globally averaged clear-sky TOA SW η of dust via observations and to apply the new method in locations where dust and water vapor are correlated. These regions may include deserts where dust generation is associated with mesoscale convective systems, monsoonal surges, or haboobs. More broadly, reducing the uncertainty in the clear-sky TOA SW η of dust and further constraining the magnitude of this parameter can aid in determining precisely if and how much dust cools or warms the surface. As a result, the general offset by radiative cooling of aerosols on the warming from greenhouse gasses can be more precisely evaluated and the representation of such forcings can be improved in global climate models.

2.8 Appendix: A

2.8.1 Old Theory

The SW direct radiative effect of mineral dust ζ at the TOA is defined as

$$\zeta = (S^\downarrow - S^\uparrow) - (S^\downarrow - S^\uparrow)_p \quad (2.15)$$

where, S^\downarrow and S^\uparrow are the downward and upward clear-sky SW TOA radiative fluxes, respectively, and the subscript p indicates the pristine-sky fluxes, i.e., fluxes in the absence of aerosols and clouds.

The SW forcing efficiency of dust η is then estimated as the ζ per unit aerosol optical depth τ

$$\eta = \frac{d\zeta}{d\tau}. \quad (2.16)$$

Taking the derivative of Eq. 2.15 with respect to τ and noting that the S^\downarrow is independent of τ , we obtain

$$\eta_o = -\frac{dS^\uparrow}{d\tau} \quad (2.17)$$

where the subscript o refers to the old method for estimating the η , which implicitly assumes that

$$\frac{dS_p^\uparrow}{d\tau} = 0 \quad (2.18)$$

However, we note that this condition is only valid if other atmospheric constituents that affect S^\uparrow are uncorrelated with dust.

We represent S^\uparrow as a linear function of τ ,

$$S^\uparrow = \frac{\partial S^\uparrow}{\partial \tau} \tau + S_p^\uparrow \quad (2.19)$$

where S_p^\uparrow is the upward SW flux at the TOA for a pristine-sky atmosphere. Eq. 2.19 can be solved for $\partial S^\uparrow / \partial \tau$ via linear regression given measurements of τ and S^\uparrow , which is interpreted as $-\eta_o$ (Eq. 2.17). A number of studies have used such an approach to observationally estimate dust η over various regions, including the Saharan Desert (e.g. Hsu et al., 2000).

2.8.2 New Theory

Since water vapor absorbs SW radiation, if q and τ are positively correlated Eq. 2.17 will produce an estimate of η that is too small in magnitude. For this case, $dS_p^\uparrow / d\tau \neq 0$ and thus, the derivative of Eq. 2.15 with respect to τ (Eq. 2.16), becomes

$$\eta = -\frac{dS^\uparrow}{d\tau} + \frac{dS_p^\uparrow}{d\tau} \quad (2.20)$$

If we assume that S^\uparrow is instead a function of τ and q , rather than a function of τ alone (Eq. 2.19), then the linearized equation for the upwelling solar radiation is

$$S^\uparrow = \left(\frac{\partial S^\uparrow}{\partial \tau} \right)_q \tau + \left(\frac{\partial S^\uparrow}{\partial q} \right)_\tau q + S_{p,dry}^\uparrow \quad (2.21)$$

where $(\)_q$ and $(\)_\tau$ indicate partial derivatives with q or τ held constant, respectively, and $S_{p,dry}^\uparrow$ is the upward SW flux at the TOA for a pristine and completely dry atmosphere. The derivative of Eq. 2.21 with respect to τ is

$$\frac{dS^\uparrow}{d\tau} = \left(\frac{\partial S^\uparrow}{\partial \tau} \right)_q + \left(\frac{\partial S^\uparrow}{\partial q} \right)_\tau \frac{dq}{d\tau} \quad (2.22)$$

which can then be substituted into the estimation of η (Eq. 2.20),

$$\eta = -\left(\frac{\partial S^\uparrow}{\partial \tau} \right)_q - \left(\frac{\partial S^\uparrow}{\partial q} \right)_\tau \frac{dq}{d\tau} + \frac{\partial S_p^\uparrow}{\partial q} \frac{dq}{d\tau} \quad (2.23)$$

where we have represented the pristine-sky fluxes as a linear function of q ,

$$S_p^\uparrow = \frac{\partial S_p^\uparrow}{\partial q} q + S_{p,dry}^\uparrow. \quad (2.24)$$

Recognizing that

$$\left(\frac{\partial S^\uparrow}{\partial q} \right)_\tau = \frac{\partial S_p^\uparrow}{\partial q}. \quad (2.25)$$

We re-estimate a new η for the case where water vapor concentrations are correlated with τ_d ,

$$\eta_n = - \left(\frac{\partial S^\uparrow}{\partial \tau} \right)_q \quad (2.26)$$

which can be estimated via multivariate linear regression and measurements of S^\uparrow , τ , and q (Eq. 2.21). This estimation is referred to as the new η , η_n .

2.9 Appendix: B

In this section we test the old and new methods to estimate the dust forcing efficiency η in a more comprehensive, radiative transfer model. Firstly, we describe the design of the model experiments (Section 2.9.1). We then evaluate the biases in the old (Appendix 2.8.1) and new methods (Appendix 2.8.2) in Section 2.9.2.

2.9.1 Streamer Radiative Transfer Model

In order to generate results that are more representative of conditions over the Sahara Desert, we force Streamer (Key & Schweiger, 1998) with time series of daily mean values of aerosol optical depth τ , total precipitable water vapor q , and solar zenith angle θ from the CERES SSF data product from 2010–2019 from Aqua (Section 2.2.1). To reduce the complexity of the analysis we assume a perpetual diurnal cycle of solar radiation corresponding to June 15th.

From Streamer we obtain clear-sky and pristine-sky TOA SW upward and downward fluxes for each 1° grid-box in the study area ($8 - 38^\circ\text{N}$, $20^\circ\text{W} - 40^\circ\text{E}$). Using these fluxes and the CERES SSF data we estimate η via the old (η_o) and new (η_n) methods following the theory described in Sections 2.3.1 and 2.3.3, respectively.

In order to evaluate the biases in the old and new methods, we compare η_o and η_n to the “true” η via Eq. 2.16 (η_t) where τ is from MODIS. To remain consistent with the methodology to quantify η_t in the linear and two-stream idealized models, we estimate η_t via linear least squares regression of τ onto the “true” direct radiative effect ζ quantified via Eq. 2.15.

2.9.2 Forcing Efficiency

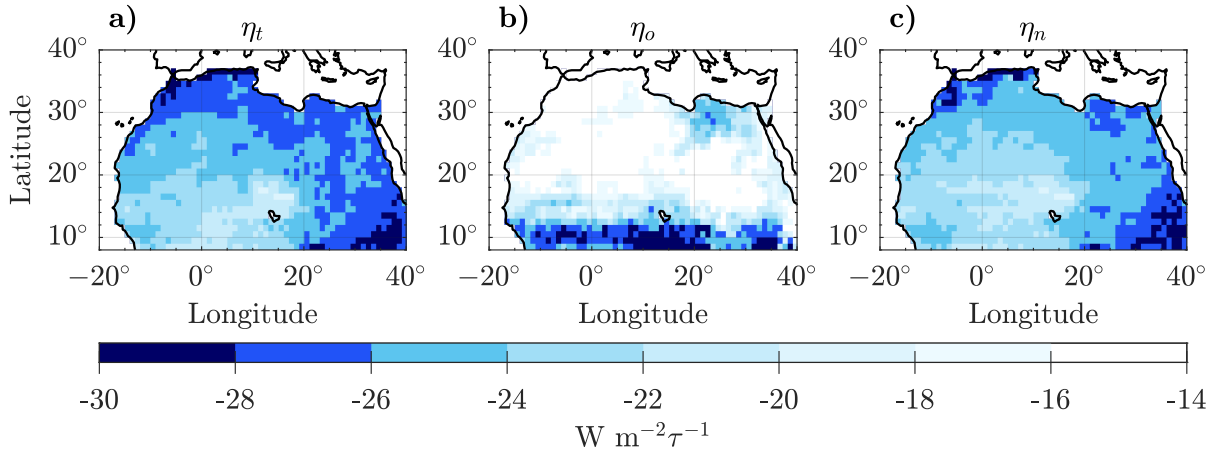


Figure 2.8: Maps of (a) η_t , (b) η_o , and (c) η_n over all land grid-boxes within $8-38^\circ\text{N}$, $20^\circ\text{W}-40^\circ\text{E}$. All of the estimated values of η ($\text{W m}^{-2}\tau^{-1}$) are represented by the same color scale. White depicts areas where the η is equal to the spatial mode of η_t ($-26.0 \text{ W m}^{-2}\tau^{-1}$).

Figure 2.8 shows η_t , η_o , and η_n over all land grid-boxes within the study area ($8-38^\circ\text{N}$, $20^\circ\text{W}-40^\circ\text{E}$). All η estimates are negative which is expected because dust strongly scatters SW radiation. The spatial distribution of η_t (Figure 2.8a) is relatively uniform with a regional mean of $-25.1 \text{ W m}^{-2}\tau^{-1}$ and a standard deviation of $1.90 \text{ W m}^{-2}\tau^{-1}$ (7.57%). The minimum and maximum values of η_t are -30.2 and $-19.5 \text{ W m}^{-2}\tau^{-1}$, respectively. It is unsurprising that the spatial variation in η_t is small since we only change the dust and water vapor concentrations in the Streamer simulations (i.e. the dust optical properties are homogeneous in space). In contrast

the magnitude of η_o (Figure 2.8b) differs across the study area as depicted by the high regional (mean $-18.4 \text{ W m}^{-2}\tau^{-1}$) standard deviation, which is equal to $5.56 \text{ W m}^{-2}\tau^{-1}$ (30.2%). The magnitude of η_o is smallest north of 12°N within 18°W – 37°E and within 8 – 18°N , 37 – 40°E . The magnitude of η_o reaches a minimum of roughly $-1.80 \text{ W m}^{-2}\tau^{-1}$ at around 36°N , 2°E and along the northern and northwestern coasts of Algeria and Morocco, respectively. The magnitude of η_o reaches a maximum of $-37.9 \text{ W m}^{-2}\tau^{-1}$ at around 8°N , 22°E while the magnitude of η_o high in the Sahel (Figure 2.8b). In regards to the new method the spatial distribution of η_n (Figure 2.8c) is almost uniform with latitude. The regional mean and standard deviation of η_n are -24.5 and $1.90 \text{ W m}^{-2}\tau^{-1}$, respectively. Areas with the most positive values of η_n occur at around 16°N , 16°E ($\eta_n = -19.6 \text{ W m}^{-2}\tau^{-1}$) (Figure 2.8c). More negative values of η_n occur east of 35°E and over the coasts of northern and northwestern Algeria and Morocco, respectively ($\eta_n = -30.8 \text{ W m}^{-2}\tau^{-1}$).

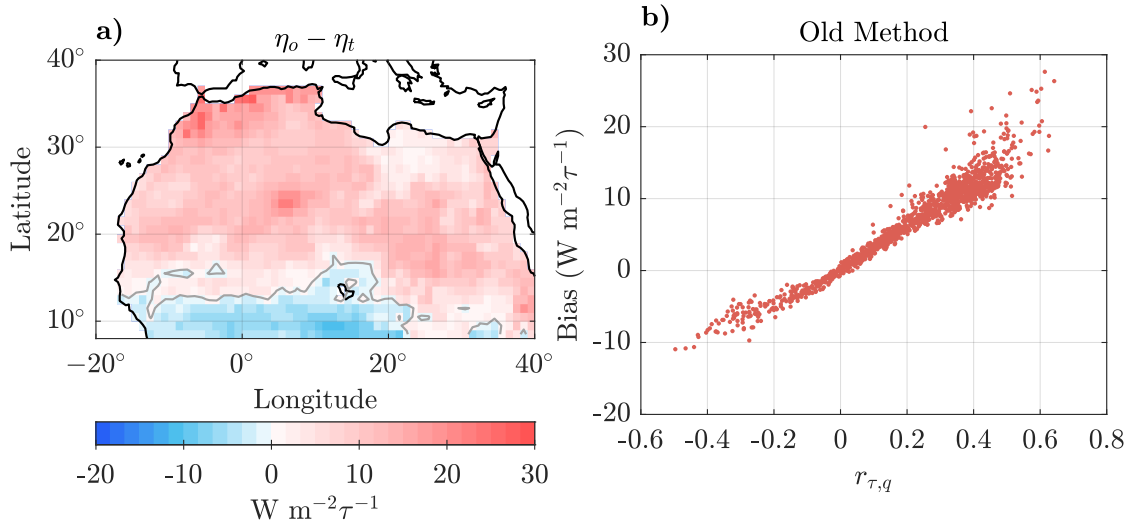


Figure 2.9: Shown is a (a) map of the η_o bias (colors, in $\text{W m}^{-2}\tau^{-1}$). The gray contour line indicates areas where the η_o bias is equal to zero. Also shown is a (b) scatter plot of the η_o bias ($\text{W m}^{-2}\tau^{-1}$) as a function of the correlation coefficient between τ and q ($r_{\tau,q}$).

Generally positive and negative biases in η_o occur northward and southward, respectively, of approximately 12°N (Figure 2.9a). The largest positive bias in η_o is equal to $27.6 \text{ W m}^{-2}\tau^{-1}$ and occurs at around 36°N , 2°E . Strong negative biases occur south of 10°N , 10° – 20°E . Within

this region the largest negative bias in η_o occurs at around 9°N, 13°E as $-10.9 \text{ W m}^{-2}\tau^{-1}$ (Figure 2.9a). Over northern Africa the regional mean η_o bias is positive ($6.76 \text{ W m}^{-2}\tau^{-1}$) and the standard deviation is 95.4%. The spatial distribution of η_o bias most resembles that of the correlation coefficient between τ and q ($r_{\tau,q}$, Figure 2.3), where the strongest similarities occur north of approximately 12°N, 18°W–23°E. If we consider the relationship between η_o bias and $r_{\tau,q}$ (Figure 2.9b) there is high, positive correlation between η_o bias and $r_{\tau,q}$ (r -value = 0.967, p -value < 0.01). This finding is consistent with our theory in that η estimated with the old method exhibit biases when water vapor and dust are strongly correlated to one another. This is due to the competing radiative effects of water vapor and dust in the SW and at the TOA which causes the magnitude of η_o to be under or over estimated depending on the sign of $r_{\tau,q}$. Note that biases in η_o approach zero when $r_{\tau,q} \sim 0$ (Figure 2.9b).

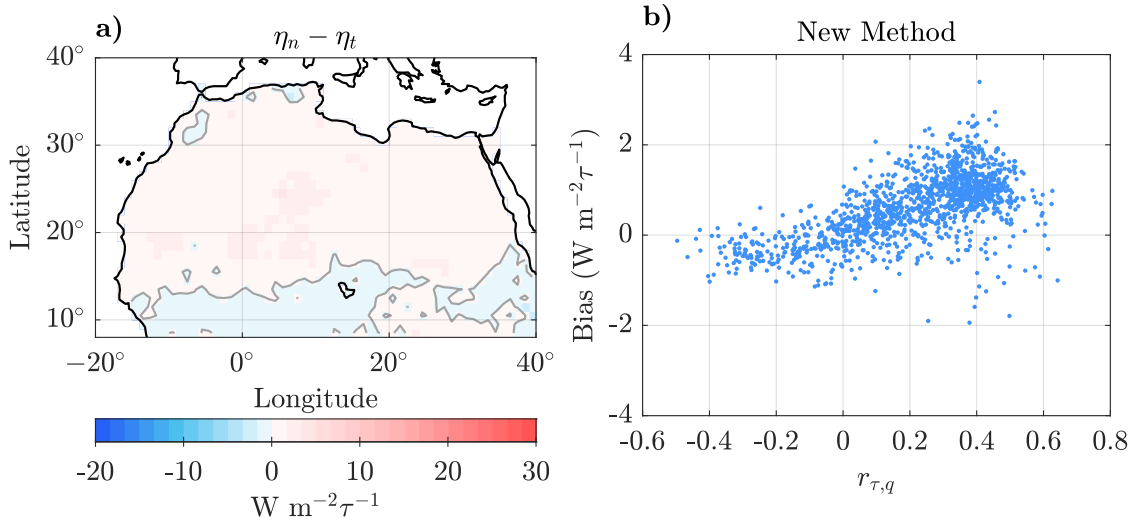


Figure 2.10: Shown is a (a) map of the η_n bias (colors, in $\text{W m}^{-2}\tau^{-1}$) with the same colorbar as Figure 2.9a. The gray contour line indicates where the η bias is equal to zero. Also shown is a (b) scatter plot of the η_n bias ($\text{W m}^{-2}\tau^{-1}$) as a function of the correlation coefficient between τ and q ($r_{\tau,q}$). Note that Figure 2.10a has the same colorbar as Figure 2.9a.

The spatial distribution of the bias in η_n is more uniform than that of the old method (Figure 2.10a). Positive biases in η_n occur approximately north of 12°N, 17°W–25°E and throughout most of Egypt and Sudan, with the exception in southeastern Sudan. The regional mean and standard deviation of the η_n biases are 0.616 and 0.733 $\text{W m}^{-2}\tau^{-1}$, respectively.

The bias in η_n is maximum ($3.39 \text{ W m}^{-2}\tau^{-1}$) at around 25°N , 6°E while reaching its most negative value of $-1.94 \text{ W m}^{-2}\tau^{-1}$ at around 11°N , 39°E . In roughly half of the grid-boxes the magnitude of the bias in η_n is roughly 1/8 the magnitude of the bias in η_o . In consideration of the scatter between the bias in η_n and $r_{\tau,q}$, there is weak correlation between η_n bias and $r_{\tau,q}$ (r -value = 0.61, p -value ≤ 0.01). These results are similar to that found from the linear, 2-stream, and Streamer models (Figure 2.4) and suggest that in locations where dust and water vapor are correlated using the new method to estimate the clear-sky dust SW η at the TOA can reduce biases in η .

2.10 Acknowledgments

Funding for this work was provided by NSF Award AGS-1833173. We would like to thank three anonymous reviewers for their suggestions on the first submission of this paper.

CERES SSF level 2 edition 4A data (NASA/LARC/SD/ASDC, 2014a, 2014f) used in this study were obtained from the Atmospheric Science Data Center at the NASA Langley Research Center (<https://ceres.larc.nasa.gov/data/>). Streamer source code is available publicly from <http://stratus.ssec.wisc.edu/streamer/> (Key & Schweiger, 2013). Estimates of the dust optical depth used in this study from Voss and Evan (2020) are publicly available at <https://doi.pangaea.de/10.1594/PANGAEA.909140> (Voss & Evan, 2019).

Chapter 2, in part, is a reprint of the material as it appears in Journal of Geophysical Research: Atmospheres. Kuwano, A., and Evan, A. (2022). A method to account for the impact of water vapor on observation-based estimates of the clear-sky shortwave direct radiative effect of mineral dust. Journal of Geophysical Research: Atmospheres, 127 (17), doi:<https://doi.org/10.1029/2022JD036620>. The dissertation author was the primary author of this paper.

Chapter 3

Quantifying the Dust Direct Radiative Effect in the Southwestern United States: Findings from Novel Measurements

Mineral aerosols (i.e. dust) perturb the Earth's energy budget by scattering and absorbing shortwave (SW) and longwave (LW) radiation, which can be described as the direct radiative effect. Generally dust has a net (SW + LW) negative direct radiative effect, which is the difference between clear-sky (cloud-free) and pristine-sky (cloud and dust-free) net flux, at the top of the atmosphere. Thus, dust tends to induce an overall cooling effect on the Earth's climate system. Though there has been work to constrain the direct radiative effect of dust, there are few estimates of the dust direct radiative effect over small dust source regions and the sign of the dust direct radiative effect at the top of the atmosphere is still uncertain. In an effort to reduce uncertainties of this parameter over such regions, we use two independent methods - a model method and an observation-based method - to estimate the surface and top of the atmosphere SW forcing efficiency, the direct radiative effect normalized by the aerosol optical depth, over a dust source region in the northwestern Sonoran Desert in the Salton Basin. After validating a radiative transfer model we find that the estimates of the dust SW forcing efficiency via these independent methods are statistically similar. Next we apply the model method to estimate the LW forcing efficiency of dust and the diurnally averaged net forcing efficiency at the surface and top of the atmosphere. Estimates of the diurnally averaged net forcing efficiency of dust over the Salton

Basin are -29 ± 10 , -10 ± 11 , and $19 \pm 15 \text{ W m}^{-2}$ per optical depth at the surface, top of the atmosphere, and atmosphere, respectively. We find that the sign of the diurnally averaged net forcing efficiency is constrained at the surface and atmosphere, suggesting that dust induces a cooling effect at the surface and a warming effect within the atmosphere. These results have implications for semi-direct effects of dust on the climate system, which can affect local weather patterns and dust feedbacks.

3.1 Introduction

Mineral aerosols (i.e. dust) account for the majority of aerosol mass in the Earth's atmosphere (Gliß et al., 2021) and there are a number of mechanisms by which dust interacts with the Earth's climate system (Kok et al., 2023). For example dust alters the Earth's energy budget by directly absorbing or scattering shortwave (SW) or longwave (LW) radiation (Sokolik & Toon, 1996). Dust indirectly affects the Earth's energy budget by altering ice cloud development since dust is an ice nuclei (DeMott et al., 2003; Sassen et al., 2003; DeMott et al., 2010; Rosenfeld, Rudich, & Lahav, 2001), thereby altering the reflectivity of clouds. Through absorption of SW and LW radiation, dust can alter the atmospheric temperature profile and induce semi-direct effects on the Earth's energy budget (Helmert et al., 2007; Johnson et al., 2004) or perpetuate feedbacks within the Earth's climate system (Helmert et al., 2007; Kok, Ward, Mahowald, & Evan, 2018). On a broader scale the direct effect of dust contributes towards the total aerosol direct effect on the Earth's energy budget of which is still uncertain (IPCC, 2014).

In this study we focus on the dust direct radiative effect, *DRE*, which is the difference between the net flux in clear-sky (cloud free and dust laden) and pristine-sky (cloud and dust free) conditions. In the SW spectrum dust typically cools the Earth's surface and top of the atmosphere (TOA) while in the LW dust generally induces a warming effect (Liao & Seinfeld, 1998). Di Biagio et al. (2020) and Kok et al. (2017) used observations to constrain a radiative transfer model (RTM) and quantified the globally averaged TOA *DRE* of dust ranging from

-0.85 to -0.04 W m^{-2} in the SW and 0.07 to 0.59 W m^{-2} in the LW, resulting in a net (SW + LW) dust *DRE* ranging from -0.6 to 0.23 W m^{-2} . As demonstrated from Di Biagio et al. (2020) and Kok et al. (2017) the sign of the globally averaged net *DRE* of dust at the TOA is unconstrained. One of the reasons for this outcome is because the typical method to estimate the dust *DRE* (i.e. through an RTM) requires knowledge of dusts' optical and microphysical properties, which can vary widely as a function of space and time (Di Biagio et al., 2019, 2020; Kok et al., 2017; Song et al., 2022). For example Di Biagio et al. (2017) and Di Biagio et al. (2019) found that the magnitude and spectral dependency of the imaginary part of the complex refractive index - a measure of how much a constituent absorbs radiation - is highly dependent on dust mineralogy; in particular, the relative concentration of the minerals that efficiently absorb SW and LW radiation (i.e. iron oxides, clays, quartz, and calcite) differ among dust source regions in North Africa, North America, Asia, and Australia (Di Biagio et al., 2017; Di Biagio et al., 2019). In regards to dust size many regional and global circulation models underestimate, if at all include, the amount of coarse dust particles in their schemes (Zhao, Ryder, & Wilcox, 2022; Adebisi & Kok, 2020; Kok et al., 2017) and as a result can lead to an underestimation of the magnitude of SW cooling or LW warming induced by dust (Kok et al., 2017; Song et al., 2018). This challenge is especially critical since recent *in-situ* measurements of dust size distribution show that larger dust particles are found higher in the atmosphere or at a distance from dust source regions (Ryder et al., 2018, 2019; van der Does et al., 2018) which cannot be explained via gravitational settling (Adebisi & Kok, 2020; Ryder et al., 2019). Furthermore dust is aspherical (Okada, Heintzenberg, Kai, & Qin, 2001; Chou et al., 2008; Kandler et al., 2009; Huang et al., 2020) and challenging to precisely characterize and measure (Huang, Kok, Saito, & Muñoz, 2023). By assuming that dust is spherical, both quantified and retrieved values of the optical properties of dust can be underestimated. If the total extinction by dust is underestimated the magnitude of the dust *DRE* in the SW and LW spectrums can also be underestimated (Huang et al., 2023). To further complicate matters, these properties can be challenging to fully incorporate into an RTM because the instrumentation required to collect these parameters can be expensive

or physically challenging to maintain in remote dust source regions over a long period of time. This limitation can lead to scarce, if any, datasets of the relevant optical and physical parameters used as inputs into RTMs that are fully representative of the dust properties in a specific region.

In order to avoid making assumptions about dusts' optical and microphysical properties in an RTM, a number of studies used observations of fluxes and retrievals of dust physical properties to obtain observation-based estimates of the surface and TOA dust *DRE* in the SW (e.g. Hsu et al., 2000; Di Biagio et al., 2009, 2010; J. Haywood et al., 2003; Yang et al., 2009; Kuwano & Evan, 2022) and LW (e.g. Brindley, 2007; Brindley & Russell, 2009; Zhang & Christopher, 2003) spectrums. Since the main challenge with using observations to estimate the clear-sky SW and LW *DRE* of dust is that pristine-sky fluxes can rarely, if at all, be measured, the observational method involves estimating the dust forcing efficiency *FE*, the *DRE* normalized by the aerosol optical depth τ . Several studies estimated the *FE* of dust at the surface and TOA using the direct method from Satheesh and Ramanathan (2000) in the SW (e.g. Di Biagio et al., 2009, 2010; Kuwano & Evan, 2022; Song et al., 2018) and an observational method from Brindley (2007); Brindley and Russell (2009) in the LW, both of which can be described as statistical and observational methods. Uncertainties related to this observational method include instrumental and retrieval uncertainty, uncertainty related to the correlation between dust and other atmospheric constituents, and the sample size available for the analysis (Satheesh & Ramanathan, 2000). Another challenge with the observational method is that dust laden scenes need to be identified because aerosols other than dust may be present in the atmosphere. A challenge with estimating the LW *FE* of dust is that LW fluxes are highly dependent on water vapor, surface temperature, and the vertical distribution of dust and temperature in the atmosphere (Brindley, 2007; Brindley & Russell, 2009). Obtaining retrievals or observations of these parameters often requires additional instrumentation and an extensive analysis to fully understand the relationship between the LW fluxes and the additional parameters.

In this study we use two independent methods to estimate the clear-sky surface, atmospheric, and TOA SW *FE* of dust in the Salton Basin, a depression in southeastern California.

The first method involves using solely ground and satellite based measurements in the observational method from Satheesh and Ramanathan (2000); Kuwano and Evan (2022) to estimate the surface and TOA SW *FE* of dust. The second method entails constraining the relevant dust optical and microphysical parameters in an RTM (hereby the model method) to estimate both the SW dust *DRE* and *FE* at the surface and TOA. The main incentives to estimating the SW *DRE* and *FE* with both the observational and model methods is so that we can validate our estimates of the clear-sky SW *FE* of dust and apply the model method to estimate the LW and diurnally averaged *FE* of dust. We do not include an observation-based estimate of the LW *FE* and *DRE* due to complications with using only observations to estimate the LW component.

We conduct this study in the Salton Basin because the Salton Sea and Imperial Valley experience frequent, intense dust storms (A. T. Evan, 2019). There is also a field site just west of the Salton Sea shoreline with instrumentation to measure the relevant properties required for the model and observational method and is located downwind of much of the active dust emitting sources in the region. It is also predicted that the Salton Basin will become more dusty over the next several years as the Salton Sea shrinks (Poudel, Ahmad, & Stephen, 2021) due to water being redirected in 2017 (San Diego County Water Authority, n.d.). Exposed dried up playa can become an additional dust (Imperial Irrigation District, 2016) and pollution (Jones & Fleck, 2020) source. To the best of our knowledge, this is the first study to derive observation-based and model estimates of the SW and LW *DRE* and *FE* of dust in North America.

The remaining portion of this paper is structured as follows. In Section 3.2 we describe the field site and relevant instrumentation (Table 3.1). We then describe and validate the RTM used in this study (Section 3.3). In Section 3.4 we describe the theory of the model and observational methods to estimate the surface and TOA *FE* of dust and further justify the observational method. In Section 3.5 we use the observational and model methods to estimate the clear-sky instantaneous SW *FE* of dust at the surface, TOA, and atmosphere. In addition we use the model method to estimate the instantaneous LW *FE* of dust. Next we derive the diurnal cycles of SW and LW *FE* and estimate the diurnally averaged SW, LW, and net *FE* of dust at the surface,

TOA, and atmosphere. We then compare our estimates of the SW and LW *FE* of dust to that from other studies. We conclude with a summary and conclusion in Section 3.6.

3.2 Data Sets and Products

In this section we describe the *in-situ* (Section 3.2.1) and satellite (Section 3.2.2) datasets, the field site (Section 3.2.1), other datasets (Section 3.2.3), and the instrumentation used in this study. Instrumentation and corresponding measurements, retrievals, and their respective uncertainties are listed in Table 3.1. Next we describe how we identify dusty conditions at the field site (Section 3.2.4) and the surface soil mineralogy (Section 3.2.5), of which the dust optical properties are based on.

3.2.1 Field Site Description, Instruments, and Products

We obtain *in-situ* observations and retrievals from the Scripps Institution of Oceanography (SIO) field site in the Salton Basin in southeastern California (white square, 33.169°N, 115.856°W in Figure 3.1) from 2020–2022. The Salton Basin can be characterized as a semi-arid region with an average annual rainfall of 81 mm (Stephen & Gorsline, 1975) and elevations below sea level (Ives, 1949). The field site is northeast of Imperial Valley, a major agricultural and metropolitan center of southeastern California, and east of the Anza-Borrego Desert State Park (Figure 3.1). The field site rests on the eastern edge of an orchard and is roughly 2.5 km west of the western shoreline of the Salton Sea (Figure 3.1). During the summer surface temperatures can reach values greater than 100°F while in the winter, temperatures are moderately cool and can fall below freezing at night (Ives, 1949; Imperial County Air Pollution Control District, 2018). The general morphology of the Salton Basin include alluvial fans, sand dunes, badlands, dry washes, offshore playa, rocks, and scattered vegetation (Stephen & Gorsline, 1975; Imperial Irrigation District, 2016). The major aerosol species that reside in the Salton Basin include dust, pollution from Mexico (Imperial County Air Pollution Control District, 2018), and smoke from agricultural or wild fires.

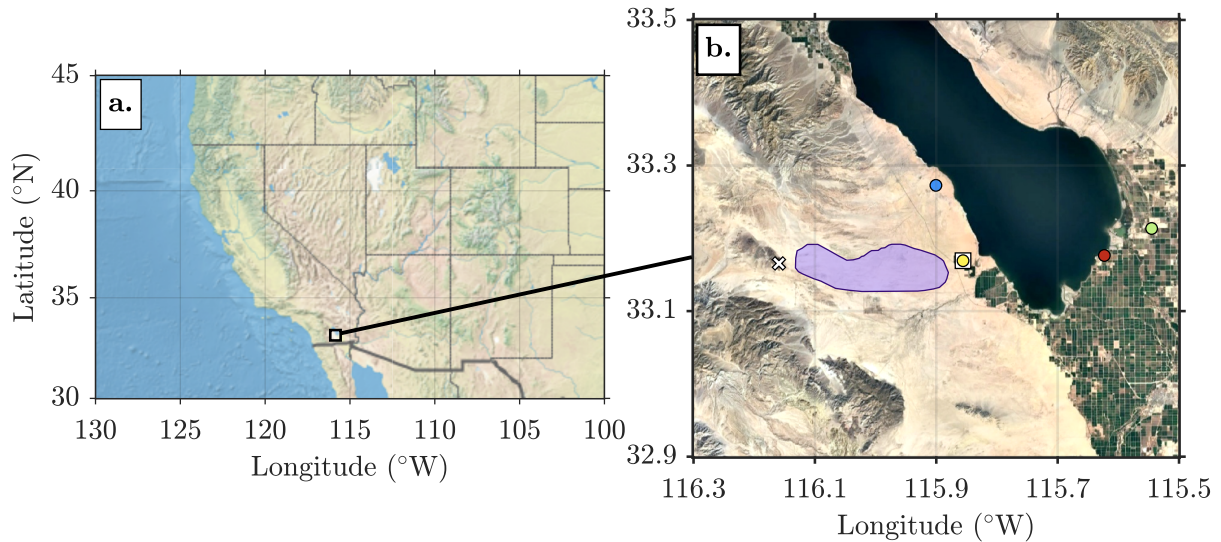


Figure 3.1: A map of (a) California and the (b) regions surrounding the Salton Sea. Also plotted is the location of the field site (white square). The red, yellow, green, and blue closed circles represent the locations of the monitoring stations Sonny Bono, Naval Test Base, Niland-English Road, and Salton City, respectively. The region enclosed by the purple polygon is the area used to obtain the soil mineralogy from satellite retrievals (Section 3.2.5). South of the Salton Sea is Imperial Valley. The satellite image in (b) was obtained from Google Earth on August 26, 2023.

Solar and Infrared Radiometers

We obtain the surface SW upward and downward fluxes from two Kipp and Zonen CM21 pyranometers (3A, Figure 3.2) that measure the broadband SW flux from 0.2–4 μm . These SW fluxes are acquired every second and averaged over 1 minute. The CM21 pyranometers exhibit small cosine offsets with a typical maximum error of 3% at high solar zenith angle θ values (“CM21 Precision Pyranometer Instruction Manual”, 2004; Ramana & Ramanathan, 2006). One pyranometer was factory calibrated on July 23, 2018 at the Kipp and Zonen headquarters in Delft, the Netherlands and February 24, 2023 in Sterling, Virginia by an authorized calibration partner. This pyranometer holds a calibration classification of ISO 9060, Secondary Standard with a total instrument calibration uncertainty of $\pm 1.32\%$ (2018) and $\pm 1.35\%$ (2023). The other pyranometer is calibrated against the factory-calibrated pyranometer during clear-sky and daytime conditions and over the following four time periods: October 2019, September 2020, September 2021, and April 2023. During the first two and last time periods the cross-calibration

procedure is conducted in La Jolla (32.8688°N, 117.2513°W); during September 2022 the non-calibrated pyranometer is calibrated at the SIO field site (described in Section 3.2.1). From November 2019–June 2021 and September 2021–current the factory-calibrated pyranometer was downward and upward facing, respectively, and was outfitted with a CV2 Kipp and Zonen ventilation unit cover; we do not fully run the CV2 units since there is little water vapor present in this region. In this study we obtain minute-averaged surface measurements of the SW flux in the upward and downward direction from 2020–2022.

We obtain surface LW upward and downward fluxes from Kipp and Zonen CG4 (2A in Figure 3.2) and CGR4 pyrgeometers (1A in Figure 3.2), respectively, from 2020–2022 (Table 3.1). These radiometers measure broadband LW flux from 4.5–42 μm (“CG4 Pyrgeometer Instruction Manual”, 2001) and are outfitted with Pt-100 thermistors to measure instrument body temperature. The Kipp and Zonen CG4 and CGR4 pyrgeometers have uncertainties of roughly $\pm 4 - 5\%$ (Table 3.1) and LW fluxes are acquired every second and averaged over 1 minute intervals. The CGR4 pyrgeometer was factory-calibrated at the Kipp and Zonen headquarters in Delft, the Netherlands on July 16, 2018 and March 28, 2023. Throughout the study time period the CGR4 pyrgeometer is facing upward and outfitted with a CV2 unit cover. The CG4 pyrgeometer is cross-calibrated against the factory-calibrated pyrgeometer from October 30–November 11, 2019 in La Jolla; August 9–September 13, 2021 in La Jolla; and April 21–May 2, 2023 at the field site. Details of such calibration are in Section 3.2.1. Here we obtain minute-averaged surface measurements of the upward and downward LW flux from 2020–2022.

Pyranometer Calibration Procedure

Factory-calibrated pyranometers are typically calibrated against a reference pyranometer under an artificial light in a dark room on a rotating table. One pyranometer was calibrated under this procedure (hereafter, the factory-calibrated pyranometer) at the Kipp and Zonen facility on July 23, 2018 and from an authorized party on February 24, 2023. Calibration results are available in the supplement (Section S3.8, Figure S3.23).

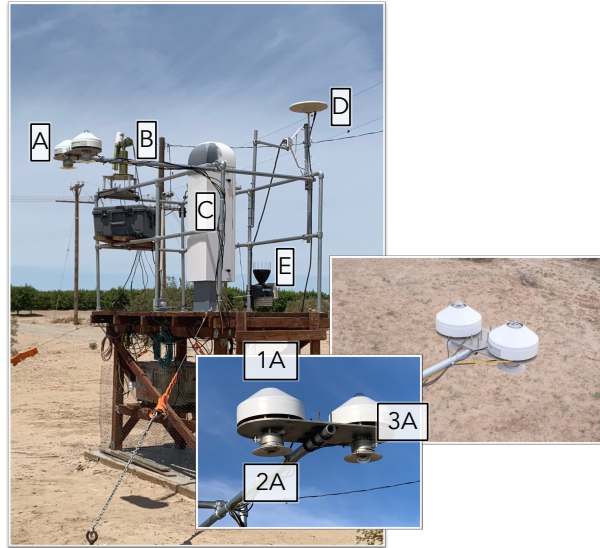


Figure 3.2: The instrumentation available at the Scripps Institution of Oceanography (SIO) field site (white square, Figure 3.1) in the Salton Basin. The instruments marked with an “A” represent the radiometers (“1A” = CGR4 pyrgeometer, “2A” = CG4 pyrgeometer, and “3A” = CM21 pyranometer). The location of the CMIEL sun photometer is represented by the “B” marker while the location of the CL51 ceilometer is denoted by “C”. The locations of the GPS system and met station are represented by the “D” and “E” markers, respectively.

We cross calibrated the other pyranometer during daytime, cloud-free, and aerosol-free conditions at SIO in La Jolla from October 9–10, 2019; August 5–September 13th, 2021; and March 6–April 22, 2023; between August 17–23, 2022 we cross calibrated this pyranometer at the SIO field site under the same conditions. The advantage to calibrating this pyranometer (hereafter, the field-calibrated pyranometer) in La Jolla is that it was easy to maintain and monitor the radiometers during calibration; the disadvantage, however, was that La Jolla can oftentimes be cloudy. Scattering effects induced by the presence of clouds and aerosols may cause high variability of the measured surface solar flux and lead to biases in cross-calibration. Cross calibrating the field-calibrated pyranometer at the field site eliminated the challenge with collecting calibration data during cloud-free conditions.

After filtering for daytime, cloud-free, and aerosol-free conditions we estimate the cross calibration coefficient for each calibration time period by calculating the slope of the linear least squares regression of the surface SW downward flux measured from the factory-

calibrated pyranometer onto the outputted voltage of the field-calibrated instrument (Figure S3.23). Before calibration we remove outliers and, to remain consistent with the Kipp and Zonen CM21 pyranometer manual, we perform the regression without a y-intercept. Values of the calibration coefficient for the cross calibration are in the supplement (Section S3.8, Figure S3.23). Next we generate a time series of the calibration coefficients for both pyranometers by linearly interpolating the calibration coefficients from before, during, and after 2019–2022. Finally we apply these time series to the voltage outputs of both pyranometers to generate SW fluxes from 2019–2022.

Pyrgeometer Calibration

In this section we describe the cross-calibration procedure for the CG4 pyrgeometer. The CGR4 pyrgeometer was factory calibrated on July 16th, 2018 and March 28th, 2023 at the Kipp and Zonen headquarters in Deft the Netherlands (results shown in the supplemental, Section S3.8 and Figure 3.24). The typical calibration procedure for Kipp and Zonen pyrgeometers includes a cross calibration with the pyrgeometer output (in mV) and reference pyrgeometer (in W m^{-2}) at nighttime during clear-sky conditions. The calibration coefficient is estimated via the best fit of the reference and uncalibrated pyrgeometer output. One of the criteria for the calibration is that the LW downward flux measured by the reference and uncalibrated pyrgeometers do not differ by more than $|5| \text{ W m}^{-2}$.

In this study we perform the cross-calibration of the CG4 pyrgeometer with the reference factory calibrated CGR4 pyrgeometer during the following three time periods: October 30–November 11, 2019; August 9–September 13, 2021; and April 21–May 2, 2023. For each time period we orient the radiometers side by side on the roof of a building at SIO in La Jolla. During the last calibration time period the CG4 pyrgeometer is calibrated against the CGR4 pyrgeometer at the field site.

During the calibration procedure the pyrgeometer output is averaged every minute. We then filter for cloudy (and, at the field site, dusty) conditions by eliminating data where the

minute range is larger than 1 W m^{-2} . We did not limit our calibration to nighttime data because we did not find a significant advantage to using only nighttime data and found large biases in the LW downward flux after applying a nighttime calibration coefficient. We further eliminate temperature and flux outliers from the surface observations. While conducting the calibration analysis we found biases in the body temperature of the two radiometers of roughly 2 K . Because a bias in the radiometer body temperature can lead to biases in the LW downward flux measured by the pyrgeometers we derive a calibration coefficient for the net body LW flux in $\text{W m}^{-2} \text{ mV}^{-1}$ and then apply a temperature bias correction to the CG4 temperature. After correcting the CG4 body temperature we obtain a root-mean-squared-error (*RMSE*) in the body temperature of less than 1%. Next we estimate the calibration coefficient as the slope of the best fit line between the raw voltage output from the CGR4 and CG4 pyrgeometers. We derive a time-series of the factory calibration coefficient from 2018 to 2023 by linearly interpolating the CGR4 calibration coefficients from 2018 and 2023. Similar to the procedure outlined in the pyrgeometer manual (“CG4 Pyrgeometer Instruction Manual”, 2001) we multiply the voltage output of the CG4 pyrgeometer by the linearly interpolated CGR4 calibration coefficient and calibration coefficient of the raw voltage output. Finally we add this value to the upward LW flux emitted by the CG4 body ($5.67 \times 10^{-8} * T_b^4$, where T_b is the body temperature of the pyrgeometer) to obtain the surface LW upward flux.

Global positioning system

Global positioning system (GPS) retrieved total precipitable water vapor q – the amount of condensed water vapor in a column of atmosphere – has been shown to provide reliable retrievals of q (Haase, Ge, Vedel, & Calais, 2003; Ware et al., 2000) where the uncertainty is roughly 10% for mean conditions at the field site (J. Wang, Zhang, Dai, Van Hove, & Van Baelen, 2007; Bevis et al., 1994). Furthermore several studies used GPS retrieved q to validate q retrieved from satellite remote sensors (Liu, Tang, Hu, Zhang, & Deng, 2017; Roman et al., 2016; Bedka, Knuteson, Revercomb, Tobin, & Turner, 2010). We also obtain retrievals of q from a GPS

mounted at the field site (“D”, Figure 3.2) from 2020–2022 at a temporal resolution of 1 hour. GPS retrieve q by measuring the time lag between emitted and sampled radio signals from nearby satellites which can be delayed due to the presence and amount of water vapor in the atmosphere (Haase et al., 2003). Raw GPS retrievals here are processed by Souminet.

Sun Photometer

The field site houses a CIMEL sun photometer that is part of the NASA Aerosol Robotic Network (AERONET). This sun photometer is a radiometric instrument that measures solar radiance at the following 8 wavelengths 340, 380, 440, 500, 675, 870, 940, and 1020 nm (Holben et al., 1998). From these radiances the aerosol optical depth τ at a specific wavelength can be retrieved. We use level 1.5 τ retrievals (Holben et al., 1998) because these data have been cloud-screened and thus can allow us to evaluate cloud-free conditions based on the availability of level 1.5 τ . Previously the CIMEL sun photometer at the field site misclassified dusty measurements as being cloudy which led to missing cloud-free AERONET τ during dust storms (A. Evan, Walkowiak, & Frouin, 2022). In this study we use corrected level 1.5 τ at 500 nm (A. Evan et al., 2022; Holben et al., 1998), fine-mode-fraction f , and 440-675 nm angstrom exponent AE from 2020 to 2022 (Holben et al., 1998). The retrieved AERONET τ has an absolute uncertainty of 0.01 ($\pm 5\%$, Table 3.1). We also obtain q and solar zenith angle θ from the AERONET sun photometer. The AERONET q retrievals have an uncertainty $\sim 10\%$ and are limited to daytime and clear-sky conditions.

Total Precipitable Water Correction

Here we compare AERONET and GPS retrieved q in order to identify biases in the AERONET retrieved q . We compare AERONET q to GPS retrieved q since GPS q has been used to validate AERONET and other retrieved q products (Liu et al., 2017; Roman et al., 2016; Bedka et al., 2010). We do not exclusively use GPS q in this study because the GPS retrievals are collected at a lower temporal resolution than that from AERONET. The linear relationship

between the GPS and AERONET retrieved q (blue, closed circles in Figure 3.3) for daytime and clear-sky conditions from 2020–2022 show a positive and statistically significant linear relationship (r -value = 0.99, p -value < 0.01). The slope of the best fit line is 1.14 cm/cm while the y -intercept is set to 0. The $RMSE$ between AERONET and GPS q is 19%. As such we apply a linear correction to AERONET q at the site based on this regression slope and use this corrected AERONET q in the analyses presented here.

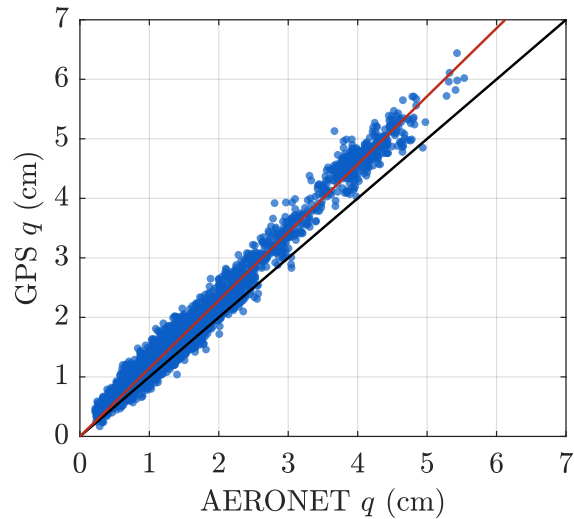


Figure 3.3: A scatter plot of the GPS (y-axis) and AERONET (x-axis) retrieved q (cm) before the correction was applied to the AERONET retrieved q . The black, solid line represents the 1:1 ratio of GPS and AERONET q while the red, solid line is the best-fit line between AERONET and GPS q .

Ceilometer

Also at the field site is a CL51 Vaisala ceilometer, a single lens lidar system that measures attenuated backscatter BS from the surface to 15 km. The ceilometer has a temporal and vertical resolution of 36 s and 10 m, respectively. The ceilometer was designed to detect the presence and height of clouds but has also been used to retrieve the vertical profile of aerosols in the lower atmosphere (Jin et al., 2015; Marcos et al., 2018; Munkel, Eresmaa, Räsänen, & Karppinen, 2007). More specifically the ceilometer can retrieve the extinction profile and optical depth at a nominal wavelength of 910 nm in the presence of dust (e.g. A. Evan et al., 2022). In this

study we obtain a time series of cloud base height, BS , and extinction profiles to more explicitly identify cloud and dust presence (A. T. Evan et al., 2022b). The extinction profiles are further scaled by AERONET retrieved τ and we use these extinction profiles to derive τ as a function of height.

Identifying Clouds

Even though we utilize cloud-screened AERONET retrievals we apply another cloud filter on the *in-situ* measurements. To accomplish this goal we obtain cloud base height from the CL51 ceilometer (Table 3.1) and define scenes as being cloud contaminated if the cloud base height is greater than 2 km. We choose a threshold of 2 km because dust over the field site does not typically extend beyond 2 km (A. Evan et al., 2022). We then classify AERONET measurements as being cloudy if at least one cloud is identified within 30 minutes of each measurement. We assume a 30 minute threshold because fractional horizontal cloud cover has been estimated within this time period from ceilometer retrievals (Wagner & Kleiss, 2016).

Meteorological Measurements

We obtain 13 vertical profiles of temperature $T(z)$, pressure $P(z)$, and mixing ratio $w(z)$ from Vaisala RS-41 radiosondes launched at the site within the spring months of 2020–2022 (A. T. Evan et al., 2022a) during clear-sky conditions (Table 3.1). Since atmospheric profiles from the radiosonde only extend to roughly 25 km, we use profiles of temperature T , pressure P , and water vapor mixing ratio w from the San Diego Airport (NKX, Department of Atmospheric Science (n.d.)) to obtain atmospheric vertical profiles beyond 25 km. We then use a standard mid-latitude summer atmospheric profile from Anderson, Clough, Kneizys, Chetwynd, and Shettle (1986) to extend these profiles from ~ 32 to 95 km.

Mounted at the field site is a Vantage Pro2 Davis Met Station. This met station provides real-time data of surface meteorological data, i.e. P , T , humidity, wind speed, and wind direction. Here we obtain surface T , P , and w that are logged at a 1 minute temporal resolution from

Table 3.1: *In-situ* (top) and space-borne (bottom) instrumentation with their corresponding measurements, retrievals, and uncertainties used in this study.

Instrument/Product	Measurement/Retrieval	Uncertainty
<i>in-situ</i>		
Sunphotometer (L1.5)	τ at $0.5 \mu\text{m}$	5%
	q	10%
	θ	
	f	
	AE at $0.44 - 0.67 \mu\text{m}$	
GPS	q	10%
CM21 Pyranometers	Surface SW upward and downward flux	2%
CG4 Pyrgeometer	Surface LW upward flux	6%
CGR4 Pyrgeometer	Surface LW downward flux	5%
CL51 Ceilometer	BS , cloud base height, and β_e	
Met Station	2 m T, P, w	
Vaisala Radiosonde	$T(z), P(z), w(z)$	
<i>space-borne</i>		
CERES SSF (L2)	TOA SW upward flux	2%
	TOA LW upward flux	1%
	θ	
	Clear-sky fraction	
	Broadband SW surface albedo α	
	Broadband LW surface emissivity ϵ	
(MODIS/VIIRS)	τ at $0.55 \mu\text{m}$	10%
(GEOS-5)	q	10%

2020–2022.

3.2.2 Satellite Data

In this study we obtain observations of TOA SW upward flux and outgoing longwave flux (OLR) and retrievals of broadband SW surface albedo α from the Clouds and Earth’s Radiant Energy System (CERES) Single Scanner Footprint (SSF) level 2 data product (Wielicki et al., 1996; Su et al., 2015a; Su, Corbett, Eitzen, & Liang, 2015b; NASA/LARC/SD/ASDC, 2014b, 2014e, 2014d, 2014c). CERES is a space-borne instrument that measures top of the atmosphere (TOA) radiance at the SW (0.2–5 μm), window (8–12 μm), and total (0.2–100 μm) spectral intervals at a spatial resolution of ~ 25 km (Su et al., 2015a). LW radiance is estimated by taking the difference between the total broadband and SW radiances. Instantaneous CERES SSF measurements are collected along-scan of the CERES footprint as it traverses the Earth’s surface. We collect CERES SSF level 2 data onboard the National Aeronautics and Space Administration’s (NASA) Aqua and Terra satellites (Edition 4a, Table 3.1). These satellites are sun synchronous and pass over the equator at roughly 1:30/13:30 (Aqua) and 10:30/22:30 (Terra) local time (Loeb et al., 2018; Parkinson, 2003). In addition to CERES SSF data from Terra and Aqua, we obtain CERES SSF level 2 data onboard NASA and the National Oceanic and Atmospheric (NOAA) Suomi National Polar-orbiting Partnership (NPP, Edition 2A) and NOAA-20 (Edition 1B) sun synchronous satellites. Suomi NPP and NOAA-20 cross over the Earth’s surface at about 1:30 and 13:30 local time. The TOA SW fluxes from CERES onboard Aqua, Terra, Suomi NPP, and NOAA-20 are quantified using the same Angular Distribution Models (ADMs), which convert observed radiances to fluxes (Su et al., 2015a).

The CERES SSF data products differ across platforms in that CERES SSF data onboard Aqua and Terra are collocated with cloud and aerosol properties from the Moderate Resolution Imaging Spectroradiometer (MODIS) while CERES data onboard Suomi NPP and NOAA-20 are collocated to cloud and aerosol products from the Visible Infrared Imaging Radiometer Suite (VIIRS) imager. MODIS and VIIRS are radiometers that measure radiance at multiple

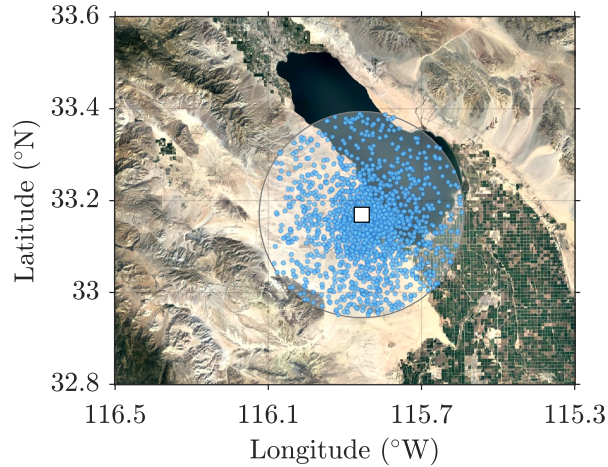


Figure 3.4: Nadir-looking points of the CERES SSF data used in this study. Shown are CERES SSF footprints (blue, closed circles) within approximately 25 km (shaded white circle) of the field site (white square). Shown are 1302 data points during clear-sky and daytime conditions.

wavelengths with the intent to observe various land, ocean, and atmospheric features on Earth. More specifically MODIS has 32 spectral bands within 0.4–14.5 μm at a spatial resolution of 1 km, 500 m, or 250 m (Parkinson, 2003) while VIIRS has 22 spectral bands from 0.402–12.488 μm and is part of a joint NASA and NOAA mission. Of the 22 bands, 18 bands have a nadir spatial resolution of 750 m and the other 4 bands have a nadir spatial resolution of 374 m (Xiong et al., 2014). These two radiometers were designed with similar features and capabilities with the goal to connect NASA’s EOS project and the joint NASA/NOAA mission. The aerosol retrieval algorithm from VIIRS is based off MODIS’ Dark Target retrieval algorithm. We obtain retrievals of MODIS deep blue τ at 550 nm and VIIRS corrected deep blue τ at 550 nm, both from the CERES SSF level 2 data products because these τ retrievals are more representative of τ over the total CERES footprint (Wielicki et al., 1996; Hsu et al., 2013). We assume that the differences between satellite and ground-based τ retrieved at 500 and 550 nm are small. We also obtain surface type and surface type fraction from the MODIS and VIIRS imagers to confirm the IGBP surface type classification and corresponding CERES broadband surface albedo within each CERES footprint (not shown).

We also use retrievals of q from the CERES SSF level 2 data product. This dataset is

derived from meteorological reanalysis products from the Goddard Earth Observing System Model version 5.4.1 (GEOS-5) in the Global Modeling and the Assimilation Office (GMAO) reanalysis product (Wielicki et al., 1996).

To filter for daytime and clear-sky conditions we obtain solar zenith angle θ and clear-sky fraction from the CERES SSF level 2 data product from 2019–2022 (Wielicki et al., 1996; NASA/LARC/SD/ASDC, 2014b, 2014e, 2014d, 2014c). We obtain clear-sky fraction from the clear/layer/overlap condition percent coverage parameter (Wielicki et al., 1996) and omit data where the clear-sky fraction is less than 95%; we choose this clear-sky fraction threshold in order to maintain a reasonable sample size for the TOA analysis while also limiting the amount of cloud-contamination. After filtering for clear-sky and daytime conditions we estimate the minute-averaged values for each CERES SSF parameter described above. To obtain CERES data representative of the conditions over the field site we limit the CERES SSF level 2 to measurements 25 km from the field site (white square, Figure 3.4).

3.2.3 Other Data Sets

We also obtain $T(z)$ and geopotential height from the Japan Meteorological Agency (JMA) and research data archive at the National Center for Atmospheric Research (NCAR, Computational and Information Systems Laboratory). Here we obtain JRA-55, daily 6-hourly model resolution model level at a 0.5616° spatial resolution (Japan Meteorological Agency, Japan, 2013). We also obtain concentrations of particulate matter (PM_{10}) from four stations around the field site (colored, closed circles in Figure 3.1b). These measurements are averaged over 1 hour. We also obtain images from a 360° Roundshot web camera maintained by the Imperial Irrigation District (IID). This roundshot camera lies at an elevation of roughly 300 m and is approximately 28 km west of the field site (white cross in Figure 3.1b). Roundshot images are available either at 12:00 local time or at 10 minute intervals during daytime hours. These images remain unavailable during the summer months (i.e. July, August, and September).

3.2.4 Identifying Dust Events

Because dust is not the only species of aerosols in the area we develop a method to identify dusty scenes. To do so we examine backscatter (*BS*) profiles retrieved by the CL51 Vaisala ceilometer (i.e. Figure 3.5a) and surface measurements such as *AE* (440–675 nm), *f*, τ , and PM_{10} (Figures 3.5b–e). We first select days and times as potentially being dust when *BS* is greater than 3 a.u.. Next we further select days and times when *f* is less than or equal to 0.5 (A. Evan et al., 2022) and *AE* is less than or equal to 1 (Voss & Evan, 2020). In order to ensure that dust is being considered we generally select times when PM_{10} is greater than or equal to $50 \mu\text{g m}^{-3}$ (Hoffmann, Funk, Wieland, Li, & Sommer, 2008) and τ is greater than 0.1 (A. Evan et al., 2022). When available, we verify the presence of dust or biomass burning using roundshot (i.e. Figure 3.6) and satellite imagery (i.e. Figure 3.7).

Shown in Figure 3.5 is an example of the time series of *BS*, PM_{10} , *f*, τ , and *AE* during a dust storm on April 22, 2022. The *BS* profile (Figure 3.5a) shows potential sporadic dust emission from 0:00–4:00 PT, 6:00–11:00 PT and 13:00–19:00 PT. In the corresponding time series for *f*, *AE*, τ , and PM_{10} (Figures 3.5b–e) we find that *f* is less than 0.5 from roughly 8:30–19:00 PT and *AE* is less than 1 for most of the day with the exception from roughly 7:30–8:30 PT. Also from roughly 8:30–18:30 PT τ is greater than 0.1. Values of PM_{10} from several stations surrounding the field site (Figure 3.1e) are greater than $50 \mu\text{g m}^{-3}$ from 0:00–4:00 PT, 7:00–11:30 PT, and 12:00–18:00 PT. These values evince the presence of large aerosol particles at these times. In consideration of the values of PM_{10} , τ , *f*, and *AE* from 440–675 nm throughout the day, we identify dust on April 22, 2022 from roughly 0:00–4:00 PT, 9:00–11:00 PT, and 13:00–19:00 PT. Dust storms identified at nighttime are based on PM_{10} values.

The roundshot (Figure 3.6) and visible satellite imagery (Figure 3.7) further support the dust identification based on the *BS* profiles and surface measurements (Fig 3.5). For example the roundshot imagery shows dust emission at 6:10, 8:00, and 16:00 PT (Figure 3.6). The visible satellite imagery show moderate dust emission while Aqua is overhead (roughly 13:30 PT) and

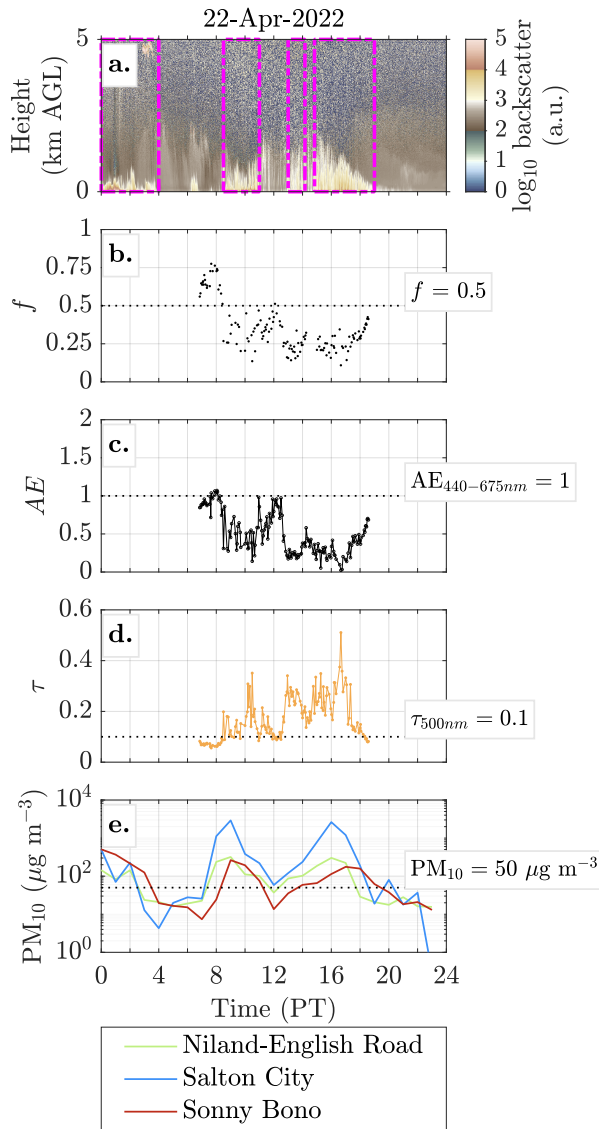


Figure 3.5: Shown is a time series of the (a) backscatter BS profile generated from the CL51 Vaisala ceilometer at the SIO field site during a dust storm on April 22, 2022. Times enclosed by the magenta dashed rectangles are identified as being dusty. Also shown are time series of (b) f (c) AE , (d) τ , and (e) PM_{10} concentrations on April 22, 2022. The blue, red, and green lines represent the PM_{10} concentrations from Salton City, Sonny Bono, and Niland-English Road, respectively.

no significant wildfires in the surrounding area (Figure 3.7).

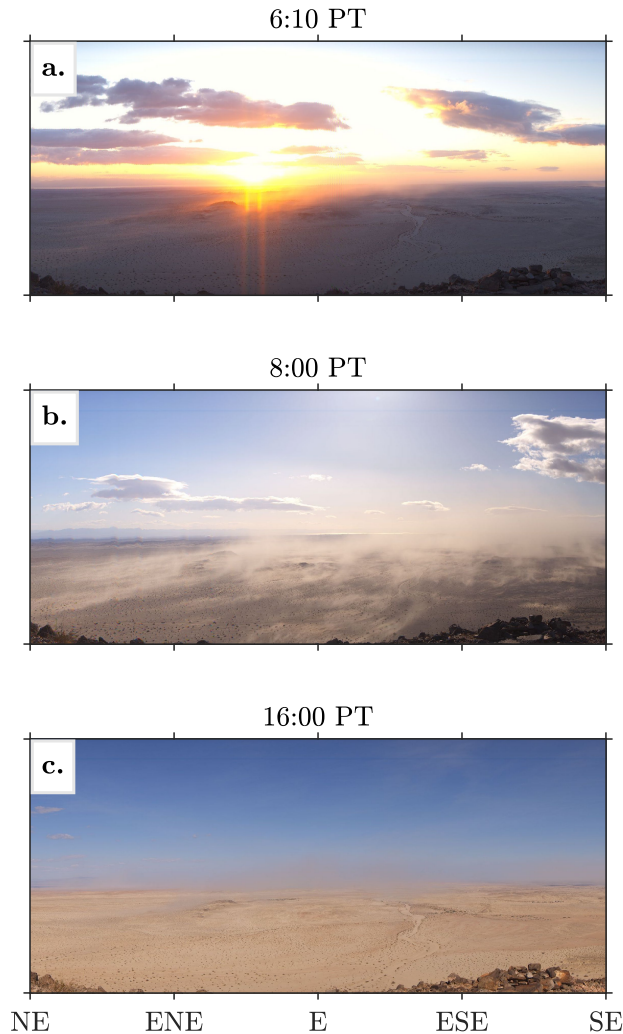


Figure 3.6: Roundshot images at (a) 6:10 PT, (b) 8:00 PT, and (c) 16:00 PT on April 22, 2022. Roundshot images are from a camera owned by the Imperial Irrigation District (IID) at the Anza-Borrego Station (accessed at: <https://iid.roundshot.com/anza-borrego/#/>), depicted as the white cross in Figure 3.1b.

3.2.5 Surface Soil Mineralogy

In order to calculate the complex refractive index *CRI* of dust over the field site we estimate the average soil mineralogy over the dust emitting regions that are typically upwind (i.e., to the west) of the field site (purple polygon in Figure 3.1), which are based on analysis of satellite imagery of dust outbreaks and eye-witness accounts. Surface soil mineralogy is from The Airborne Visible/Infrared Imaging Spectrometer - Classic (AVIRIS-C), a passive

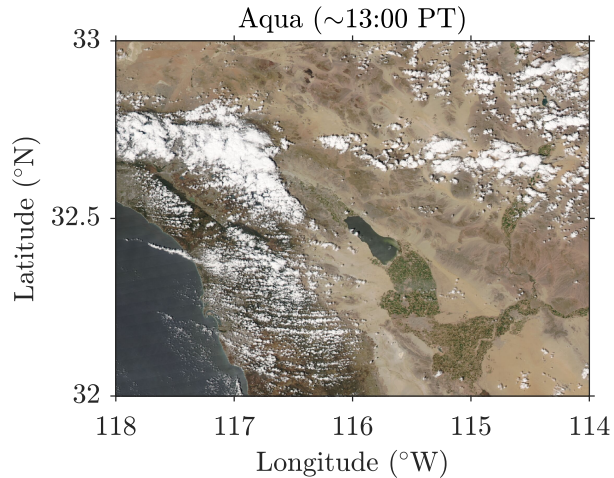


Figure 3.7: NASA Worldview True Color imagery on April 22, 2022 from Aqua (~13:30 PT). World view images can be accessed at: <https://worldview.earthdata.nasa.gov/>.

imaging spectrometer that operates in the 0.41-2.45 μm wavelength range and is designed to operate aboard NASA’s Earth Resources 2 aircraft (Chrien, Green, & Eastwood, 1990). The AVIRIS-C measurements used here were collected over the region in 2018 and from these data the approximate mineral abundance for the following nine minerals are retrieved: calcite, chlorite, dolomite, goethite, gypsum, hematite, illite, kaolinite, montmorillonite (Thompson et al., 2020). Also retrieved from AVIRIS-C are estimates of the fractional cover of major land surface types, of which fractional bare soil cover is used here.

3.3 Radiative Transfer Model

In this study we utilize the Rapid Radiative Transfer Model (RRTM) in the SW (version 2.5, Atmospheric & Environmental Research, 2004) and LW (version 3.3, Atmospheric & Environmental Research, 2010) from the Atmospheric and Environmental Research (AER) Inc (E. J. Mlawer, Taubman, Brown, Iacono, & Clough, 1997; E. Mlawer & Clough, 1997, 1998). This RRTM is a band transmission model that evaluates radiative transfer at 14 spectral bands ranging from 0.2–12.2 μm and 16 spectral bands from 3.1–1000 μm (Iacono et al., 2008; Clough et al., 2005). RRTM uses the correlated- k method to evaluate radiative transfer. In the SW code

the correlated- k method is applied to the solar source function, which derives the incoming solar flux at the TOA (E. Mlawer & Clough, 1998). We use 8 streams in the Discrete Ordinate Radiative Transfer (DISORT) to solve radiative transfer for multiple scattering in both the SW and LW spectrum (Iacono et al., 2008). Each SW band uses a present-day solar source function and a constant surface SW albedo α over each band. Correspondingly each LW band uses a constant broadband LW α of 0.0145. We assume a CO₂ mixing ratio of 417 ppm, which is the approximate average atmospheric CO₂ concentration measured at Mauna Loa in mid to late 2021. Other gases that are included in the model are water vapor, nitrogen, ozone, nitrous oxide, methane, oxygen, carbon monoxide, and the halocarbons CCL₄, CFC112, CFC12, and CFC222. We obtain SW α from the ratio of surface SW upwelling and downwelling flux measured from the CM21 pyranometers (Table 3.1) and the broadband LW α as 1 minus the temporally averaged surface LW emissivity ε from the CERES SSF data product. The model assumes Lambertian reflection at the surface. RRTM SW has been extensively validated against the Line-by-line Radiative Transfer Model (LBLRTM), an accurate line-by-line model that is continuously validated against observations; the coefficients used in the correlated- k method are developed via LBLRTM. RRTM SW is in agreement within 1.5 W m⁻² to LBLRTM (Clough et al., 2005).

We define 107 radiative levels for which radiative transfer RT is evaluated in RRTM SW and LW. We obtain vertical profiles of water vapor (relative humidity RH and mixing ratio w), T , and P as input into RRTM from several radiosonde launches at the field site during the spring months (i.e. February, March, April, and May) of 2020–2022 (Tables 3.1 and S3.2). Here we define the TOA and surface at 95 and 0 km above ground level (AGL), respectively. For radiosondes launched without a mounted pressure sensor we obtain surface P and estimate $P(z)$ via the hydrostatic equation. We also obtain vertical profiles of atmospheric temperature and geopotential height from reanalysis.

Dust Complex Refractive Index

For the RRTM simulations we estimate the dust complex refractive index (*CRI*) using the surface soil mineralogy described in Section 3.2.5 and the methods described in Walkowiak (2022). Briefly, we firstly average the mineral abundances over the polygon shown in Figure 3.1, weighing each 20 m horizontal resolution AVIRIS-C grid cell by its corresponding bare soil fraction. The retrieved AVIRIS-C soil mineralogy is 7% calcite, 3% kaolinite, 2% goethite, 2% montmorillonite, 0.5% hematite and illite, and with the abundances of chlorite, dolomite, and gypsum being < 0.1% (Figure 3.8).

In order to generate a *CRI* from the AVIRIS-C surface soil mineralogy we partition the surface mineralogy into clay and silt sizes. To do so we assume that the fractional surface soil abundance of a mineral m , given by AVIRIS-C, is

$$m = f_c m_c + f_s m_s \quad (3.1)$$

where m_c and m_s are the soil mineral abundances in the clay and silt sizes, respectively, and f_c and f_s are the fractional abundances of clay and silt in the soil, respectively, which are calculated from the soil probability size distribution in Kok (2011). We also define the ratio of mineral abundance r_m in the clay and silt size ranges as $r_m = m_c/m_s$, which allows us to express m_s and m_c , via Eq. 3.1, as

$$m_s = \frac{m}{f_c r_m + f_s} \quad (3.2)$$

and

$$m_c = \frac{m - m_s f_s}{f_c} \quad (3.3)$$

We obtain r_m for each AVIRIS-C mineral from the clay and silt fractional abundances for the Calcaric Fluvisols soil type in Claquin, Schulz, and Balkanski (1999) and then estimate the

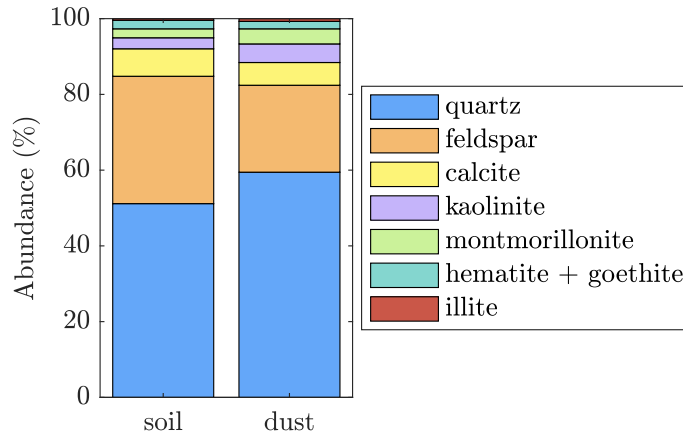


Figure 3.8: Mineral abundances of the surface soil and dust, based on AVIRIS-C retrieved mineral abundance averaged over the polygon in Figure 3.1.

fractional contribution of each to the soil clay and silt sizes via Eqs. 3.2 and 3.3. We assume that the unclassified abundances in the clay and silt sizes are comprised of quartz and feldspar, two abundant minerals that are not retrieved by AVIRIS-C due to their relatively uniform optical properties across the solar spectrum. We proportionally assign the quartz and feldspar fractions within each soil size class via their relative abundances for the same soil type (Claquin et al., 1999). For this case the total soil abundances of quartz and feldspar are 51% and 34%, respectively (Figure 3.8). We obtained similar results when repeating this process but using the Luvic Yermosols soil type abundances from Claquin et al. (1999) and using the reported abundances for these two soil types via Journet et al. (2014, not shown).

Having partitioned the AVIRIS-C soil mineralogy into the silt and clay sizes, we follow the methods described in Scanza et al. (2015) in order to generate a corresponding dust mineralogy, which slightly differs to that for the surface soil since minerals in the clay sizes are more abundant in the aerosol than in the surface (Figure 3.8). We also follow the methods of Scanza et al. (2015) to estimate a resulting *CRI* from the dust mineralogy. Here in the solar part of the spectrum we obtain the characteristically flat real part of the refractive index n (Figure 3.9a) while the imaginary part of the refractive index k increases with decreasing wavelength (Figure 3.9b). This pattern is due to the abundance of the iron oxides hematite and goethite

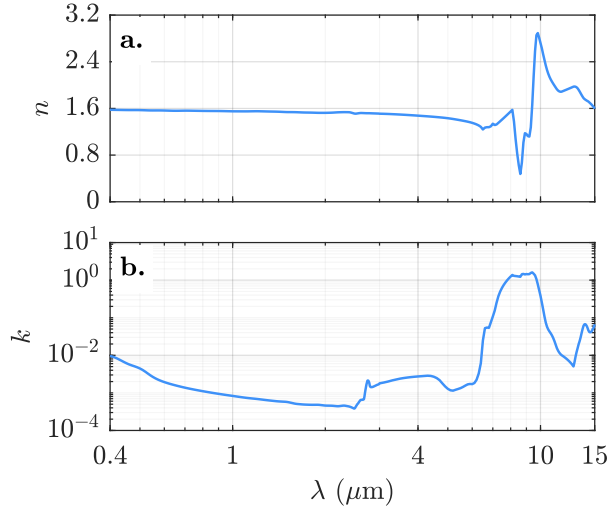


Figure 3.9: Shown are plots of the (a) real n and (b) imaginary k parts of the dust CRI calculated from the AVIRIS-C surface soil mineralogy over the 0.4–15 μm spectral range.

(Figure 3.8). In the LW part of the spectrum the peak in k in the 8–10 μm range is due to strong absorption features in quartz, feldspar, kaolinite, and montmorillonite, and these same minerals also contribute towards the trough and peak in n at approximately 8.5 and 10 μm , respectively.

We note that we obtained a qualitatively similar CRI when using a dust size distribution that includes more coarse dust particles (Meng et al., 2022), and when substituting the Maxwell–Garnett mixing method with the Bruggeman or volume mixing methods (Chylek, Srivastava, Pinnick, & Wang, 1988; Bohren & Huffman, 2008).

Dust Single Scatter Properties

We obtain dust single scatter properties from the Texas A&M University dust 2020 (TAMUdust2020) version 1.1.0 database of optical properties of irregular aerosol particles (Saito, Yang, Ding, & Liu, 2021). This database generates single scatter properties of randomly-oriented and irregular-shaped dust particles given a CRI and degree of asphericity by considering ensembles of at least 20 irregular hexahedral particles. We use the dust CRI described in Section 3.3 and use the default model dust asphericity, which is consistent with the global mean dust particle aspect ratio reported in Huang et al. (2020).

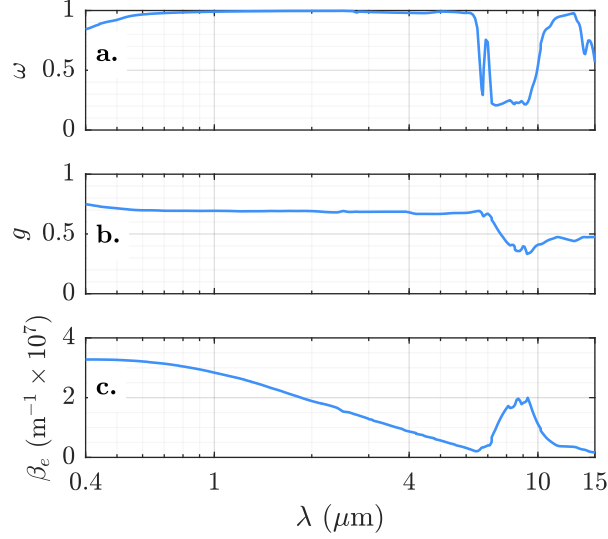


Figure 3.10: Dust single scatter properties used in RRTM and based on the *CRI* derived from AVIRIS-C (Figure 3.9). Plotted are the (a) single scatter albedo ω , (b) asymmetry parameter g , and (c) extinction coefficient β_e over the 0.4–15 μm spectral range.

We estimate the spectrally-resolved extinction coefficient $\beta_e(\lambda)$, single scatter albedo $\omega(\lambda)$, and asymmetry parameter $g(\lambda)$ from the model output and an estimate of emitted dust size distribution (Meng et al., 2022), using typical methods (e.g. Seinfeld & Pandis, 2016). For example, we apply the following equations at each height in the atmosphere

$$\beta_e(\lambda) = \int_{D_{min}}^{D_{max}} A(D) Q_e(\lambda, D) n(D) dD$$

$$\omega(\lambda) = \frac{\int_{D_{min}}^{D_{max}} A(D) Q_s(\lambda, D) n(D) dD}{\int_{D_{min}}^{D_{max}} A(D) Q_e(\lambda, D) n(D) dD}$$

$$g(\lambda) = \frac{\int_{D_{min}}^{D_{max}} A(D) Q_s(\lambda, D) g(\lambda, D) n(D) dD}{\int_{D_{min}}^{D_{max}} A(D) Q_e(\lambda, D) n(D) dD}$$

where Q_s is the dust volume scattering coefficient, A is the particle projected area, D is the dust particle diameter, g is the dust asymmetry parameter, Q_e is the volume extinction coefficient, and $n(D)$ is the size-resolved dust concentration with height. The resulting single scatter properties exhibit typical characteristics of dust (e.g. Highwood & Ryder, 2014) including increasing ω with increasing wavelength (Figure 3.10a) and scattering in the forward direction (Figure 3.10b),

both in the visible, and decreasing β_e with increasing wavelength except for a peak in the 8-10 μm spectral range (Figure 3.10c).

In order to obtain spectrally and height dependent τ we first derive the AE for each spectral band in RRTM SW and LW via linear least squares regression in log-log space of λ and $\beta_e(\lambda)$ generated from the TAMUdust2020 output. We use this band dependent AE to convert 500 nm AERONET τ to an average τ for each RRTM spectral band (Ångström, 1964; Gueymard, 2001; Ruiz-Arias, Dudhia, & Gueymard, 2014). In order to obtain height dependent τ we scale the spectral τ by the dust extinction coefficient β_e from the CL51 ceilometer (Table 3.1) and vertically integrate β_e for each 107 radiative levels in RRTM.

We note that running RRTM with height dependent $\omega(\lambda)$ and $g(\lambda)$ did not drastically change the results so we run RRTM while holding $\omega(\lambda)$ and $g(\lambda)$ constant with height to improve the efficiency and speed of running RRTM.

Radiative Transfer Model Uncertainty

Next we validate RRTM SW and LW output against surface observations in order to gauge the representation of dust in RRTM. To accomplish this goal we first run RRTM with $T(z)$, $P(z)$, and $RH(z)$ measured from 13 radiosondes launched at the field site during the spring months from 2020–2022 (Table S3.2) and dust $\beta_e(z)$ from the CL51 ceilometer (Table 3.1) averaged within the first 10 minutes of each sonde launch. We compare the surface SW fluxes to observations averaged within the first 10 minutes of each launch (Figure 3.11). We find that the modeled and observed surface SW net flux are nearly identical with the exception of a negative bias in the SW flux (-18 W m^{-2}) on March 9, 2021 at 19 UTC. The $RMSE$ for modeled surface net SW flux (9.6 W m^{-2}) is 2% of the average observed net SW flux (Figure 3.11). These results suggest that RRTM SW is accurately modeling dust and radiation given the precise local meteorological conditions and dust optical properties. Here we do not compare modeled and observed TOA SW fluxes due to unavailability of observed TOA SW fluxes during radiosonde launches.

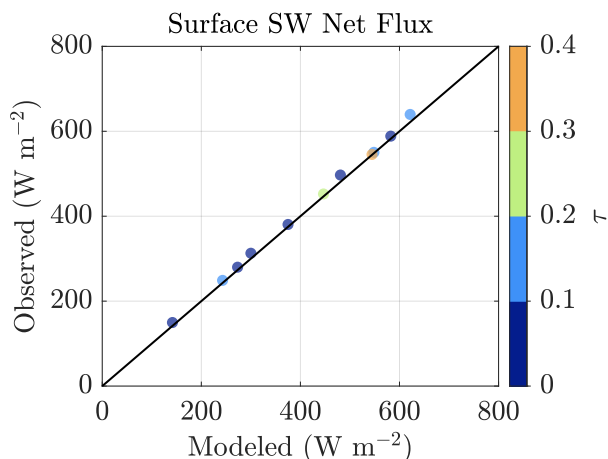


Figure 3.11: Shown is a scatter plot of the observed (y-axis) and modeled (x-axis) surface net SW flux. These simulations are run under clear-sky conditions with inputs obtained from 13 radiosonde launches during dust storms at the SIO field site from 2020–2022. The black line represents the 1:1 ratio and the colors denote the AERONET τ at 500 nm, averaged within the first 10 minutes of each launch. All observed fluxes are averaged within the first 10 minutes of each launch. The *RMSE* for the modeled surface SW net flux is 2%.

Next we compare observed and modeled surface net LW fluxes where observed LW fluxes are averaged within the first 10 minutes of each radiosonde launch (Figure 3.12). We find that there is an overall negative bias in the modeled surface net LW flux (mean bias = -5 W m^{-2}) and an *RMSE* of 6.1 W m^{-2} which is 4% of the mean net LW flux. This negative bias indicates that the magnitude of the surface net LW flux is overestimated by RRTM LW. Upon consideration of the upward and downward LW fluxes at the surface, much of the discrepancy is due to an underestimation of the magnitude of the LW downward flux (mean bias = -9 W m^{-2} , not shown) in the model. Biases in the modeled net LW flux are not significantly correlated to τ , q , and surface T and are not reduced if the vertical resolution of the radiative levels in RRTM is increased. It is unclear why there is a negative bias in the surface net LW flux, but we speculate that biases in the net LW flux may arise due to the representation of $T(z)$ at heights near the surface because we do not fully measure the small-scale variation of T with height between the Earth’s soil and overlying air. Despite finding discrepancy between the modeled and observed net LW fluxes, we find high positive and significant correlation between modeled and observed

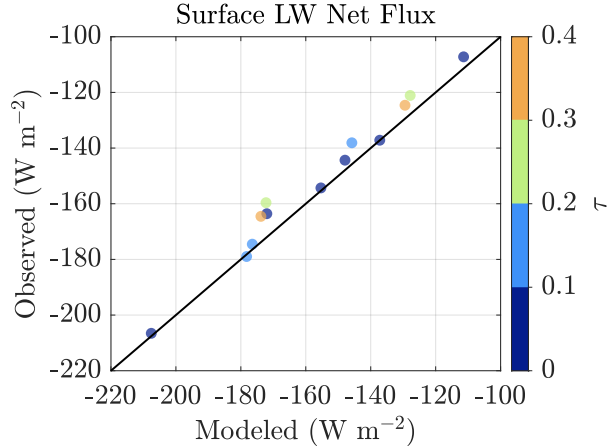


Figure 3.12: Shown is a scatter plot of the observed (y-axis) and modeled (x-axis) surface LW net flux. These simulations are run under clear-sky conditions with inputs obtained from 13 radiosonde launches during dust storms at the SIO field site from 2020–2022. The black line represents the 1:1 ratio and the colors denote the AERONET τ at 500 nm, averaged within the first 10 minutes of each launch. All observed fluxes are averaged within the first 10 minutes of each launch. The *RMSE* for the modeled surface LW net flux is 4%.

fluxes ($r = 0.99$, p -value < 0.01) and low relative *RMSE* (Figure 3.12). These results suggest that RRTM LW is reproducing the surface net LW fluxes somewhat realistically. Similar to the SW analysis here we do not compare the observed and modeled TOA LW fluxes.

Next we expand our model analysis by running RRTM SW and LW during days and times when there is an available AERONET level 1.5 τ retrieval. We run RRTM SW and LW with temporally, linearly interpolated vertical profiles of T and geopotential height from reanalysis, averaged P profiles scaled by collocated surface pressure, and an average w profile scaled by AERONET q (in kg m^{-2} , Table 3.1). We average dust $\beta_e(z)$ within the first 5 minutes of each AERONET measurement and scale $\beta_e(z)$ by the corresponding spectral τ for each simulation. Here we compare fluxes during times when the atmosphere is cloud free and dust laden. We find that the cloud-free and dust laden modeled and observed surface net SW fluxes are in agreement with an *RMSE* of 4% (mean bias = 3 W m^{-2} , Figure 3.13a). Additionally the observed and modeled surface net SW fluxes are positively correlated to one another ($r = 0.997$, p -value < 0.01). Because the SW α retrieved from the CERES SSF data product is more representative of the CERES footprint and not surface conditions at the field site, we correct for potential biases

in the observed TOA SW upward flux due to SW α by regressing out the linear contribution of the flux bias by SW α . We find that modeled and observed SW upward flux at the TOA are highly correlated to one another ($r = 0.8$, p -value < 0.01) and the $RMSE$ is 11% (mean bias = -1 W m^{-2} , Figure 3.13b). These results suggest that RRTM SW is realistically representing dust in its scheme and reasonably modeling the SW flux.

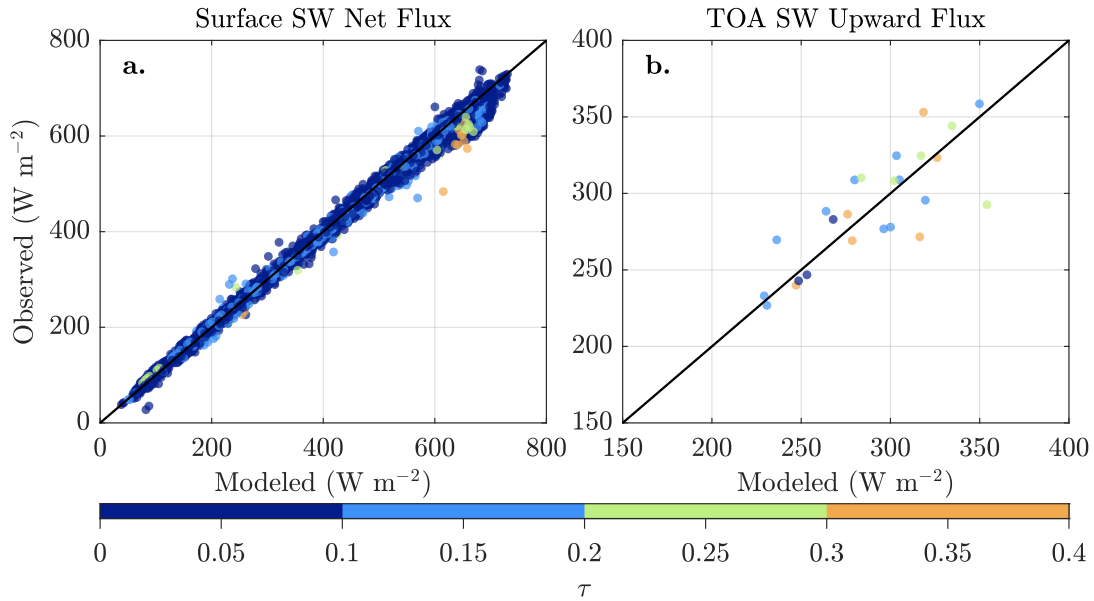


Figure 3.13: Shown are scatter plots of the observed (y-axis) and modeled (x-axis) SW flux at the (a) surface (net) and (b) TOA (upward). Each model run is simulated under clear-sky and dusty conditions, as described in Sections 3.2.1 and 3.2.4, respectively. The black line represents the 1:1 ratio and all radiometric measurements (1-minute averages) are temporally collocated to AERONET τ . The colors represent AERONET retrieved τ at 500 nm. The $RMSE$ for the modeled SW surface net and TOA upward fluxes are 4% and 11%, respectively.

We find positive and significant correlation between the cloud free and dust laden modeled surface net LW flux (r -value = 0.87, p -value < 0.01) and an $RMSE$ of 13% (mean bias = 4 W m^{-2} , Figure 3.14a). For a majority of observations and simulations RRTM LW tends to underestimate the magnitude of the surface net LW flux. Additionally we find that biases in the net surface LW fluxes (Figure 3.14a) are linearly dependent on soil surface T ($r = 0.48$, p -value < 0.01) and q ($r = 0.4$, p -value < 0.01). These results are contradictory to the results when simulating the LW flux for each radiosonde launch at the field site (Figure 3.12). These findings

suggest that underlying causes of the biases in the modeled LW fluxes are unclear since the sign of the mean bias is inconsistent when considering RRTM LW output during each radiosonde launch (Figure 3.12) and AERONET measurement (Figure 3.14a). It is also possible that model simulations corresponding to each AERONET measurement may include biases that were also present in the simulations corresponding to each radiosonde and biases associated with soil surface T and q . Similarly for the surface analysis the outgoing longwave radiation (OLR) at the TOA generated from RRTM LW is positively and significantly correlated to the observed OLR from the CERES SSF data product ($r = 0.88$, p -value < 0.01 , Figure 3.14b). There is a mean positive model bias of 16.6 W m^{-2} while the $RMSE$ is 6% of the average observed OLR. Because the underlying causes to clear-sky model LW flux bias may also be present in the pristine-sky simulations, we do not estimate the LW ζ of dust by subtracting the observed clear-sky LW fluxes by the modeled pristine-sky LW fluxes. Furthermore we do not apply corrections to the clear-sky and pristine-sky LW fluxes simulated by RRTM LW based on q and soil surface temperature because, at least for surface temperature, dust can alter desert surface temperatures (Yoshioka et al., 2007).

3.4 Methods

The clear-sky SW and LW direct radiative effect of dust at height z (ζ_z) is defined as the difference between the clear-sky (cloud-free) and pristine-sky (cloud and dust-free) net flux

$$\zeta_z = \left(F_z^\downarrow - F_z^\uparrow \right) - \left(F_z^\downarrow - F_z^\uparrow \right)_p \quad (3.4)$$

where F_z is the SW or LW flux at height z , the subscript p denotes the flux for pristine-sky conditions, the absence of a subscript represents clear-sky conditions, and the superscripts \downarrow and \uparrow describe the flux components in the downward and upward directions, respectively.

Since pristine-sky fluxes cannot be directly measured via observations, we define the clear-sky forcing efficiency η of dust at height z as the ζ_z normalized by the aerosol optical depth

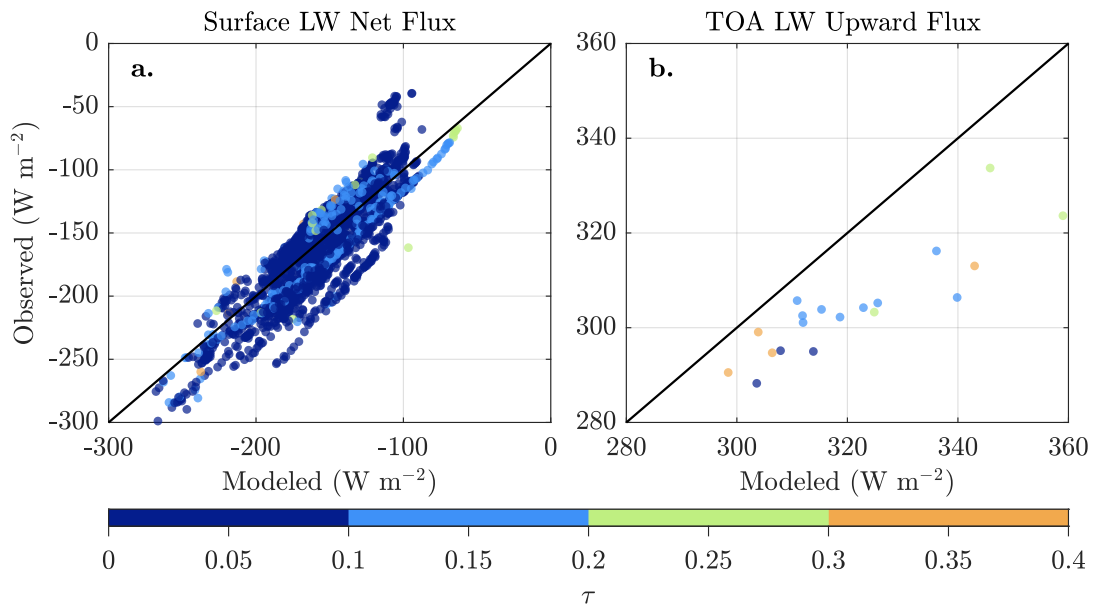


Figure 3.14: Shown are scatter plots of observed (y-axis) and modeled (x-axis) LW fluxes at the (a) surface (net) and (b) TOA (upward). All RRTM LW output are simulated under clear-sky and dusty conditions. The black line represents the 1:1 ratio and the colors represent AERONET retrieved τ at 500 nm. Observed and modeled LW fluxes are temporally collocated to AERONET measurements and retrievals. The *RMSE* for the modeled LW surface net and TOA upward fluxes are 13% and 6%, respectively.

τ . We can therefore relate the η and ζ via

$$\eta_z = \frac{\zeta_z}{\tau} \quad (3.5)$$

and if τ is linearly proportional to ζ_z

$$\eta_z = \frac{d\zeta_z}{d\tau} \quad (3.6)$$

where Eq. 3.5 can be estimated as the ratio of ζ_z and τ .

In the remainder of this section we describe the theory related to estimating the clear-sky dust SW η at height z with only observations (Section 3.4.1). Next we describe and justify using the observational method to estimate the SW ζ_z and η_z (Section 3.4.2). In Section 3.4.3 we describe how we use RRTM SW and LW to estimate both the dust SW and LW ζ_z and η_z .

3.4.1 Theory

The clear-sky SW forcing efficiency η of dust at the surface and top of the atmosphere (TOA) has been estimated solely from surface and TOA measurements over land (e.g. Satheesh & Ramanathan, 2000; Kuwano & Evan, 2022; Hsu et al., 2000; Di Biagio et al., 2009, 2010; Yang et al., 2009) and ocean (e.g. Hsu et al., 2000; Loeb & Kato, 2002; F. Li et al., 2004; Song et al., 2018). Here we apply the methods described in Kuwano and Evan (2022) to estimate the surface and TOA SW η of dust. We assume that during dusty conditions, the surface SW net flux S_0^n and TOA SW upward flux S_∞^\uparrow can be represented as linear function of τ , q , μ , and surface SW albedo α

$$S_0^n = \left(\frac{\partial S_0^n}{\partial \tau} \right)_{q,\mu,\alpha} \tau + \left(\frac{\partial S_0^n}{\partial q} \right)_{\tau,\mu,\alpha} q + \left(\frac{\partial S_0^n}{\partial \mu} \right)_{\tau,q,\alpha} \mu + \left(\frac{\partial S_0^n}{\partial \alpha} \right)_{\tau,q,\mu} \alpha + S_*^n \quad (3.7)$$

and

$$S_{\infty}^{\uparrow} = \left(\frac{\partial S_{\infty}^{\uparrow}}{\partial \tau} \right)_{q,\mu,\alpha} \tau + \left(\frac{\partial S_{\infty}^{\uparrow}}{\partial q} \right)_{\tau,\mu,\alpha} q + \left(\frac{\partial S_{\infty}^{\uparrow}}{\partial \mu} \right)_{\tau,q,\alpha} \mu + \left(\frac{\partial S_{\infty}^{\uparrow}}{\partial \alpha} \right)_{\tau,q,\mu} \alpha + S_{*}^{\uparrow} \quad (3.8)$$

respectively, where S represents the SW fluxes and the subscript $*$ describes the SW flux at a mean μ for a pristine, completely dry atmosphere and over a surface with a pristine-sky SW α . Subscripts $()_{\tau}$, $()_q$, $()_{\mu}$, and $()_{\alpha}$ represent partial derivatives while holding τ , q , μ , or α constant, respectively.

In consideration of the effects of q , τ , μ , and α on the clear-sky SW flux at the surface and TOA, Eq. 3.6 can be simplified to

$$\eta_0 = \left(\frac{\partial S_0^n}{\partial \tau} \right)_{q,\mu,\alpha} \quad (3.9)$$

and

$$\eta_{\infty} = - \left(\frac{\partial S_{\infty}^{\uparrow}}{\partial \tau} \right)_{q,\mu,\alpha} \quad (3.10)$$

at the surface and TOA, respectively.

3.4.2 Observational Method Description and Justification

In the observational method we use observations of SW fluxes and α and retrievals of τ , q , and μ to estimate the clear-sky instantaneous surface and TOA SW η of dust (Eq. 3.9 and 3.10, respectively) via multivariate regression of Eqs. 3.7 and 3.8, respectively. For the surface analysis we obtain observed surface net SW fluxes from the Kipp and Zonen pyranometers (Table 3.1) and retrievals of τ , q , and μ from AERONET (Table 3.1). Surface SW α is estimated as the ratio of the observed surface SW upward and downward fluxes. We filter these data for dust laden and clear-sky conditions as described in Sections 3.2.4 and 3.2.1, respectively.

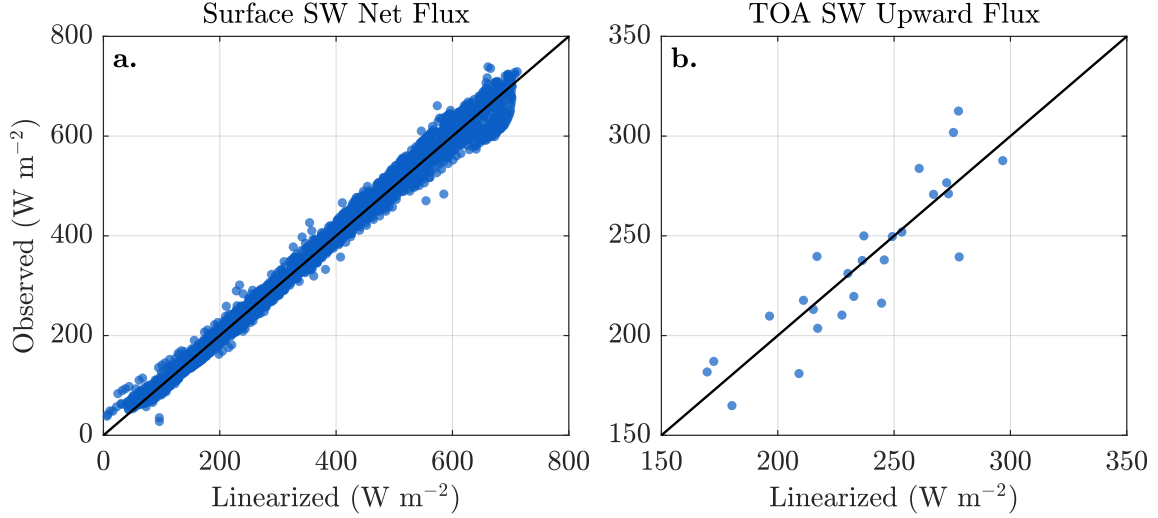


Figure 3.15: Shown are scatter plots of the observed (y-axis) and linearized (x-axis) SW flux at the (a) surface (net) and (b) TOA (upward). The black, solid-line represents the 1:1 ratio of the observed and linearized SW fluxes. All simulated and observed fluxes are collocated to AERONET measurements and retrievals during clear-sky and dusty conditions, as described in Sections 3.2.1 and 3.2.4, respectively. The *RMSE* of the surface SW surface net and TOA upward fluxes are 5% ($r = 0.995$, p -value < 0.01) and 7% ($r = 0.89$, p -value < 0.01), respectively.

If we represent the surface SW net flux as a linear function of τ , q , μ , and α (Eq. 3.7), we can use multivariate linear regression to estimate the regression coefficients (i.e. the slope of surface SW net flux to τ , q , μ , and α) and linearize the surface net SW flux. We find that there is significant, high positive correlation between the observed and linearized surface SW net flux (p -value < 0.01 , Figure 3.15a). The *RMSE* is 5% of the average observed SW net flux at the surface. These results suggest that non-linear effects on the surface SW net flux are second-order and thus it is reasonable to linearize the surface SW net flux via Eq. 3.7 and estimate the surface SW η of dust via the theory described in Section 3.4.1. Thus in the observation-based method we estimate the surface SW η of dust (Eq. 3.9) using multivariate regression of Eq. 3.7.

Similar to the surface analysis in the TOA analysis we obtain retrievals of τ , q , and μ from AERONET and measurements and retrievals of the TOA SW upward flux and broadband SW α from the CERES SSF data product. Even though MODIS τ is more representative of the CERES footprint, here we use AERONET τ because AERONET τ is more accurate than MODIS τ and

has been used as a reference to validate MODIS τ . We use q and μ from AERONET because AERONET q and μ do not greatly differ from q and μ from the CERES SSF data product (i.e. $r = 0.96$, p -value < 0.01 for AERONET and CERES SSF q). Similarly for the surface analysis we filter the satellite-based and *in-situ* measurements for dust-laden and clear-sky conditions via the methods described in Sections 3.2.4 and 3.2.1, respectively.

If we approximate the TOA SW upward flux as a linear function of τ , q , μ , and SW α (Eq. 3.8), we can use multivariate regression to estimate the regression coefficients and linearize the TOA SW upward flux. We find high positive and significant correlation between the observed and linearized SW upward flux at the TOA (Figure 3.15b). Furthermore the RMSE is 7% of the average SW upward flux at the TOA. Similarly for the surface analysis, these results suggest that at the TOA we can linearize the SW upward flux and estimate the TOA SW η using multivariate linear regression of Eq. 3.8.

3.4.3 Model Method Description

In the model method we use a Monte Carlo method to directly estimate the SW and LW ζ from Eq. 3.4 and η from Eq. 3.5 at the surface and TOA from model output for 10,000 simulations. In each simulation we add error to the surface and TOA SW and LW fluxes and τ . The error associated with the observed surface upward and downward fluxes are randomly sampled from a Gaussian distribution of mean 0 and standard deviation equal to the absolute error in the surface upward (2.1 W m^{-2} in the SW and 28 W m^{-2} in the LW) and downward fluxes (6.9 W m^{-2} in the SW and 16 W m^{-2} in the LW), respectively. The error associated with the observed TOA upward flux is randomly sampled from a Gaussian distribution of mean 0 and standard deviation equal to the absolute error in the CERES TOA fluxes over the field site (2.9 W m^{-2} in the SW and 3.1 W m^{-2} in the LW). For each simulation, the error in the modeled surface net and TOA upward fluxes are randomly sampled from a Gaussian distribution with a mean of 0 and standard deviation of the *RMSE* of the modeled fluxes, where instrumental uncertainty as described above is applied to the observed SW and LW fluxes.

In a similar manner error in τ is randomly sampled from a Gaussian distribution with mean 0 and standard deviation 0.01, the absolute error in AERONET τ for $\lambda > 440$ nm (Holben et al., 1998). The final SW and LW η estimates are equal to the average η over all Monte Carlo simulations; here we estimate both the 1 standard deviation σ uncertainty and 95% confidence interval ($\sim 2\text{-}\sigma$) over all simulations. We then estimate the SW and LW ζ as the product of η and the mean τ from 2020–2022 ($= 0.17$).

3.5 Results

Following the methods described in Section 3.4 in this section we use observations (Section 3.5.1) and model output from RRTM (Section 3.5.2) to estimate the instantaneous clear-sky forcing efficiency η of dust and the direct radiative effect ζ of dust in the SW and LW spectrums at the surface ($z = 0$), TOA ($z = \infty$), and atmosphere ($z = a$). We also use the output from RRTM SW and LW to derive the diurnally averaged clear-sky surface, TOA, and atmospheric SW and LW η and ζ of dust over the field site (Section 3.5.3).

3.5.1 Observation-based Shortwave Instantaneous Forcing Efficiency

As described in Section 3.4.2 we use both measurements of surface and TOA SW flux, τ , q , μ , and SW α to estimate the instantaneous SW forcing efficiency of dust at the surface η_0 and TOA η_∞ via Eqs. 3.9 and 3.10, respectively. Because the sample size, or the number of available measurements, of the satellite-based dataset is limited and we aim to more directly compare the clear-sky instantaneous SW η_0 and η_∞ , we estimate η_0 with surface measurements that are collocated to the CERES SSF level 2 data product (hereafter, the “collocated” *in-situ* dataset). However, estimating the SW η with a limited sample size may lead to large uncertainties in η and thus, we estimate the clear-sky instantaneous SW η_0 with an additional dataset which consists of all available *in-situ* measurements (hereafter, the “all” *in-situ* dataset).

The instantaneous SW η_0 estimated via the collocated and all *in-situ* datasets are -93 ± 41 and $-101 \pm 7 \text{ W m}^{-2}\tau^{-1}$, respectively (Figure 3.16). The uncertainty reported here is the

95% confidence interval of the regression coefficient. The relative uncertainties in the SW η_0 estimated with both datasets are under 45%, indicating that the sign of the instantaneous SW η_0 is constrained and dust induces a cooling effect at the surface over the Salton Basin. Because the instantaneous SW η_0 estimated via the collocated and all *in-situ* datasets are statistically similar we can define our best estimate of the instantaneous SW η_0 as $-101 \pm 7 \text{ W m}^{-2} \tau^{-1}$. Also note that the relative uncertainty in η_0 estimated with the all *in-situ* dataset is approximately less than 7% (Figure 3.16). It is likely that the main reason that the relative uncertainty in the SW η_0 estimated with the collocated *in-situ* dataset (44%) is much larger than that estimated with the all *in-situ* dataset is because the sample size of the all *in-situ* dataset is approximately 140% larger than the sample size of the collocated *in-situ* dataset.

Next we estimate the instantaneous SW η_∞ via multivariate linear least squares regression of Eq. 3.8 with observations of the TOA SW upward flux S_∞^\uparrow and retrievals of τ , q , μ , and SW α that are temporally collocated to the collocated *in-situ* dataset (hereafter, the “collocated” satellite dataset). We find that the instantaneous SW η_∞ estimated with the collocated satellite dataset is $-10 \pm 47 \text{ W m}^{-2} \tau^{-1}$ (Figure 3.16b). We also find statistically similar results if we estimate the instantaneous η_∞ with MODIS τ rather than AERONET τ (not shown). The relative uncertainty in the instantaneous SW η_∞ estimated from the collocated satellite dataset and AERONET τ is roughly 450% of the magnitude of the η_∞ . The primary reason for the relative η_∞ uncertainty exceeding 100% is the low satellite sample size (Figure 3.16b). The satellites from which we obtain CERES SSF data (i.e. Aqua, Terra, NOAA-20, and Suomi-NPP) are polar orbiting satellites that only measure data twice a day at a specific location. The sample size is further reduced when filtering for satellite data within 25 km from the field site (i.e. Figure 3.4), during daytime conditions ($\mu > 0$), during cloud-free scenes, and during dust storms. An additional factor contributing towards the high uncertainty in the instantaneous SW η_∞ is the bright desert surface (i.e. high SW α). For example Yang et al. (2009) used satellite observations and retrievals to determine the sensitivity of TOA SW upward fluxes and forcing on SW α ; they found that the SW η_∞ over the Sahara Desert becomes more negative or positive when the SW α

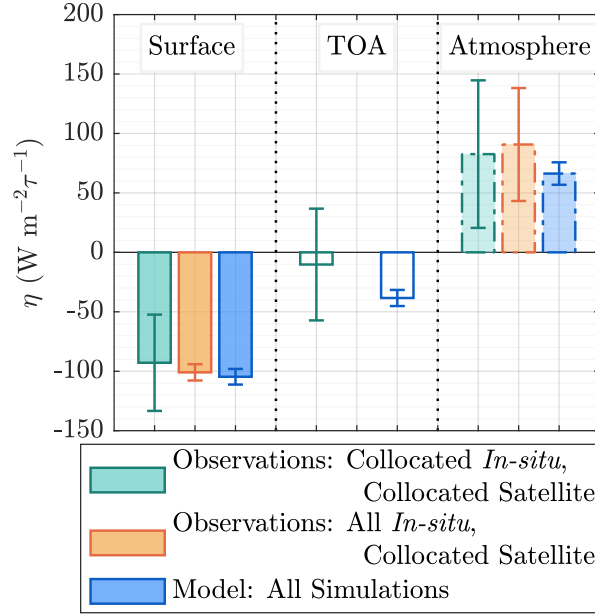


Figure 3.16: Observation (teal and orange) and model-based (blue) estimates of the clear-sky instantaneous SW η of dust at the surface (left), TOA (middle), and atmosphere (right). All observation-based estimates of SW η_∞ are estimated with the collocated satellite dataset (teal). For the surface, the teal bar represents the η_0 estimated with the collocated *in-situ* dataset while the orange bar denotes the η_0 estimated with the all *in-situ* dataset. For the atmosphere, the teal bar represents the η_a estimated with the collocated *in-situ* and satellite datasets while the orange bar represents the η_a estimated with the all *in-situ* and collocated satellite datasets. The purple bars represent the model-based estimates of the clear-sky instantaneous SW η of dust. All uncertainties are reported as the 95% confidence interval. Note that the sample size of the collocated *in-situ* and satellite datasets is 24 measurements while the sample size for the all *in-situ* dataset and simulations is 3421 measurements.

exceeds or falls below 0.32. Physically dust suspended over a bright surface can appear optically darker than the underlying surface and enhance solar warming. As a result the instantaneous SW η_∞ may approach 0 or become positive. It is also possible that over a bright surface the scatter between τ and the TOA SW upward flux can increase due to non-linear effects related to α becoming more significant. Because the sign of the instantaneous SW η_∞ is unconstrained it is unclear whether or not dust cools or warms at the TOA.

After estimating the clear-sky instantaneous SW η_0 and η_∞ of dust with observations we estimate the clear-sky instantaneous SW forcing efficiency of dust of the atmosphere η_a by taking the difference between best estimates of the instantaneous η_∞ and η_0 . The uncertainty

SPACE	a. Dust ζ (W m^{-2})		b. Dust η ($\text{W m}^{-2} \tau^{-1}$)	
	OBS Method	RTM Method	OBS Method	RTM Method
	-2 ± 8	-6 ± 1	-10 ± 47	-38 ± 7
ATMOSPHERE				
	15 ± 8	11 ± 2	91 ± 47	66 ± 9
SURFACE				
	-17 ± 1	-18 ± 1	-101 ± 7	-105 ± 7

Figure 3.17: Shown are the best estimates of the clear-sky instantaneous SW (a) ζ and (b) η of dust at the surface, TOA, and atmosphere. The abbreviations “OBS” and “RTM” represent the observational and model methods, respectively. All uncertainties are reported as the 95% confidence interval. The η_∞ estimated with the OBS method is estimated with the collocated satellite dataset while η_0 is estimated with the all *in-situ* dataset. The corresponding atmospheric η_a from the OBS method is estimated with η estimated with the all *in-situ* and collocated satellite datasets.

of η_a is estimated via error propagation. Using the collocated satellite and all *in-situ* datasets we estimate η_a as $91 \pm 47 \text{ W m}^{-2} \tau^{-1}$ (Figures 3.16 and 3.17b). We also estimate η_a using the collocated *in-situ* and satellite datasets as $83 \pm 62 \text{ W m}^{-2} \tau^{-1}$, which is statistically similar to the SW η_a estimated with the collocated satellite and all *in-situ* datasets. These results suggest that the sign of the instantaneous SW η_a is constrained and positive; however the magnitude of atmospheric warming is uncertain.

3.5.2 Modeled Instantaneous Forcing Efficiency

Shortwave

After validating RRTM SW we estimate the clear-sky instantaneous SW ζ (Eq. 3.4) and η of dust (Eq. 3.5) at the surface and TOA with modeled clear-sky and pristine-sky SW flux via the procedure described in Section 3.4.3. Here we estimate the instantaneous SW ζ and η with all RRTM output collocated to dust laden and clear-sky *in-situ* measurements (hereafter, all simulations). We find that the instantaneous SW η_0 of dust is $-105 \pm 7 \text{ W m}^{-2} \tau^{-1}$ (Figures 3.16 and 3.17b). The relative uncertainty in the model-based estimate of the instantaneous SW

η_0 is less than 10%. Furthermore we find that the model and observational-based estimates of the instantaneous SW η_0 are statistically similar (Figure 3.17b). These results suggest that the magnitude of the SW cooling effect by dust at the surface is roughly $|100| \text{ W m}^{-2} \tau^{-1}$.

Following the Monte Carlo approach in Section 3.4.3 we estimate the clear-sky instantaneous SW η_∞ and η_a with model output, where η_a is the difference between the model η_∞ and η_0 . We find that the model η_∞ and η_a are -38 ± 7 and $66 \pm 9 \text{ W m}^{-2} \tau^{-1}$, respectively (Figures 3.16 and 3.17b). We also find that the relative uncertainties in η_∞ and η_a are under 20%, indicating that the sign of η_∞ and η_a are constrained when using model output to estimate the instantaneous η_∞ and η_a . We find that the model η_∞ and η_z are statistically similar to the η_∞ and η_z estimated with only observations (Figures 3.16 and 3.17b). Consistency between the model and observation-based estimates of the instantaneous SW η_0 , η_∞ , and η_a suggest that we can use RRTM SW to derive the diurnal cycle of SW η (i.e. η as a function of μ) at the surface, TOA, and atmosphere and, given the relevant inputs, estimate diurnal averaged SW η at the surface, TOA, and atmosphere.

Longwave

After validating the RRTM LW output against observed surface and TOA LW fluxes we use the Monte Carlo method as described in Section 3.4.3 to estimate the LW forcing efficiency of dust at the surface η_0 and TOA η_∞ (Figure 3.18). We find that the clear-sky instantaneous LW η_0 and η_∞ are 22 ± 19 and $6 \pm 9 \text{ W m}^{-2} \tau^{-1}$, respectively. The atmospheric component η_a is estimated as the difference between the LW η_∞ and η_0 , which is $-15 \pm 21 \text{ W m}^{-2}$. A main feature of this plot is that the the relative uncertainties in LW η are greater than 100%, with the exception of η_0 ($\sim 85\%$), and thus the sign of the LW η is unconstrained at the TOA and atmosphere (Figure 3.18). One of the reasons that the relative uncertainty in the instantaneous LW η_0 is large is that the instrumental uncertainty in the pyrgeometer measurements and modeled fluxes is high. Relative errors in the observed LW upward (5%) and downward fluxes (6%) can translate into an *RMSE* of modeled LW net flux of $\sim 20\%$ and as a result, increases the spread of

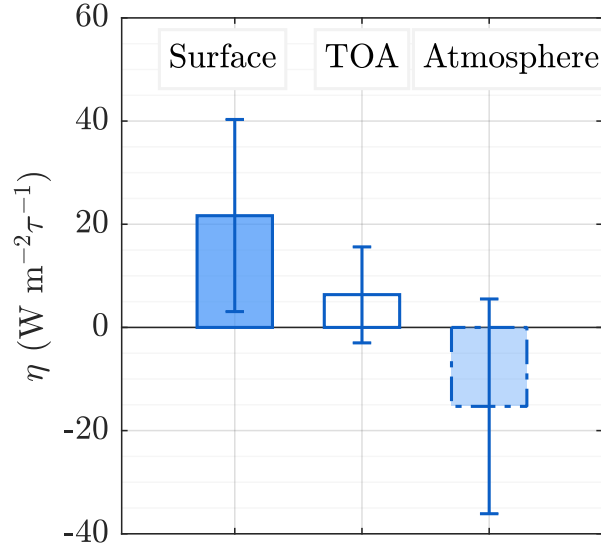


Figure 3.18: Shown are estimates of the clear-sky instantaneous LW η of dust at the surface (left), TOA (middle), and atmosphere (right) via the model method, described in Section 3.4.3. Error bars represent the 95% confidence interval of the instantaneous LW η .

the LW η in the Monte Carlo simulations. In regards to the TOA analysis it is possible that the uncertainty in the LW η_{∞} of dust is large due to possible high variation in the vertical distribution of temperature or water vapor.

3.5.3 Diurnally Averaged Forcing Efficiency

After validating model clear-sky and dust laden SW and LW fluxes against observations and finding consistency between the model and observation-based estimates of the instantaneous SW η , we estimate the clear-sky diurnally averaged SW and LW η of dust. We accomplish this goal by running RRTM SW and LW over a day with diurnal cycles of q and $P(z)$, $T(z)$, and $w(z)$. We estimate the diurnal cycle of q by applying a moving average filter on GPS retrieved q over μ intervals (bin width of 0.1) ranging from -1 to 3 , where $\mu < 0$ and $\mu > 2$ represent nighttime conditions and $0 < \mu < 1$ and $1 < \mu < 2$ represent morning and evening time periods, respectively. The diurnal cycle of $T(z)$ is obtained by applying the μ moving average to temperature at each height in the atmosphere. In regards to pressure and water vapor we scale an average pressure and mixing ratio profile by the diurnal cycle of surface pressure and GPS q (in

kg m⁻²). The diurnal cycle of the surface pressure is estimated via the same moving μ average applied on surface pressure from the met station (Table 3.1). We run RRTM SW and LW with a constant τ equal to the average daytime dust τ ($\bar{\tau} = 0.17$) and constant dust $\beta_e(z)$ equal to the average $\beta_e(z)$ over the 13 radiosonde launches and scaled by $\tau = 0.17$. We found that running RRTM SW with a constant τ and $\beta_e(z)$ profile did not drastically change the magnitude and sign of the diurnally averaged SW η of dust. Here we assume that the surface SW and LW albedos α are constant throughout the day and equal to the temporally averaged SW and LW α (0.3 and 0.0145, respectively). After running RRTM SW and LW with these inputs we obtain a look up table of the surface and TOA SW and LW fluxes as a function of μ .

In order to estimate the diurnally averaged η and the associated errors we modify the Monte Carlo approach (Section 3.4.3). For each simulation we quantify ζ directly from the model output (Eq. 3.4) and add uncertainty that is randomly sampled from a Gaussian distribution of mean 0 and standard deviation equal to the absolute error in the modeled ζ (1- σ uncertainty). The diurnal cycle of ζ is then derived by interpolating ζ by the diurnal cycle of μ for the solstices and equinoxes. We acquire the diurnal cycle of μ for the solstices and equinoxes of 2020 from the solarPosition MATLAB function (Mikofski, 2016). We consider the solstices and equinoxes because changes in seasonal solar insolation can alter the range of μ and the magnitude of η . The year 2020 is arbitrary and we assume that the diurnal variation of μ during the solstices and equinoxes do not significantly change on a yearly basis. We estimate an annually and diurnally averaged η by averaging the diurnally averaged η over all solstices and equinoxes.

Shown are the estimates of the clear-sky annual and diurnally averaged SW, LW, and net η of dust (Figure 3.19). The net η of dust was estimated as the sum of the SW and LW η and uncertainties are reported as the 95% confidence interval. We find that the annual and diurnally averaged SW, LW, and net η of dust at the surface are -44 ± 2 , 15 ± 10 , and -29 ± 10 W m⁻² τ^{-1} , respectively. The corresponding TOA components are -14 ± 2 , 4 ± 10 , and -10 ± 11 W m⁻² τ^{-1} in the SW, LW, and net, respectively, which result in a SW, LW, and net atmospheric η of 30 ± 3 , -11 ± 14 , and 19 ± 15 W m⁻² τ^{-1} , respectively (Figure 3.19). The relative uncertainty in the

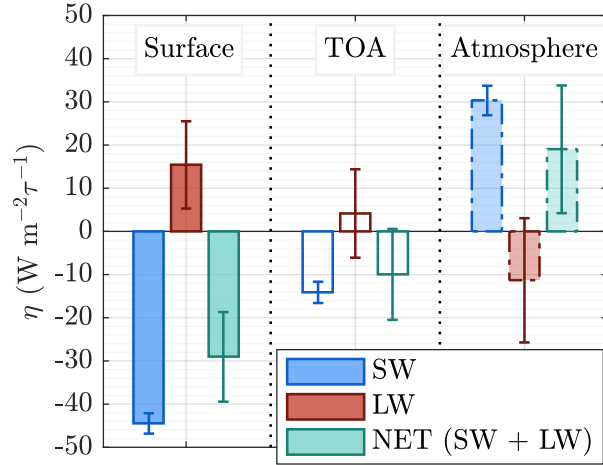


Figure 3.19: Shown is the clear-sky annual and diurnally averaged SW (blue), LW (red), and net (teal) η of dust at the surface (left), TOA (middle), and atmosphere (right). Error bars represent the 95% confidence interval of η .

annual and diurnally averaged net η of dust at the surface and atmosphere are 36% and 78%, respectively; these results suggest that the sign of the net η at the surface and atmosphere are constrained and that dust induces a net cooling and warming effect at the surface and atmosphere, respectively. Further study is required in order to constrain the sign of the TOA net η of dust and determine if dust cools or warms at the TOA.

3.5.4 Comparison to Other Studies

Instantaneous Comparisons

After estimating the instantaneous clear-sky SW and LW forcing efficiency at the surface η_0 , TOA η_∞ , and atmosphere η_a we compare our results to that from other studies. A map of the instantaneous SW η_0 (solid colored bar) and η_∞ (clear bar) estimated via the model method from this study, Di Biagio et al. (2010), Di Sarra, Fuà, and Meloni (2013), and Kuwano and Evan (2022) are presented in Figure 3.20. In order to better compare the results presented here to that from these other studies, we estimate the instantaneous η at μ equal to the mean μ for each solar zenith angle θ interval from these studies (Figure 3.20). Using observations and model output Di Biagio et al. (2010) estimated the instantaneous SW η_0 and η_∞ via the methods from

Satheesh and Ramanathan (2000) over Lampedusa (35.5°N, 12.6°E), a small island in the central Mediterranean that experiences frequent dust storms from the Sahara Desert. Over this same region, Di Sarra et al. (2013) used the output from an RTM to estimate the SW η_0 . In general our estimates of the instantaneous SW η_0 and η_∞ are more positive than the SW η_0 and η_∞ from Di Biagio et al. (2010) and Di Sarra et al. (2013). For example the instantaneous SW η_0 at $\bar{\mu} = 0.77$ estimated in this study ($-79 \pm 5 \text{ W m}^{-2}$) is roughly $|57| \text{ W m}^{-2} \tau^{-1}$ greater than the SW η_0 ($-136 \pm 12 \text{ W m}^{-2} \tau^{-1}$) at $\mu = 0.77$ from Di Biagio et al. (2010) (Figure 3.20). It is somewhat unclear as to whether or not this pattern arises due to differing optical properties of dust suspended over Lampedusa and the Salton Basin. For example, Di Biagio et al. (2010) identified that the single scatter albedo ω for desert dust in Lampedusa ranges from 0.76 ± 0.03 and 0.89 ± 0.05 for λ between 415 and 869 nm; over this spectral region the ω for dust over the Salton Basin ranges from 0.84 to 0.99. Di Sarra et al. (2013) also found that ω of dust suspended over Lampedusa ranged from 0.92 and ~ 0.99 . These findings are somewhat contradictory to one another, indicating that dust from Di Biagio et al. (2010) is more absorptive than dust from Di Sarra et al. (2013), despite these studies being conducted in the same study region. Furthermore it is possible that strongly absorbing aerosols can induce a strong cooling effect at the surface; yet aerosols that more efficiently scatter solar radiation can also induce a strong cooling effect at the surface. As such it is more likely that differences in the magnitude of the η_0 from this study and the studies conducted in Lampedusa (Di Biagio et al., 2010; Di Sarra et al., 2013) arise due to differing surface SW α or dust size. For example, surface SW α for Lampedusa was parameterized based on sea and land fraction within 5 km of the Station for Climate Observation in Lampedusa, which ranges from 0.06 to 0.21 (Di Biagio et al., 2010; Di Sarra et al., 2013). These low values of the SW α may explain the stronger cooling effect by dust at the TOA from Di Biagio et al. (2010) because the dust suspended over Lampedusa may be optically brighter than the underlying surface. Additionally Song et al. (2022) stated that dust found far from dust source regions may be smaller than freshly emitted dust. In order to make such a claim, however, one must consider both the measured dust size distributions in Lampedusa

and the Salton Basin. Despite finding statistically dissimilar results of the surface and TOA SW η of dust from this study and Di Biagio et al. (2010) and Di Sarra et al. (2013), the atmospheric SW η of dust found from this study and Di Biagio et al. (2010) are statistically similar at $\mu = 0.87$ and 0.77 (Figure 3.20), indicating a consensus that dust warms the atmosphere over Lampedusa and the Salton Basin.

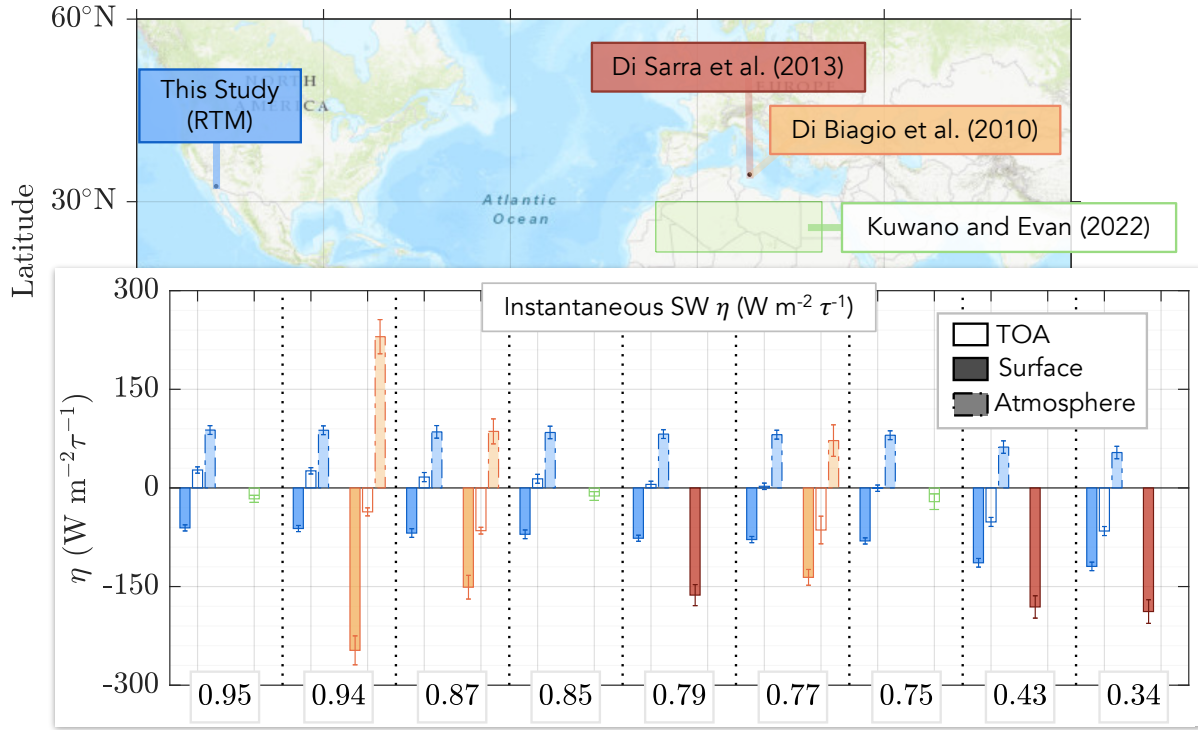


Figure 3.20: Shown are estimates of the clear-sky instantaneous SW η of dust at the surface (solid colored bar, solid line), TOA (clear bar, solid line), and atmosphere (solid colored bar, dashed-dot line) from this study (blue), Di Biagio et al. (2010) (orange), Di Sarra et al. (2013) (red), and Kuвано and Evan (2022) (green). Estimates of the instantaneous SW η of dust from this study are derived from RRTM SW output corresponding to μ intervals from Di Biagio et al. (2010), Di Sarra et al. (2013), and Kuвано and Evan (2022). Uncertainties from this study are the 95% confidence intervals.

We next compare the estimates of the instantaneous SW η_{∞} at μ of 0.95, 0.85, and 0.75 from Kuвано and Evan (2022) and this study (Figure 3.20). At these μ intervals the instantaneous SW η_{∞} estimated in this study are more positive than that from Kuвано and Evan (2022), which are equal to -16.6 ± 5.35 ($\mu = 0.95$), -12.3 ± 6.68 ($\mu = 0.85$), and -20.9 ± 11.9

($\mu = 0.75$) $\text{W m}^{-2} \tau^{-1}$ at μ of 0.95, 0.85, and 0.75, respectively (clear, green lined bars in Figure 3.20). Furthermore the instantaneous SW η_∞ from this study and Kuwano and Evan (2022) are statistically dissimilar. These results suggest that dust suspended over the Salton Basin may be more absorptive than dust suspended over the Sahara Desert. A comparison between the optical properties of dust suspended over the Sahara Desert and Salton Basin, however, is not straightforward to conduct. Measurements of Saharan dust ω at 550 nm from the Fennec (Ryder et al., 2013) and Sahara Dust Experiment (SHADE, J. Haywood et al., 2003) campaigns show that a majority of ω at 550 nm range from 0.95–0.98, while the corresponding ω for dust suspended over the Salton Basin (purple polygon, Figure 3.1) is approximately 0.95. Yet measurements from the Fennec campaign were measured with instruments that restrict the presence of larger dust particles, of which reach supermicron ($> 20\mu\text{m}$) values during the Fennec campaign and can reduce the magnitude of the ω at 550 nm (i.e. Ryder et al., 2013). A comparison between Saharan and Salton Basin dust ω at 450 nm suggests that dust suspended over the Salton Basin ($\omega = 0.89$) more efficiently absorbs blue light than does Saharan dust ($0.94 \leq \omega \leq 0.99$). Differences in the sign of the SW η_∞ from this study and Kuwano and Evan (2022) are unlikely due to differing surface albedo α . A majority of grid-boxes within the Sahara Desert (19 – 30°N, 10°W–30°E) have a SW α of roughly 0.35 while 67% of α over the field site ranges from 0.28 and 0.33 from 2020–2022. This comparison suggests that dust over the Salton Basin, in general, is more absorptive in the SW spectrum than dust over the Sahara Desert, which confirms the comparison between instantaneous SW η_∞ from this study and Kuwano and Evan (2022). In order to investigate these differences further, comparisons between measurements of the full size distribution of dust and, likely, the asphericity of dust suspended over the Sahara Desert and the Salton Basin are required.

Next we compare our estimates of the instantaneous surface and TOA LW η of dust to that from other studies (Figure 3.21). Hansell et al. (2012) used observations and retrievals to constrain an RTM to estimate the instantaneous LW ζ_0 and ζ_∞ over Zhangye, China during an intense 2 week dust storm. The instantaneous LW ζ_0 and ζ_∞ estimated from Hansell et al. (2012)

averaged over the study period ($\eta_0 = 10.1 \pm 4.9$ and $\eta_\infty = 5.2 \pm 3.7 \text{ W m}^{-2}$) are within the 1- σ uncertainties from this study ($\zeta_0 = 4 \pm 2$ and $\zeta_\infty = 1 \pm 2 \text{ W m}^{-2}$, Figure 3.21). However since ζ is dependent on τ we compare our estimates of the LW η_0 ($22 \pm 10 \text{ W m}^{-2}$) and η_∞ ($6 \pm 10 \text{ W m}^{-2}$) to the average instantaneous ζ divided by the daytime-averaged τ for the study time period ($\bar{\tau} = 0.53$, Hansell et al. (2012)). The regionally averaged instantaneous LW η_0 and η_∞ become 19 ± 9 and $10 \pm 7 \text{ W m}^{-2} \tau^{-1}$, respectively. Though our results are statistically similar to that from Hansell et al. (2012) we note that it is possible that there is agreement between this study and Hansell et al. (2012) due to differing dust optical properties over the Salton Basin and Zhangye; for example the dust ω ($1 < \lambda < 40 \mu\text{m}$) from Zhangye ranges from roughly 0.7 to 0.3 while ω ($10 < \lambda < 15 \mu\text{m}$) for dust over the Salton Basin approaches 1 (Figure 3.10). This comparison suggests that dust from Zhangye may be more absorbing than dust over the Salton Basin. Furthermore Hansell et al. (2012) incorporated smaller dust particles in their RTM model (i.e. dust diameter $< 10\mu\text{m}$) whereas in this study we utilize a dust size distribution that incorporates larger dust particles (i.e. $> 10\mu\text{m}$). Smaller dust particles are typically less effective at absorbing LW radiation (Song et al., 2022). Due to these competing optical and physical dust properties, it is unclear whether or not dust over Zhangye better absorbs or scatters LW radiation than does dust over the Salton Basin. These comparisons, however, suggest that the top of the dust layers over Zhangye and the Salton Basin may be the same height since the instantaneous LW η_∞ from this study and Hansell et al. (2012) are statistically similar.

The LW η_∞ from this study and that from Song et al. (2022) and Zhang and Christopher (2003) are statistically similar (Figure 3.21). For example, Song et al. (2022) used observations and retrievals to derive a clear-sky dust η dataset based on the spatial distribution of dust size and estimated the LW η_∞ over North Africa (S22a, Figure 3.21) as $12.8 \text{ W m}^{-2} \tau^{-1}$, which is within the 1- σ LW η_∞ uncertainty from this study. Furthermore, our estimates of the LW η_∞ are statistically similar to that from Brindley and Russell (2009) over Agoufou (BR09a), Banizoumbou (BR09b), DMN Maine Soroa (BR09c), IER Cinzana (BR09d), Saada (BR09e), and Solar Village (BR09g) stations (Figure 3.21).

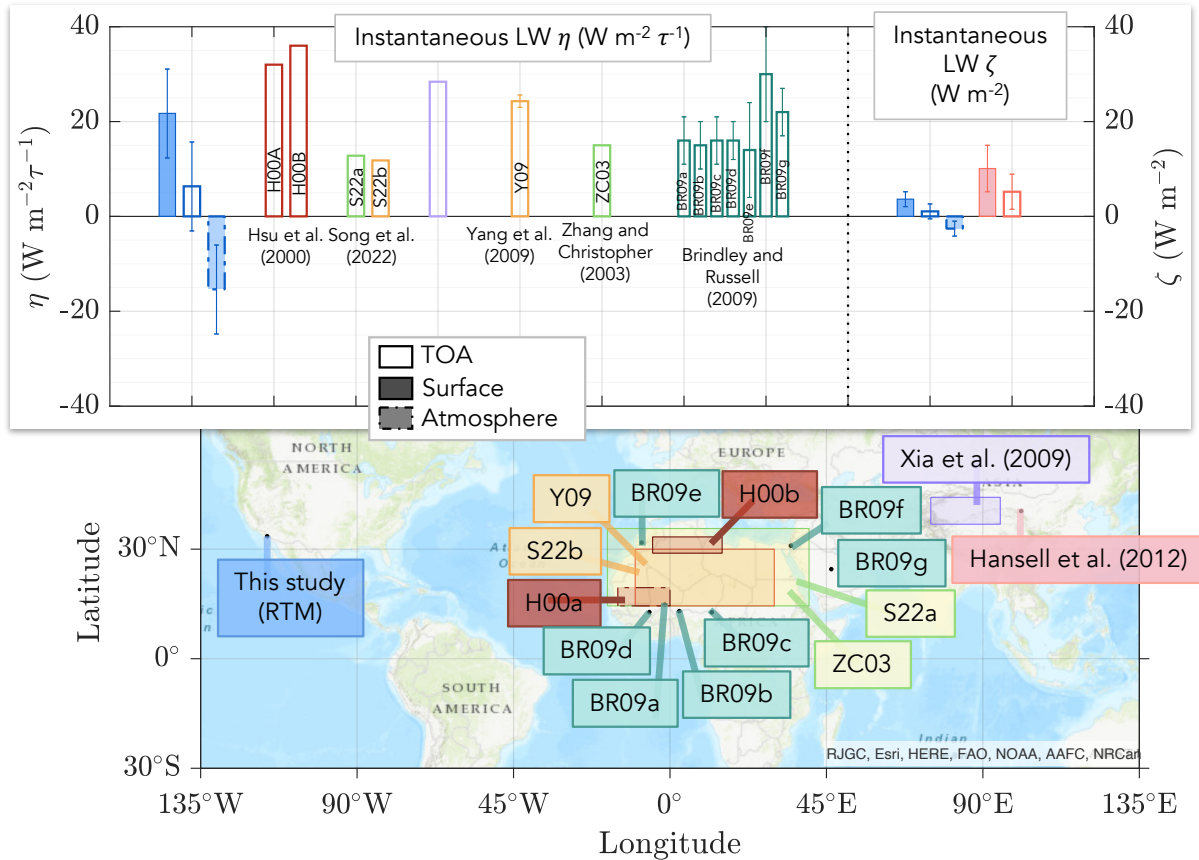


Figure 3.21: Shown are estimates of the clear-sky instantaneous LW η (left) and ζ (right) of dust at the surface (solid colored bar, solid line), TOA (clear bar, solid line), and atmosphere (solid colored bar, dotted line) from this and other studies. Black, closed circles denote the locations of the various studies. Presented here are the 1- σ uncertainty since this uncertainty was reported in the other studies (i.e. Hansell et al., 2012; Yang et al., 2009). The abbreviations S22a and S22b refer to the LW η from Song et al. (2022) over North Africa and the Sahara Desert, respectively; Y09 represents Yang et al. (2009); ZC03 represents Zhang and Christopher (2003); and BR09a, BR09b, BR09c, BR09d, BR09e, BR09f, and BR09g represents the LW η from Brindley and Russell (2009) based on data from the Agoufou, Banizoumbou, DMN Maine Soroa, Saada, Sede Boker, and Solar Village AERONET stations, respectively.

Estimates of the LW η_{∞} from this study differ more from that identified in Hsu et al. (2000), Xia and Zong (2009), and Yang et al. (2009) (Figure 3.21) and Brindley and Russell (2009) over Sede Boker (BR09f, Figure 3.21). It is possible that discrepancy between this study and these studies arise due to variability in the dust height among each study. For example, Hsu et al. (2000) used satellite-based observations to estimate the LW η_{∞} (per unit aerosol index and aerosol optical thickness) over both land and ocean and estimated the LW η over North

Africa (H00a and H00b, Figure 3.21) as roughly 32 and $36 \text{ W m}^{-2} \tau^{-1}$ for the winter (H00a) and summer (H00b); Hsu et al. (2000) recognized that differences between these winter and summer LW η_∞ estimates may be due to seasonal differences in dust source origin or water vapor content. In another study Xia and Zong (2009) reported that the dust aerosol layer typically extended from the surface to 4–6 km. These values are high in comparison to that from the Salton Sea, where dust height rarely extends beyond 2 km. The instantaneous LW η_∞ is particularly sensitive to the dust height because dust more efficiently reduces the amount of OLR at the TOA when dust resides at higher altitudes and lower temperatures.

Diurnal Comparisons

Next we compare the estimates of the clear-sky annual and diurnally averaged SW η at the surface, TOA, and atmosphere from this and other studies (Figure 3.22). The annual and diurnally averaged SW forcing efficiency at the surface η_0 and TOA η_∞ estimated from this study are statistically similar to that from Zhou, Yu, Dickinson, Dubovik, and Holben (2005) at SW $\alpha \sim 0.3$ (Figure 3.22). Zhou et al. (2005) investigated the relationship between SW η_0 and η_∞ as a function of SW α via an RTM. The inputs to this RTM and validation scheme were based on *in-situ* measurements from AERONET and binned in SW α intervals. It is encouraging that our estimates of the diurnally averaged SW η_0 and η_∞ are statistically similar to that from Zhou et al. (2005) at SW $\alpha \sim 0.3$ because Zhou et al. (2005) was conducted in a region with similar climate and surface type as that of the Salton Basin, where the average SW $\alpha \sim 0.3$.

The magnitude of the diurnally averaged SW η_0 from Ge et al. (2010), Balkanski et al. (2007), Valenzuela et al. (2012), García et al. (2014), Di Biagio et al. (2010), and Di Sarra et al. (2013) are greater than the magnitude of the annual and diurnally averaged SW η_0 estimated in this study (Figure 3.22). For example the diurnally averaged η_0 from Ge et al. (2010) and García et al. (2014) are -95.1 ± 10.3 and $-59 \pm 6 \text{ W m}^{-2} \tau^{-1}$, respectively (Figure 3.22). A reason for the η_0 discrepancy is differing dust optical and physical properties; for example the volume size distribution presented in Ge et al. (2010) suggests that dust particles greater than $10 \mu\text{m}$ are not

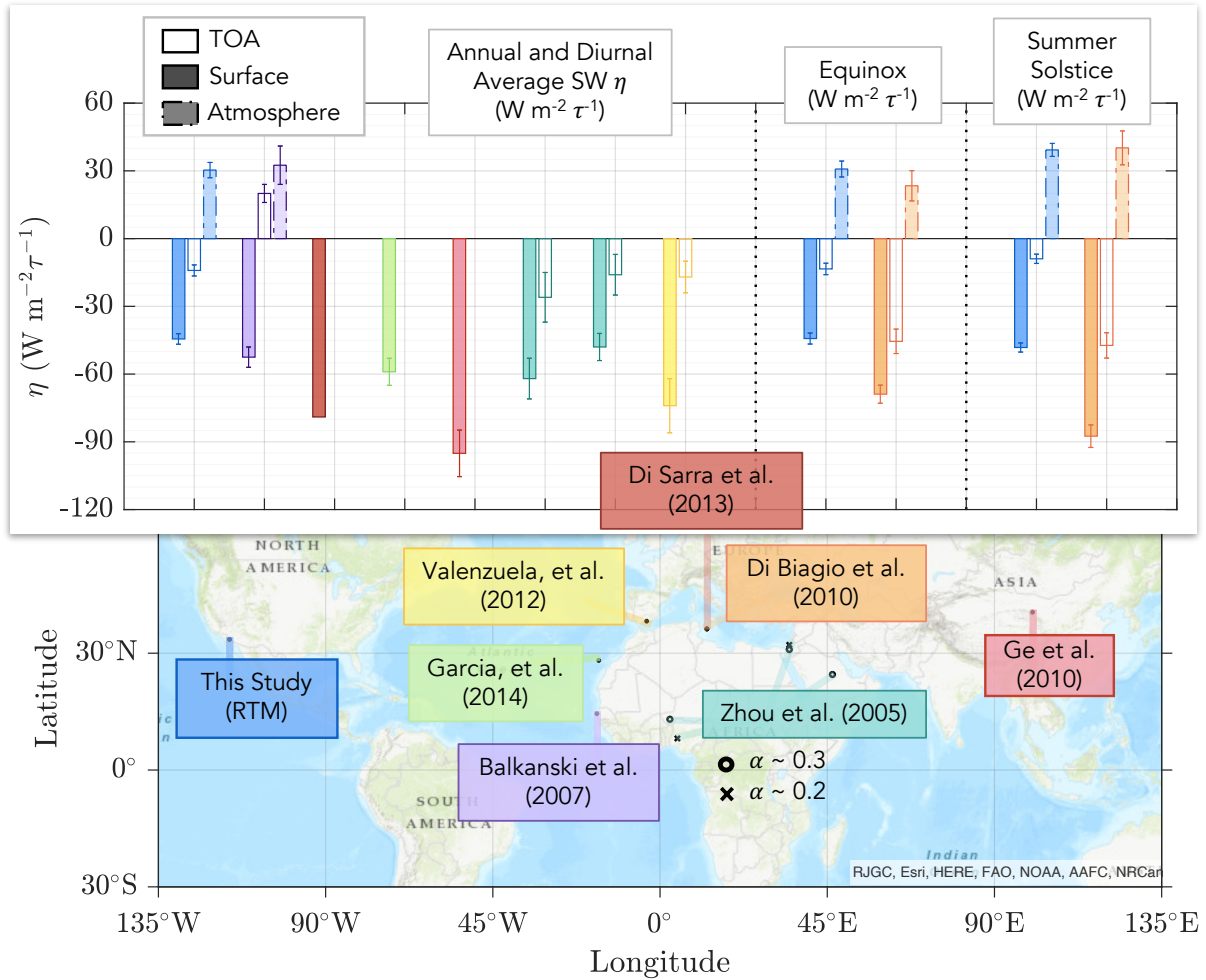


Figure 3.22: Clear-sky annual and diurnally averaged SW η at the surface (shaded colored bars, solid line), TOA (clear bars, solid line), and atmosphere (shaded colored bars, dot-dashed line) from this (blue) and other studies. Locations marked with an open black circle or black \times denote a surface with $\alpha \sim 0.3$ and $\alpha \sim 0.2$, respectively.

included in the analysis (not shown) and as a result, can lead to a η_0 that is more negative than that from this study. In regards to García et al. (2014) it is possible that suspended dust over the Canary Islands may be more reflective than dust suspended over the Salton Basin. We find that ω at 400 nm from García et al. (2014) is 0.96 ± 0.01 whereas in this study this parameter is roughly 0.8 at 400 nm. Additionally we find that the SW α in García et al. (2014) is 0.12 ± 0.01 , which is smaller than the average SW α over the field site. Both these conditions can result in dust being more reflective in the solar spectrum and can lead to a SW η_0 that is more negative.

The clear-sky annual and diurnally averaged LW η_∞ of dust is statistically similar to that from J. M. Haywood et al. (2005) (not shown). J. M. Haywood et al. (2005) used an RTM constrained with *in-situ* observations and retrievals from the SHADE campaign to model the OLR over North Africa (25°N, 11°E). J. M. Haywood et al. (2005) estimated the diurnally averaged LW η at the TOA as $20.6 \text{ W m}^{-2}\tau^{-1}$ (not shown), which is statistically dissimilar to the diurnally averaged LW η_∞ of dust estimated in this study ($4 \pm 10 \text{ W m}^{-2}\tau^{-1}$). It is possible that this disagreement arises because dust from J. M. Haywood et al. (2005) is highly absorptive for $4.5 < \lambda$. For example the spectral ω for $4.5 < \lambda$ ranges from approximately 0.05 to 0.2 in J. M. Haywood et al. (2005). For this spectral interval, the ω from this study is greater than 0.2 (Figure 3.10).

Even though there are estimates of the diurnally averaged LW ζ of dust at the TOA from other studies, here we only compare our estimate of the diurnally averaged LW η_∞ to that from J. M. Haywood et al. (2005) because it is not straightforward to compare the annual and diurnally averaged LW ζ between studies when the temporal or regionally averaged τ is unavailable or unknown. The magnitude of ζ is dependent on τ , which can vary as a function of space and λ .

3.6 Conclusion

In this study we described the ground and satellite-based instrumentation at the SIO field site in the Salton Basin (Section 3.2). In Section 3.2 we also describe the cloud and dust filtering algorithms, based on ceilometer and AERONET measurements and retrievals. We then described the RTM used in this study and validated the model output against observations (Section 3.3). We found that RRTM SW reproduced cloud free and dust laden surface SW fluxes with low bias ($RMSE = 2\%$, Figure 3.11 and $RMSE = 4\%$, Figure 3.13a). After correcting the observed TOA fluxes for biases that varied as a function of SW α we found low bias and high, positive correlation between the observed and modeled TOA SW fluxes ($RMSE = 11\%$, Figure 3.13b). Despite finding biases in the observed and modeled surface and TOA LW fluxes, observed and

modeled surface and TOA LW fluxes were positively and significantly correlated ($r = 0.99$, Figure 3.12 and $r = 0.87$, Figure 3.14a at the surface, and $r = 0.88$, Figure 3.14b at the TOA). Results presented here suggest that biases in the LW fluxes may be due to the representation of soil surface temperature, the vertical distribution of temperature and moisture, and the total content of water vapor in the atmosphere. We suggest future work that incorporates observations or retrievals of the soil surface temperature and further work to investigate these discrepancies.

In Section 3.4 we described the methods to estimate the clear-sky instantaneous SW forcing efficiency η of dust at the surface and top of the atmosphere (TOA) via the model and observational methods. Using the observational method we estimated the instantaneous SW η of dust at the surface η_0 and TOA η_∞ with collocated and all *in-situ* and satellite datasets (Section 3.5.1). After finding agreement between the SW η estimated with the collocated and all *in-situ* and satellite datasets, our best estimate of the SW η of dust via the observational method is $-101 \pm 7 \text{ W m}^{-2}\tau^{-1}$ at the surface and $-10 \pm 47 \text{ W m}^{-2}\tau^{-1}$ at the TOA (Figures 3.16 and 3.17b). A limitation with using the observational method to estimate η_∞ is that the sample size of the satellite data was small, leading to low precision in the estimate of the SW η_∞ (i.e. relative uncertainty $> 100\%$). We suggest future work centered on utilizing a variety of satellite observations and retrievals (i.e. geostationary satellites) to estimate the clear-sky instantaneous TOA SW η over desert regions.

After validating the RRTM output we find that the clear-sky instantaneous SW and LW η_0 estimated via the model method are -105 ± 7 (Figures 3.16 and 3.17b) and $22 \pm 19 \text{ W m}^{-2}\tau^{-1}$ (Figure 3.18), respectively. The SW component is statistically similar to the instantaneous SW η_0 estimated with the observational method (Figure 3.16). We also find that the atmospheric SW η estimated via the model ($66 \pm 9 \text{ W m}^{-2}\tau^{-1}$) and observational ($91 \pm 47 \text{ W m}^{-2}\tau^{-1}$) methods are statistically significant. These findings suggest that in the SW spectrum dust primarily cools and warms the surface and atmosphere, respectively.

In comparison to other studies the instantaneous SW η_0 and η_∞ from this study are statistically dissimilar to that from Di Biagio et al. (2010), Di Sarra et al. (2013), and Kuwano

and Evan (2022) (Figure 3.20). Differences in the SW η are likely due to differing SW α and dust size. For example it is possible that dust suspended over the field site is more representative of freshly emitted dust, which may contain larger dust particles than dust transported over a larger distance (Song et al., 2022) and can result in a more positive SW η_0 . These comparisons highlight the dependency of the η on the underlying SW α and complexities related to dust optical and microphysical effects that lead to competing radiative effects. For example a dusts' mineral composition may indicate that dust more efficiently absorbs SW radiation, which can result in a more positive SW η_∞ (Sokolik & Toon, 1996). However if these dust particles are small, the SW η_∞ may become more negative (Kok et al., 2017; Song et al., 2022) and compete against the SW warming effect due to dust mineralogy.

In the LW spectrum our results were more statistically similar to that from Hansell et al. (2012), Song et al. (2022), Zhang and Christopher (2003), and Brindley and Russell (2009) (Figure 3.21). We achieved similar results with Hansell et al. (2012) despite dust over Zhangye being more absorbing and smaller than dust over the Salton Basin. We recognize, however, that the magnitude of the LW η of dust over the Salton basin may be dependent on the model biases in the LW fluxes presented here. As such we suggest further work to reduce model biases in the LW fluxes and to develop an observational or semi-observational method to estimate the surface and TOA LW η over the Salton Basin. An observation-based estimate of the LW η can act as a validation metric to evaluate model output and potentially increase confidence of the modeled LW η of dust over the field site.

After finding agreement between the observation and model-based estimates of the surface and atmospheric SW instantaneous η of dust over the field site, we ran RRTM SW and LW with the diurnal cycles of μ , q , $T(z)$, and $P(z)$ (Section 3.5.3). We ran these simulations at a constant τ ($= 0.17$), $\beta(z)$ scaled by τ , and $w(z)$ scaled by q . We then estimate the annual and diurnally averaged SW and LW η of dust via a Monte Carlo method (i.e. Section 3.4.3). We find that the annual and diurnally averaged SW η is $-44 \pm 2 \text{ W m}^{-2} \tau^{-1}$ at the surface, $-14 \pm 2 \text{ W m}^{-2} \tau^{-1}$ at the TOA, and $30 \pm 3 \text{ W m}^{-2} \tau^{-1}$ in the atmosphere (Figure 3.19). The corresponding

LW surface, TOA, and atmospheric η of dust are 15 ± 10 , 4 ± 10 , and $-11 \pm 14 \text{ W m}^{-2}\tau^{-1}$, respectively. These results produce an annual and diurnally averaged net effect at the surface, TOA, and atmosphere of -29 ± 10 , -10 ± 11 , and $19 \pm 15 \text{ W m}^{-2}\tau^{-1}$, respectively (Figure 3.19). Upon comparisons with other studies (Section 3.5.4 and Figure 3.22) there is consistency among other dust source regions that dust tends to cool at the surface in the SW spectrum. The magnitude of such cooling, however, is dependent on the optical and physical properties of dust and the underlying surface type (i.e. desert vs ocean). It is particularly encouraging that our estimates of the diurnally averaged SW η_0 and η_∞ of dust are statistically similar to that from Zhou et al. (2005) because Zhou et al. (2005) estimated this value over regions with SW $\alpha \sim 0.3$, which is nearly identical to the temporally averaged SW α over the field site. Our results differed most from that of Ge et al. (2010) primarily because of differing physical properties (Figure 3.22).

The sign of the diurnally averaged net η of dust at the surface and atmosphere estimated in this study (Figure 3.19) suggests that dust has an overall cooling effect at the surface and warming effect in the atmosphere over the Salton Basin; thus it is possible that these effects may have implications for semi-direct effects in the Salton Basin. For example simultaneous cooling of the surface and heating of the atmosphere can alter the vertical temperature distribution and stability within the atmosphere. On a broader climate perspective the dust net effect at the TOA is of particular importance but unconstrained in this study. It is essential that research efforts include reducing the uncertainty in the TOA η of dust over deserts and other dust source regions. Of particular importance dust has the potential to induce a SW warming effect at the TOA over desert regions because suspended dust can be more optically dark than the underlying desert surface and as a result, enhance warming within the dust layer. As such we suggest further work to reduce the uncertainty in the SW η_∞ over the Salton Basin to investigate whether or not dust cools or warms the TOA in the SW and LW spectrums.

This study was conducted in a small dust source region that is predicted to experience more dust activity in the coming years. As exposed playa from the Salton Sea dries and becomes

more susceptible to erosion, it is possible that these dust radiative effects may change. Thus it is essential that future work is done in this region to understand how the direct radiative effect of dust may change as dust mineralogy changes in this region. Furthermore to our knowledge this is the first study to use both observations and model output to estimate the SW, LW, and net η of dust in the Americas. It is important that observation and model-based estimates of the SW, LW, and net η of dust are made in these regions because these estimates can be used to validate the output from climate models, of which quantify on a global scale how much and if dust warms or cools the Earth's climate system.

3.7 Acknowledgements

Funding for this work was provided for by NSF Award AGS-1833173. We thank Robert Frouin, Blake Walkowiak, Tyler Barbero, Trinity Robinson, and Sophie Wynn for their contributions towards this project. Measurements obtained from the CERES SSF level 2 data product can be obtained from <https://ceres.larc.nasa.gov/data/>.

Reanalysis data were acquired from Japan Meteorological Agency (accessed on May 4th, 2023 via <https://rda.ucar.edu/datasets/ds628.0/dataaccess/>). AERONET retrievals can be accessed publicly from the AERONET website (<https://aeronet.gsfc.nasa.gov>). Processed Vaisala radiosonde data for various launches from 2020–2022 and Vaisala CL51 ceilometer profiles can be accessed publicly from <https://library.ucsd.edu/dc/collection/bb9839221k>. Raw and processed surface SW flux measurements can be obtained via personal communication. For the calibration procedure we utilize the solarPosition calculator (Mikofski, 2016) from the MATLAB file exchange <https://www.mathworks.com/matlabcentral/fileexchange/58405-solar-position-calculator> (retrieved December 6th, 2022). Davis met station data can be publicly accessed from MesoWest station FW7082 Salton City <https://mesowest.utah.edu/>. PM_{10} data can be accessed from the California Air Resources Board at <https://www.arb.ca.gov/aqmis2/aqdselect.php>.

The Rapid Radiative Transfer Model in the SW (Atmospheric & Environmental Research, 2004) and LW (Atmospheric & Environmental Research, 2010) can be accessed via http://rtweb.aer.com/rrtm_frame.html. Dust mineralogy and complex refractive index calculations for this study were conducted by Blake Walkowiak (Walkowiak, 2022) and scattering properties were obtained from the TAMUdust2020 database (Saito & Yang, 2021b), which can be accessed via <https://github.com/masasaito/TAMUdust2020>.

Chapter 3, in part, is currently being prepared for submission for publication of the material. A. M. Kuwano; A. T. Evan; B. C. Walkowiak; R. Frouin. The dissertation author was the primary investigator and author of this material.

3.8 Supplemental

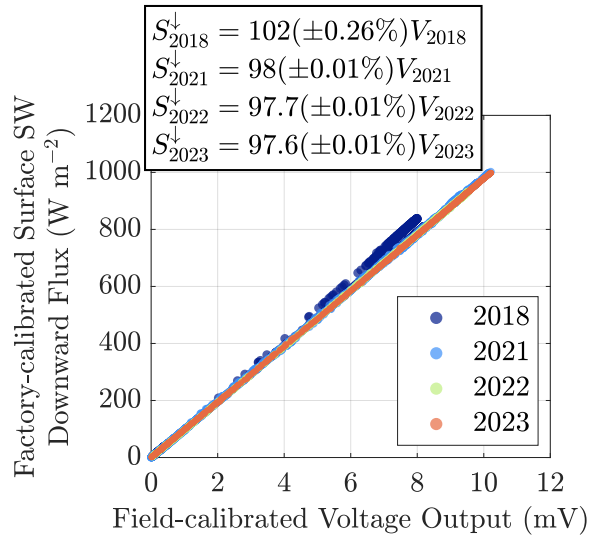


Figure 3.23: Scatter plots of the observed surface SW downward flux (S^{\downarrow}) from the factory-calibrated pyranometer (y-axis, $W\ m^{-2}$) and the voltage output V from the field-calibrated pyranometer (x-axis, mV). Each color denotes the data during each calibration period (i.e. orange for the calibration period in April–May 2023). The calibration coefficients (in $W\ m^{-2}\ mV^{-1}$) and relative uncertainty are displayed where subscripts $()_{2018}$, $()_{2021}$, $()_{2022}$, and $()_{2023}$ represent the results for each calibration period. The calibration coefficients for the factory-calibrated pyranometer during the calibration periods of 2018 and 2023 are $91.3 \pm 2\%$ and $89.9 \pm 2\%$ $W\ m^{-2}\ mV^{-1}$, respectively.

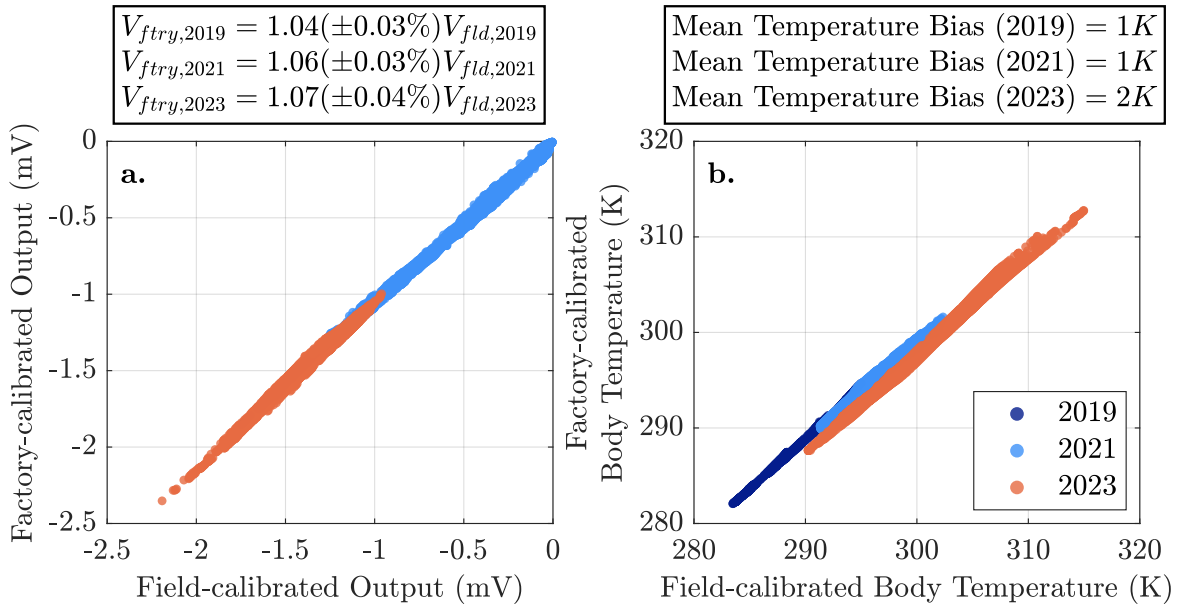


Figure 3.24: Shown are scatter plots of the (a) voltage output V from the factory (y-axis) and field-calibrated (x-axis) pyrgeometers and the (b) body temperature of the factory (y-axis) and field-calibrated (x-axis) pyrgeometers during each calibration period. Each color denotes the data during each calibration period (i.e. orange for the calibration period in April–May 2023). The calibration coefficients (in $\text{W m}^{-2} \text{mV}^{-1}$), relative uncertainty, and mean temperature bias (in K) are shown where subscripts $(\)_{2019}$, $(\)_{2021}$, and $(\)_{2023}$ represent the results for each calibration period. The subscripts $(\)_{ftry}$ and $(\)_{fld}$ indicate the factory and field-calibrated instruments, respectively. The factory-calibrated pyrgeometer calibration coefficients during the calibration periods of 2019 and 2023 are $76.3 \pm 5\%$ and $78.6 \pm 4\%$ $\text{W m}^{-2} \text{mV}^{-1}$, respectively

Table 3.2: Days and start times for each radiosonde launch considered in RRTM SW and LW.

Date (dd MMM yyyy)	Time (HH:mm, UTC)
22 February 2020	16:00
22 February 2020	18:00
29 February 2020	23:00
28 February 2021	16:00
28 February 2021	18:00
09 March 2021	15:00
09 March 2021	17:00
09 March 2021	19:00
09 March 2021	20:00
09 March 2021	22:00
09 March 2021	23:00
15 February 2022	22:00
15 February 2022	23:00

Chapter 4

Conclusions

4.1 Summary of Key Findings and Novelty

In this dissertation, observations, retrievals, and model output were used to estimate the dust SW and LW forcing efficiency FE over two dust source regions. The main goals for this work were to validate an observational method to estimate the SW FE , investigate the physical processes governing the uncertainties related to estimating the FE of dust with models and observations, and constrain the sign and magnitude of the the SW, LW, and net (SW + LW) FE at the surface, top of the atmosphere (TOA), and atmosphere over the Salton Basin.

In Chapter 2 satellite measurements and a radiative transfer model (RTM) were used to investigate the uncertainty in the clear-sky TOA SW FE of dust over one of the major dust source regions, the Sahara Desert (Ginoux, Prospero, Gill, Hsu, & Zhao, 2012). We found significant correlations between aerosol optical depth τ and total precipitable water vapor q . Using a hierarchy of RTMs we found that a correlation between τ and q led to biases in the observation-based estimates of the TOA SW FE of dust. The output from these models also showed that by using a modified method to estimate the SW FE of dust, biases in the dust TOA SW η were reduced by 11–58%. A modification of the observational method to estimate the TOA SW FE of dust was described; the crux of this method was to use statistical analysis to remove the effect of water vapor on the TOA SW upward flux. We then applied this observational method to satellite observations and retrievals to estimate the TOA SW FE of dust over the Sahara Desert;

the instantaneous clear-sky SW FE of dust ranged from 2.35 ± 139 to $-26.4 \pm 17.6 \text{ W m}^{-2}\tau^{-1}$. One of the novelties of this study was that only observations and retrievals were used to estimate the TOA SW FE of dust over a major dust source region while also reducing the uncertainty in the TOA SW FE . Furthermore results from this study are in agreement with other studies in that dust tends to induce a warming effect or weakened cooling effect at the TOA over bright surfaces (Ansell et al., 2014; Yang et al., 2009) such as the Sahara Desert and other dust source regions (i.e. the Gobi Desert). Values of positive or near zero TOA SW FE can skew the globally averaged TOA SW FE of dust towards a more positive value, which has been found in previous studies (Kok et al., 2017; Di Biagio et al., 2020). Another novelty was that the validation and uncertainty analysis conducted in this study were the foundation for the methods in subsequent observational and modeling research that we completed in a small dust source region (Chapter 3).

In Chapter 3 a combination of RTM output and ground and satellite-based measurements were used to estimate the clear-sky instantaneous and diurnally averaged SW, LW, and net η of dust over the Salton Basin. Model validations were conducted on the output from the Rapid Radiative Transfer Model (RRTM) in the SW and LW spectrum by comparing model output to observations of SW and LW fluxes. After finding agreement between modeled and observed fluxes we applied two independent methods to estimate the instantaneous surface and TOA SW FE of dust to surface and satellite measurements. The instantaneous surface, TOA, and atmospheric SW FE of dust estimated via the observational method are -101 ± 7 , -10 ± 47 , and $91 \pm 47 \text{ W m}^{-2}\tau^{-1}$, respectively. Correspondingly the model-based SW FE of dust is -105 ± 7 , -38 ± 7 , and $66 \pm 9 \text{ W m}^{-2}\tau^{-1}$ at the surface, TOA, and atmosphere, respectively. Output from RRTM was also used to estimate the instantaneous LW FE of dust over the Salton Basin as 22 ± 19 , 6 ± 9 , and $-15 \pm 21 \text{ W m}^{-2}\tau^{-1}$ at the surface, TOA, and atmosphere, respectively. Model output was then used to derive the diurnally averaged surface, TOA, and atmospheric FE of dust in the SW, LW, and net; we note that this diurnal average is more representative of an annually and diurnally averaged FE of dust during dust storms. Values of this parameter

are -44 ± 2 (SW), 15 ± 10 (LW), and -29 ± 10 (net) $\text{W m}^{-2}\tau^{-1}$ at the surface; -14 ± 2 (SW), 4 ± 10 (LW), and -10 ± 11 (net) $\text{W m}^{-2}\tau^{-1}$ at the TOA; and 30 ± 3 (SW), -11 ± 14 (LW), and 19 ± 15 (net) $\text{W m}^{-2}\tau^{-1}$ for the atmosphere. A significance of the results presented in Chapter 3 is that agreement was found between model and observation-based estimates of the instantaneous SW *FE* of dust. As a result it was possible to estimate the diurnally averaged SW, LW, and net *FE* of dust over the Salton Basin via model output. Furthermore to the best of our knowledge these are the first observational and model estimates of the instantaneous and diurnally averaged SW, LW, and net *FE* of dust in the Americas. Another significance of these findings is that the methods in Chapter 3 are based on the observational method described and validated in Chapter 2. Though the instantaneous SW *FE* of dust from both chapters were statistically dissimilar to one another, this comparison provides possible insight into the differences in the optical properties of dust found in the Sahara Desert and over the Salton Basin. This comparison also suggests that dust may induce a warming or weak cooling effect at the TOA over both major and minor dust source regions (i.e. brighter surfaces).

A main novelty of the results from this dissertation is that the results presented here contribute towards the breadth of observational estimates of the SW *FE* of dust at the surface and TOA over dust source regions. These results can be used to gain insight into the relationship between dust and climate over small dust source regions that may become dustier over the next several years due to land use changes. For example the current dust optical properties found nearby the field site in the Salton Basin may, in the future, become more absorbing or reflective in the SW. This change can alter the magnitude of the surface, TOA, and atmospheric net *FE* of dust in this region and change the vertical temperature distribution in the atmosphere (Helmert et al., 2007; Johnson et al., 2004). These changes can affect local weather or induce dust feedbacks (Kok et al., 2018). On a broader scale the estimates of the SW and LW *FE* of dust presented in this dissertation can also be used to validate global climate model output and potentially lower uncertainties in the globally averaged *FE* of dust.

4.2 Remaining Questions

Though we estimated the relationship between instantaneous TOA SW FE of dust and the cosine of the solar zenith angle μ (Chapter 2), we were not able to estimate the diurnally averaged TOA SW FE of dust over the Sahara Desert due to challenges with data availability. For example the satellite measurements used in the analysis in Chapter 2 were from sun synchronous satellites which only cross over the Earth's surface twice a day. This limited temporal resolution prevented us from obtaining satellite measurements near sunrise and sunset where solar zenith angles θ are high. As such we could not fully derive the variability of the instantaneous TOA SW FE of dust as a function of μ . We suggest further work to acquire, develop, and process geostationary datasets of observed SW fluxes to estimate the TOA SW FE of dust over desert regions.

One of the main limitations with the analysis from Chapter 3 was that the uncertainty in the TOA SW FE was over 100% and as a result, the sign of the TOA SW FE of dust is unconstrained over the Salton Basin. Further work can focus on utilizing other satellite-based measurements or extending the satellite-based dataset beyond 2020. A challenge with extending this data beyond 2020 is that an algorithm to identify dust from satellite observations and retrievals must be developed. Previous algorithms have been developed to estimate the dust τ but many of these studies were conducted on a larger scale and not over a small dust source region. Another limitation in this analysis was that we do not compare our model estimates of the surface, TOA, and atmospheric LW FE of dust to that estimated with observations over the Salton Basin. It is essential that an observational or semi-observational method to estimate the clear-sky instantaneous LW FE at the surface and TOA is developed. To our knowledge there are very few, if any, observational estimates of the clear-sky instantaneous LW FE of dust at the surface over dust source regions. A limitation with the LW model analysis in Chapter 3 was a lack of observations of the soil surface temperature at the field site, of which the soil surface LW emissivity ε is highly dependent on. Additionally it would be beneficial to incorporate a

spectrally dependent LW ε in RRTM LW. A next step in the modeling analysis would be to obtain a complete record of *in-situ* measurements and retrievals of the size distribution and shape of dust emitted over the Salton Basin. Since we approximate the variation of dust size distribution with height it would be advantageous to obtain *in-situ* measurements of the dust size distribution as a function of height. It would also be beneficial to incorporate the full diurnal cycle of τ (night and day) in the diurnal RRTM simulations in order to more fully capture the diurnal variation of *DRE* and *FE*, especially in the LW, as a function of μ .

Glossary

Aerosol optical depth	The e-folding scale of extinction of radiation through an aerosol layer.
Angstrom exponent	A measure of how aerosol optical depth changes as a function of wavelength.
Asymmetry parameter	A measure of the preferential scattering direction of a medium (> 0 represents forward scattering, < 0 represents backscattering, and $= 0$ denotes isotropic scattering).
Ceilometer	An instrument that uses a laser to detect the presence of cloud or aerosol particles.
Clear-sky	Cloud free.
Direct radiative effect	The difference between the net fluxes in clear-sky and pristine-sky conditions.
Extinction coefficient	A measure of how much radiation is extinguished (absorbed or scattered) as light passes through a medium (units: inverse length, i.e. km^{-1}).

Fine-mode-fraction	The fraction of fine-mode to total (fine and coarse) particles.
Forcing efficiency	The direct radiative effect normalized by the aerosol optical depth.
Longwave radiation	Radiation for wavelengths greater than $\sim 4\mu\text{m}$.
Outgoing longwave radiation	The LW upward flux at the TOA.
Particulate matter (PM_{10})	The concentration of particles suspended in the atmosphere (solid or liquid) that have diameters smaller than $10\mu\text{m}$.
Pristine-sky	Cloud and aerosol free.
Pyranometer	A radiometric instrument that measures broadband SW fluxes.
Pyrgeometer	A radiometric instrument that measures broadband LW fluxes.
Sample size	The number of observations available for an analysis.
Shortwave radiation	Radiation for wavelengths less than $\sim 4\mu\text{m}$.
Single scatter albedo	The fraction of the scattering and extinction (scattering and absorbing) coefficients.
Size distribution	The amount of different size particles suspended in the atmosphere. Can be sorted by number concentration, mass, and volume.

Solar zenith angle	The angle measured at the surface from the sun and a unit normal to the surface.
Surface albedo	The fraction of upward and downward flux at the surface.
Total precipitable water	The depth of water in a column of atmosphere if all the water vapor in the atmospheric column were condensed (units: mm or cm).

Bibliography

- Adebiyi, A. A., & Kok, J. F. (2020). Climate models miss most of the coarse dust in the atmosphere. *Science Advances*, 6(15). doi: 10.1126/sciadv.aaz9507
- Anderson, G. P., Clough, S. A., Kneizys, F., Chetwynd, J. H., & Shettle, E. P. (1986). *Afgl atmospheric constituent profiles (0.120 km)* (Tech. Rep.). Air Force Geophysics Lab Hanscom AFB MA.
- Ångström, A. (1964). The parameters of atmospheric turbidity. *Tellus*, 16(1), 64–75.
- Ansell, C., Brindley, H. E., Pradhan, Y., & Saunders, R. (2014). Mineral dust aerosol net direct radiative effect during gerbils field campaign period derived from sevir and gerb. *Journal of Geophysical Research: Atmospheres*, 119(7), 4070-4086. doi: 10.1002/2013JD020681
- Atmospheric, & Environmental Research, I. (2004, 4 01). *Rrtm_sw* [Software v2.5]. Retrieved from http://rtweb.aer.com/rrtm_frame.html
- Atmospheric, & Environmental Research, I. (2010, 5 01). *Rrtm_lw* [Software v3.3]. Retrieved from http://rtweb.aer.com/rrtm_frame.html
- Balkanski, Y., Schulz, M., Claquin, T., & Guibert, S. (2007). Reevaluation of mineral aerosol radiative forcings suggests a better agreement with satellite and aernet data. *Atmospheric Chemistry and Physics*, 7(1), 81–95. doi: 10.5194/acp-7-81-2007
- Bedka, S., Knuteson, R., Revercomb, H., Tobin, D., & Turner, D. (2010). An assessment of the absolute accuracy of the atmospheric infrared sounder v5 precipitable water vapor product at tropical, midlatitude, and arctic ground-truth sites: September 2002 through august 2008. *Journal of Geophysical Research: Atmospheres*, 115(D17). Retrieved from <https://agupubs.onlinelibrary.wiley.com/doi/abs/10.1029/2009JD013139> doi: <https://doi.org/10.1029/2009JD013139>
- Bevis, M., Businger, S., Chiswell, S., Herring, T. A., Anthes, R. A., Rocken, C., & Ware, R. H. (1994). Gps meteorology: Mapping zenith wet delays onto precipitable water. *Journal of Applied Meteorology (1988-2005)*, 33(3), 379–386. Retrieved from <http://www.jstor.org/stable/26186685>
- Bohren, C. F., & Huffman, D. R. (2008). *Absorption and scattering of light by small particles*. John Wiley & Sons.
- Brindley, H. E. (2007). Estimating the top-of-atmosphere longwave radiative forcing due to saharan dust from satellite observations over a west african surface site. *Atmospheric Science Letters*, 8(3), 74-79. doi: <https://doi.org/10.1002/asl.155>
- Brindley, H. E., & Russell, J. E. (2009). An assessment of saharan dust loading and the corresponding cloud-free longwave direct radiative effect from geostationary satellite observations. *Journal of Geophysical Research: Atmospheres*, 114(D23). doi: <https://doi.org/10.1029/2009JD013139>

doi.org/10.1029/2008JD011635

- Cg4 pyrgeometer instruction manual [Computer software manual]. (2001). Retrieved from <https://www.kippzonen.com/Download/33/CG-4-Manual>
- Chou, C., Formenti, P., Maille, M., Auset, P., Helas, G., Harrison, M., & Osborne, S. (2008). Size distribution, shape, and composition of mineral dust aerosols collected during the african monsoon multidisciplinary analysis special observation period 0: Dust and biomass-burning experiment field campaign in niger, january 2006. *Journal of Geophysical Research: Atmospheres*, 113(D23). Retrieved from <https://agupubs.onlinelibrary.wiley.com/doi/abs/10.1029/2008JD009897> doi: <https://doi.org/10.1029/2008JD009897>
- Chrien, T. G., Green, R. O., & Eastwood, M. L. (1990). Accuracy of the spectral and radiometric laboratory calibration of the airborne visible/infrared imaging spectrometer. In *Imaging spectroscopy of the terrestrial environment* (Vol. 1298, pp. 37–49).
- Christopher, S. A., & Zhang, J. (2002). Shortwave aerosol radiative forcing from MODIS and CERES observations over the oceans. *Geophysical Research Letters*, 29(18), 6-1-6-4. doi: 10.1029/2002GL014803
- Chylek, P., Srivastava, V., Pinnick, R. G., & Wang, R. (1988). Scattering of electromagnetic waves by composite spherical particles: experiment and effective medium approximations. *Applied Optics*, 27(12), 2396–2404. doi: 10.1364/AO.27.002396
- Claquin, T., Schulz, M., & Balkanski, Y. (1999). Modeling the mineralogy of atmospheric dust sources. *Journal of Geophysical Research: Atmospheres*, 104(D18), 22243–22256. doi: 10.1029/1999JD900416
- Clough, S. A., Shephard, M. W., Mlawer, E. J., Delamere, J. S., Iacono, M. J., Cady-Pereira, K., Boukabara, S., & Brown, P. D. (2005). Atmospheric radiative transfer modeling: a summary of the aer codes. *Journal of Quantitative Spectroscopy and Radiative Transfer*, 91(2), 233-244. Retrieved from <https://www.sciencedirect.com/science/article/pii/S0022407304002158>
- Cm21 precision pyranometer instruction manual [Computer software manual]. (2004). Retrieved from <https://www.kippzonen.com/Download/52/CM-21-Pyranometer-Manual>
- Conant, W. C. (2000). An observational approach for determining aerosol surface radiative forcing: Results from the first field phase of INDOEX. *Journal of Geophysical Research: Atmospheres*, 105(D12), 15347–15360. doi: 10.1029/1999JD901166
- Das, R., Evan, A., & Lawrence, D. (2013). Contributions of long-distance dust transport to atmospheric p inputs in the yucatan peninsula. *Global Biogeochemical Cycles*, 27(1), 167-175. doi: 10.1029/2012GB004420
- Davis, K. (2017, 3 12). Border patrol agent killed while assisting with crash in imperial valley. *The San Diego Union Tribune*. Retrieved 2021-03-16, from [https://urldefense.com/v3/_https://www.sandiegouniontribune.com/news/public-safety/story/2021-03-16/border-patrol-agent-killed_;;!!Mih3wA!DJTFWPku9aF9CseM9lXbKf_UkAc3bTasfphULI27xLCYlyHAc_T9YLmcx0eQD3A1220R7yeIeiLbBuY\\$](https://urldefense.com/v3/_https://www.sandiegouniontribune.com/news/public-safety/story/2021-03-16/border-patrol-agent-killed_;;!!Mih3wA!DJTFWPku9aF9CseM9lXbKf_UkAc3bTasfphULI27xLCYlyHAc_T9YLmcx0eQD3A1220R7yeIeiLbBuY$)
- DeMott, P. J., Cziczo, D. J., Prenni, A. J., Murphy, D. M., Kreidenweis, S. M., Thomson, D. S., Borys, R., & Rogers, D. C. (2003). Measurements of the concentration and composition of nuclei for cirrus formation. *Proceedings of the National Academy of Sciences*, 100(25),

- 14655–14660. doi: 10.1073/pnas.2532677100
- DeMott, P. J., Prenni, A. J., Liu, X., Kreidenweis, S. M., Petters, M. D., Twohy, C. H., Richardson, M., Eidhammer, T., & Rogers, D. (2010). Predicting global atmospheric ice nuclei distributions and their impacts on climate. *Proceedings of the National Academy of Sciences*, *107*(25), 11217–11222. doi: 10.1073/pnas.0910818107
- Department of Atmospheric Science, U. o. W. (n.d.). *Upperair, soundings*. Retrieved from <http://weather.uwyo.edu/upperair/sounding.html> (Accessed on 2023-3-3)
- Di Biagio, C., Balkanski, Y., Albani, S., Boucher, O., & Formenti, P. (2020). Direct radiative effect by mineral dust aerosols constrained by new microphysical and spectral optical data. *Geophysical Research Letters*, *47*(2), e2019GL086186. doi: 10.1029/2019GL086186
- Di Biagio, C., Formenti, P., Balkanski, Y., Caponi, L., Cazaunau, M., Pangui, E., Journet, E., Nowak, S., Andreae, M. O., Kandler, K., Saeed, T., Piketh, S., Seibert, D., Williams, E., & Doussin, J. F. (2019). Complex refractive indices and single-scattering albedo of global dust aerosols in the shortwave spectrum and relationship to size and iron content. *Atmospheric Chemistry and Physics*, *19*(24), 15503–15531. doi: 10.5194/acp-19-15503-2019
- Di Biagio, C., Di Sarra, A., & Meloni, D. (2010). Large atmospheric shortwave radiative forcing by Mediterranean aerosols derived from simultaneous ground-based and spaceborne observations and dependence on the aerosol type and single scattering albedo. *Journal of Geophysical Research: Atmospheres*, *115*(D10). doi: 10.1029/2009JD012697
- Di Biagio, C., Di Sarra, A., Meloni, D., Monteleone, F., Piacentino, S., & Sferlazzo, D. (2009). Measurements of Mediterranean aerosol radiative forcing and influence of the single scattering albedo. *Journal of Geophysical Research: Atmospheres*, *114*(D6). doi: 10.1029/2008JD011037
- Di Biagio, C., Formenti, P., Balkanski, Y., Caponi, L., Cazaunau, M., Pangui, E., Journet, E., Nowak, S., Caquineau, S., Andreae, M. O., Kandler, K., Saeed, T., Piketh, S., Seibert, D., Williams, E., & Doussin, J.-F. (2017). Global scale variability of the mineral dust long-wave refractive index: a new dataset of in situ measurements for climate modeling and remote sensing. *Atmospheric Chemistry and Physics*, *17*(3), 1901–1929. doi: 10.5194/acp-17-1901-2017
- Di Sarra, A., Fuà, D., & Meloni, D. (2013). Estimate of surface direct radiative forcing of desert dust from atmospheric modulation of the aerosol optical depth. *Atmospheric Chemistry and Physics*, *13*(11), 5647–5654. Retrieved from <https://acp.copernicus.org/articles/13/5647/2013/> doi: 10.5194/acp-13-5647-2013
- Evan, A., Walkowiak, B., & Frouin, R. (2022). On the misclassification of dust as cloud at an aeronet site in the sonoran desert. *Journal of Atmospheric and Oceanic Technology*, *39*(2), 181 - 191. Retrieved from <https://journals.ametsoc.org/view/journals/atot/39/2/JTECH-D-21-0114.1.xml> doi: 10.1175/JTECH-D-21-0114.1
- Evan, A. T. (2019). Downslope winds and dust storms in the salton basin. *Monthly Weather Review*, *147*(7), 2387 - 2402. doi: 10.1175/MWR-D-18-0357.1
- Evan, A. T., Flamant, C., Lavaysse, C., Kocha, C., & Saci, A. (2015). Water vapor-forced greenhouse warming over the Sahara Desert and the recent recovery from the Sahelian drought. *Journal of Climate*, *28*(1), 108–123. doi: 10.1175/JCLI-D-14-00039.1
- Evan, A. T., Frouin, R., Kuwano, A., Barbero, T., Wynn, S., & Robinson, T. (2022a). *Measure-*

- ments from radiosondes*. Boulder CO: UC San Diego Library Digital Collections. Retrieved from <https://doi.org/10.6075/J0ZG6SFK> doi: <https://doi.org/10.6075/J0ZG6SFK>
- Evan, A. T., Frouin, R., Kuwano, A., Barbero, T., Wynn, S., & Robinson, T. (2022b). *Meteorological and aerosol measurements near the salton sea, california*. UC San Diego Library Digital Collections. Retrieved from <https://library.ucsd.edu/dc/collection/bb9839221k> (Accessed on 2023-2-4) doi: <https://doi.org/10.6075/J0XP7547>
- Evan, A. T., & Mukhopadhyay, S. (2010). African dust over the northern tropical Atlantic: 1955-2008. *Journal of Applied Meteorology and Climatology*, 49(11), 2213–2229. doi: 10.1175/2010JAMC2485.1
- Flamant, C., Chaboureaud, J. P., Parker, D. J., Tayler, C. M., Cammas, J. P., Bock, O., Timouk, F., & Pelon, J. (2007). Airborne observations of the impact of a convective system on the planetary boundary layer thermodynamics and aerosol distribution in the inter-tropical discontinuity region of the West African Monsoon. *Quarterly Journal of the Royal Meteorological Society*, 133, 1175–1189. doi: 10.1002/qj.97
- García, R., García, O., Cuevas, E., Cachorro, V., Romero-Campos, P., Ramos, R., & De Frutos, A. (2014). Solar radiation measurements compared to simulations at the bsrn izaña station. mineral dust radiative forcing and efficiency study. *Journal of Geophysical Research: Atmospheres*, 119(1), 179–194.
- Ge, J. M., Su, J., Ackerman, T. P., Fu, Q., Huang, J. P., & Shi, J. S. (2010). Dust aerosol optical properties retrieval and radiative forcing over northwestern china during the 2008 china-u.s. joint field experiment. *Journal of Geophysical Research: Atmospheres*, 115(D7). Retrieved from <https://agupubs.onlinelibrary.wiley.com/doi/abs/10.1029/2009JD013263> doi: <https://doi.org/10.1029/2009JD013263>
- Ginoux, P., Prospero, J. M., Gill, T. E., Hsu, N. C., & Zhao, M. (2012). Global-scale attribution of anthropogenic and natural dust sources and their emission rates based on modis deep blue aerosol products. *Reviews of Geophysics*, 50(3).
- Gliß, J., Mortier, A., Schulz, M., Andrews, E., Balkanski, Y., Bauer, S. E., Benedictow, A. M., Bian, H., Checa-Garcia, R., Chin, M., Ginoux, P., Griesfeller, J. J., Heckel, A., Kipling, Z., Kirkevåg, A., Kokkola, H., Laj, P., Le Sager, P., Lund, M. T., Myhre, C. L., Matsui, H., Myhre, G., Neubauer, D., van Noije, T., North, P., Olivié, D. J. L., Rémy, S., Sogacheva, L., Takemura, T., Tsigaridis, K., & Tsyro, S. G. (2021). AeroCom phase iii multi-model evaluation of the aerosol life cycle and optical properties using ground-and space-based remote sensing as well as surface in situ observations. *Atmospheric Chemistry and Physics*, 21(1), 87–128. doi: 10.5194/acp-21-87-2021
- Gordon, I., Rothman, L., Hargreaves, R., Hashemi, R., Karlovets, E., Skinner, F., Conway, E., Hill, C., Kochanov, R., Tan, Y., Wcisło, P., Finenko, A., Nelson, K., Bernath, P., Birk, M., Boudon, V., Campargue, A., Chance, K., Coustenis, A., Drouin, B., Flaud, J.-M., Gamache, R., Hodges, J., Jacquemart, D., Mlawer, E., Nikitin, A., Perevalov, V., Rotger, M., Tennyson, J., Toon, G., Tran, H., Tyuterev, V., Adkins, E., Baker, A., Barbe, A., Canè, E., Császár, A., Dudaryonok, A., Egorov, O., Fleisher, A., Fleurbaey, H., Foltynowicz, A., Furtenbacher, T., Harrison, J., Hartmann, J.-M., Horneman, V.-M., Huang, X., Karman, T., Karns, J., Kass, S., Kleiner, I., Kofman, V., Kwabia-Tchana, F., Lavrentieva, N., Lee, T., Long, D., Lukashevskaya, A., Lyulin, O., Makhnev, V., Matt, W., Massie, S., Melosso, M., Mikhailenko, S., Mondelain, D., Müller, H., Naumenko, O., Perrin, A.,

- Polyansky, O., Raddaoui, E., Raston, P., Reed, Z., Rey, M., Richard, C., Tóbiás, R., Sadiék, I., Schwenke, D., Starikova, E., Sung, K., Tamassia, F., Tashkun, S., Vander Auwera, J., Vasilenko, I., Vigin, A., Villanueva, G., Vispoel, B., Wagner, G., Yachmenev, A., & Yurchenko, S. (2022). The hitran2020 molecular spectroscopic database. *Journal of Quantitative Spectroscopy and Radiative Transfer*, 277, 107949. Retrieved from <https://www.sciencedirect.com/science/article/pii/S0022407321004416> doi: <https://doi.org/10.1016/j.jqsrt.2021.107949>
- Goudie, A., & Middleton, N. (2001). Saharan dust storms: nature and consequences. *Earth-Science Reviews*, 56(1), 179-204. doi: 10.1016/S0012-8252(01)00067-8
- Gueymard, C. A. (2001). Parameterized transmittance model for direct beam and circum-solar spectral irradiance. *Solar Energy*, 71(5), 325-346. Retrieved from <https://www.sciencedirect.com/science/article/pii/S0038092X01000548> doi: [https://doi.org/10.1016/S0038-092X\(01\)00054-8](https://doi.org/10.1016/S0038-092X(01)00054-8)
- Haase, J., Ge, M., Vedel, H., & Calais, E. (2003). Accuracy and variability of gps tropospheric delay measurements of water vapor in the western mediterranean. *Journal of Applied Meteorology*, 42(11), 1547 - 1568. doi: 10.1175/1520-0450(2003)042<1547:AAVOGT>2.0.CO;2
- Hand, J. L., Mahowald, N. M., Chen, Y., Siefert, R. L., Luo, C., Subramaniam, A., & Fung, I. (2004). Estimates of atmospheric-processed soluble iron from observations and a global mineral aerosol model: Biogeochemical implications. *Journal of Geophysical Research D: Atmospheres*, 109(D17). doi: 10.1029/2004JD004574
- Hansell, R. A., Tsay, S.-C., Hsu, N. C., Ji, Q., Bell, S. W., Holben, B. N., Welton, E. J., Roush, T. L., Zhang, W., Huang, J., Li, Z., & Chen, H. (2012). An assessment of the surface longwave direct radiative effect of airborne dust in zhangye, china, during the asian monsoon years field experiment (2008). *Journal of Geophysical Research: Atmospheres*, 117(D16). Retrieved from <https://agupubs.onlinelibrary.wiley.com/doi/abs/10.1029/2011JD017370> doi: <https://doi.org/10.1029/2011JD017370>
- Haywood, J., Francis, P., Osborne, S., Glew, M., Loeb, N., Highwood, E., Tanré, D., Myhre, G., Formenti, P., & Hirst, E. (2003). Radiative properties and direct radiative effect of saharan dust measured by the c-130 aircraft during shade: 1. solar spectrum. *Journal of Geophysical Research: Atmospheres*, 108(D18). doi: 10.1029/2002JD002687
- Haywood, J. M., Allan, R. P., Culverwell, I., Slingo, T., Milton, S., Edwards, J., & Clerbaux, N. (2005). Can desert dust explain the outgoing longwave radiation anomaly over the sahara during july 2003? *Journal of Geophysical Research: Atmospheres*, 110(D5).
- Helmert, J., Heinold, B., Tegen, I., Hellmuth, O., & Wendisch, M. (2007). On the direct and semidirect effects of saharan dust over europe: A modeling study. *Journal of Geophysical Research: Atmospheres*, 112(D13). doi: 10.1029/2006JD007444
- Highwood, E. J., & Ryder, C. L. (2014). Radiative effects of dust. In P. Knippertz & J.-B. W. Stuut (Eds.), *Mineral dust: A key player in the earth system* (pp. 267–286). Springer Netherlands. doi: 10.1007/978-94-017-8978-3_11
- Hoffmann, C., Funk, R., Wieland, R., Li, Y., & Sommer, M. (2008). Effects of grazing and topography on dust flux and deposition in the xilingele grassland, inner mongolia. *Journal of Arid Environments*, 72(5), 792-807. Retrieved from <https://www.sciencedirect.com/science/article/pii/S0140196307002431> doi: <https://doi.org/10.1016/j.jaridenv.2007.07.002>

doi.org/10.1016/j.jaridenv.2007.09.004

- Holben, B., Eck, T., Slutsker, I., Tanré, D., Buis, J., Setzer, A., Vermote, E., Reagan, J., Kaufman, Y., Nakajima, T., Lavenu, F., Jankowiak, I., & Smirnov, A. (1998). Aeronet—a federated instrument network and data archive for aerosol characterization. *Remote Sensing of Environment*, 66(1), 1-16. Retrieved from <https://www.sciencedirect.com/science/article/pii/S0034425798000315> doi: [https://doi.org/10.1016/S0034-4257\(98\)00031-5](https://doi.org/10.1016/S0034-4257(98)00031-5)
- Hsu, N. C., Herman, J. R., & Weaver, C. (2000). Determination of radiative forcing of Saharan dust using combined TOMS and ERBE data. *Journal of Geophysical Research: Atmospheres*, 105(D16), 20649–20661. doi: 10.1029/2000JD900150
- Hsu, N. C., Jeong, M.-J., Bettenhausen, C., Sayer, A. M., Hansell, R., Seftor, C. S., Huang, J., & Tsay, S.-C. (2013). Enhanced deep blue aerosol retrieval algorithm: The second generation. *Journal of Geophysical Research: Atmospheres*, 118(16), 9296-9315. Retrieved from <https://agupubs.onlinelibrary.wiley.com/doi/abs/10.1002/jgrd.50712> doi: <https://doi.org/10.1002/jgrd.50712>
- Huang, Y., Adebisi, A. A., Formenti, P., & Kok, J. F. (2021). Linking the different diameter types of aspherical desert dust indicates that models underestimate coarse dust emission. *Geophysical Research Letters*, 48(6), e2020GL092054. doi: 10.1029/2020GL092054
- Huang, Y., Kok, J. F., Kandler, K., Lindqvist, H., Nousiainen, T., Sakai, T., Adebisi, A., & Jokinen, O. (2020). Climate models and remote sensing retrievals neglect substantial desert dust asphericity. *Geophysical Research Letters*, 47(6), e2019GL086592. doi: 10.1029/2019GL086592
- Huang, Y., Kok, J. F., Saito, M., & Muñoz, O. (2023). Single-scattering properties of ellipsoidal dust aerosols constrained by measured dust shape distributions. *Atmospheric Chemistry and Physics*, 23(4), 2557–2577. Retrieved from <https://acp.copernicus.org/articles/23/2557/2023/> doi: 10.5194/acp-23-2557-2023
- Huttunen, J., Arola, A., Myhre, G., Lindfors, A. V., Mielonen, T., Mikkonen, S., Schafer, J. S., Tripathi, S. N., Wild, M., Komppula, M., et al. (2014). Effect of water vapor on the determination of aerosol direct radiative effect based on the AERONET fluxes. *Atmospheric Chemistry and Physics*, 14(12), 6103–6110. doi: 10.5194/acp-14-6103-2014
- Iacono, M. J., Delamere, J. S., Mlawer, E. J., Shephard, M. W., Clough, S. A., & Collins, W. D. (2008). Radiative forcing by long-lived greenhouse gases: Calculations with the aer radiative transfer models. *Journal of Geophysical Research: Atmospheres*, 113(D13). Retrieved from <https://agupubs.onlinelibrary.wiley.com/doi/abs/10.1029/2008JD009944> doi: <https://doi.org/10.1029/2008JD009944>
- Imperial County Air Pollution Control District. (2018, April). *Imperial county 2018 annual particulate matter less than 2.5 microns in diameter state implementation plan* (Tech. Rep.). CARB and APCD. Retrieved from <https://apcd.imperialcounty.org/wp-content/uploads/2020/01/2018-IC-PM25SIP.pdf>
- Imperial Irrigation District. (2016, July). *Salton sea air quality mitigation program* (Tech. Rep.). Salton Sea Air Quality Team. Retrieved from <https://www.iid.com/Home/ShowDocument?id=11827>
- IPCC. (2014). *Climate change 2014: Synthesis report. contribution of working groups i, ii and iii to the fifth assessment report of the intergovernmental panel on climate change* (Core

- Writing Team, R. Pachauri, & L. Meyer, Eds.). Geneva, Switzerland.
- Ives, R. L. (1949). Climate of the sonoran desert region. *Annals of the Association of American Geographers*, 39(3), 143–187.
- Japan Meteorological Agency, Japan. (2013). *Jra-55: Japanese 55-year reanalysis, daily 3-hourly and 6-hourly data*. Boulder CO: Research Data Archive at the National Center for Atmospheric Research, Computational and Information Systems Laboratory. Retrieved from <https://doi.org/10.5065/D6HH6H41>
- Jickells, T., An, Z., Andersen, K. K., Baker, A., Bergametti, G., Brooks, N., Cao, J., Boyd, P., Duce, R., Hunter, K., et al. (2005). Global iron connections between desert dust, ocean biogeochemistry, and climate. *Science*, 308(5718), 67–71. doi: 10.1126/science.1105959
- Jin, Y., Kai, K., Kawai, K., Nagai, T., Sakai, T., Yamazaki, A., Uchiyama, A., Batdorj, D., Sugimoto, N., & Nishizawa, T. (2015). Ceilometer calibration for retrieval of aerosol optical properties. *Journal of Quantitative Spectroscopy and Radiative Transfer*, 153, 49-56. Retrieved from <https://www.sciencedirect.com/science/article/pii/S0022407314004257> doi: <https://doi.org/10.1016/j.jqsrt.2014.10.009>
- Johnson, B. T., Shine, K. P., & Forster, P. M. (2004). The semi-direct aerosol effect: Impact of absorbing aerosols on marine stratocumulus. *Quarterly Journal of the Royal Meteorological Society*, 130(599), 1407-1422. Retrieved from <https://rmets.onlinelibrary.wiley.com/doi/abs/10.1256/qj.03.61> doi: <https://doi.org/10.1256/qj.03.61>
- Jones, B. A., & Fleck, J. (2020). Shrinking lakes, air pollution, and human health: Evidence from california's salton sea. *Science of The Total Environment*, 712, 136490. Retrieved from <https://www.sciencedirect.com/science/article/pii/S0048969719364861> doi: <https://doi.org/10.1016/j.scitotenv.2019.136490>
- Journet, E., Balkanski, Y., & Harrison, S. P. (2014). A new data set of soil mineralogy for dust-cycle modeling. *Atmospheric Chemistry and Physics*, 14(8), 3801–3816. doi: 10.5194/acp-14-3801-2014
- Kanatani, K. T., Ito, I., Al-Delaimy, W. K., Adachi, Y., Mathews, W. C., Ramsdell, J. W., Itazawa, T., Ito, Y., Tamura, K., Shitano, Y., Murakami, G., Higuchi, O., Tsuji, T., Fuchizawa, T., & Yamamoto, J. (2010). Desert dust exposure is associated with increased risk of asthma hospitalization in children. *American Journal of Respiratory and Critical Care Medicine*, 182(12), 1475–1481. doi: 10.1164/rccm.201002-0296OC
- Kandler, K., Benker, N., Bundke, U., Cuevas, E., Ebert, M., Knippertz, P., Rodríguez, S., Schütz, L., & Weinbruch, S. (2007). Chemical composition and complex refractive index of saharan mineral dust at izaña, tenerife (spain) derived by electron microscopy. *Atmospheric Environment*, 41(37), 8058-8074. doi: 10.1016/j.atmosenv.2007.06.047
- Kandler, K., Schütz, L., Deutscher, C., Ebert, M., Hofmann, H., Jäckel, S., Jaenicke, R., Knippertz, P., Lieke, K., Massling, A., Petzold, A., Schladitz, A., Weinzierl, B., Wiedensohler, A., Zorn, S., & Weinbruch, S. (2009). Size distribution, mass concentration, chemical and mineralogical composition and derived optical parameters of the boundary layer aerosol at tinfou, morocco, during samum 2006. *Tellus B: Chemical and Physical Meteorology*, 61(1), 32-50. Retrieved from <https://doi.org/10.1111/j.1600-0889.2008.00385.x> doi: 10.1111/j.1600-0889.2008.00385.x
- Karam, D. B., Flamant, C., Knippertz, P., Reitebuch, O., Pelon, J., Chong, M., & Dabas, A. (2008). Dust emissions over the Sahel associated with the West African monsoon

- intertropical discontinuity region: A representative case-study. *Quarterly Journal of the Royal Meteorological Society*, 134, 621–634. doi: 10.1002/qj.244
- Key, J., & Schweiger, A. J. (1998). Tools for atmospheric radiative transfer: STREAMER and FLUXNET. *Computers and Geosciences*, 24(5), 443–451. doi: 10.1016/S0098-3004(97)00130-1
- Key, J., & Schweiger, A. J. (2013, 2 13). *Streamer* [Software v3.1]. Polar Meteorology and Climatology at CIMSS. Retrieved from <https://stratus.ssec.wisc.edu/streamer/>
- Knippertz, P., & Todd, M. C. (2010). The central west Saharan dust hot spot and its relation to African easterly waves and extratropical disturbances. *Journal of Geophysical Research: Atmospheres*, 115(D12). doi: 10.1029/2009JD012819
- Kok, J. F. (2011). A scaling theory for the size distribution of emitted dust aerosols suggests climate models underestimate the size of the global dust cycle. *Proceedings of the National Academy of Sciences*, 108(3), 1016–1021. doi: 10.1073/pnas.1014798108
- Kok, J. F., Ridley, D. A., Zhou, Q., Miller, R. L., Zhao, C., Heald, C. L., Ward, D. S., Albani, S., & Haustein, K. (2017). Smaller desert dust cooling effect estimated from analysis of dust size and abundance. *Nature Geoscience*, 10(4), 274–278. doi: 10.1038/NGEO2912
- Kok, J. F., Storelvmo, T., Karydis, V. A., Adebisi, A. A., Mahowald, N. M., Evan, A. T., He, C., & Leung, D. M. (2023). Mineral dust aerosol impacts on global climate and climate change. *Nature Reviews Earth & Environment*, 1–16. doi: 10.1038/s43017-022-00379-5
- Kok, J. F., Ward, D. S., Mahowald, N. M., & Evan, A. T. (2018). Global and regional importance of the direct dust-climate feedback. *Nature Communications*, 9(1), 241. Retrieved from <https://doi.org/10.1038/s41467-017-02620-y> doi: 10.1038/s41467-017-02620-y
- Kollath, D. R., Mihaljevic, J. R., & Barker, B. M. (2022). Pm10 and other climatic variables are important predictors of seasonal variability of coccidioidomycosis in arizona. *Microbiology Spectrum*, 10(2), e01483–21.
- Kuwano, A., & Evan, A. (2022). A method to account for the impact of water vapor on observation-based estimates of the clear-sky shortwave direct radiative effect of mineral dust. *Journal of Geophysical Research: Atmospheres*, 127(17), e2022JD036620. Retrieved from <https://agupubs.onlinelibrary.wiley.com/doi/abs/10.1029/2022JD036620> (e2022JD036620 2022JD036620) doi: <https://doi.org/10.1029/2022JD036620>
- Levy, R. C., Mattoo, S., Munchak, L. A., Remer, L. A., Sayer, A. M., Patadia, F., & Hsu, N. C. (2013). The collection 6 modis aerosol products over land and ocean. *Atmospheric Measurement Techniques*, 6(11), 2989–3034. doi: <https://doi.org/10.5194/amt-6-2989-2013>
- Li, F., Vogelmann, A., & Ramanathan, V. (2004). Saharan dust aerosol radiative forcing measured from space. *Journal of Climate*, 17(13), 2558–2571. doi: 10.1175/1520-0442(2004)017<2558:SDARFM>2.0.CO;2
- Li, L., Mahowald, N. M., Miller, R. L., Pérez García-Pando, C., Klose, M., Hamilton, D. S., Gonçalves Ageitos, M., Ginoux, P., Balkanski, Y., Green, R. O., Kalashnikova, O., Kok, J. F., Obiso, V., Paynter, D., & Thompson, D. R. (2021). Quantifying the range of the dust direct radiative effect due to source mineralogy uncertainty. *Atmospheric Chemistry and Physics*, 21(5), 3973–4005. doi: 10.5194/acp-21-3973-2021

- Liao, H., & Seinfeld, J. H. (1998). Radiative forcing by mineral dust aerosols: Sensitivity to key variables. *Journal of Geophysical Research: Atmospheres*, *103*(D24), 31637-31645. doi: 10.1029/1998JD200036
- Liu, H., Tang, S., Hu, J., Zhang, S., & Deng, X. (2017). An improved physical split-window algorithm for precipitable water vapor retrieval exploiting the water vapor channel observations. *Remote Sensing of Environment*, *194*, 366-378. Retrieved from <https://www.sciencedirect.com/science/article/pii/S0034425717301347> doi: <https://doi.org/10.1016/j.rse.2017.03.031>
- Loeb, N. G., & Kato, S. (2002). Top-of-atmosphere direct radiative effect of aerosols over the tropical oceans from the Clouds and the Earth's Radiant Energy System (CERES) satellite instrument. *Journal of Climate*, *15*(12), 1474-1484. doi: 10.1175/1520-0442(2002)015<1474:TOADRE>2.0.CO;2
- Loeb, N. G., Su, W., Doelling, D. R., Wong, T., Minnis, P., Thomas, S., & Miller, W. F. (2018). Earth's top-of-atmosphere radiation budget. *Reference Module in Earth Systems and Environmental Sciences*, *5*, 67-84. doi: 10.1016/B978-0-12-409548-9.10367-7
- Marcos, C. R., Gómez-Amo, J. L., Peris, C., Pedrós, R., Utrillas, M. P., & Martínez-Lozano, J. A. (2018). Analysis of four years of ceilometer-derived aerosol backscatter profiles in a coastal site of the western mediterranean. *Atmospheric Research*, *213*, 331-345. Retrieved from <https://www.sciencedirect.com/science/article/pii/S016980951830468X> doi: <https://doi.org/10.1016/j.atmosres.2018.06.016>
- Marshall, J. H., Hobby, M., Allen, C. J. T., Banks, J. R., Bart, M., Brooks, B. J., Cavazos-Guerra, C., Engelstaedter, S., Gascoyne, M., Lima, A. R., Martins, J. V., McQuaid, J. B., O'Leary, A., Ouchene, B., Ouladichir, A., Parker, D. J., Saci, A., Salah-Ferroudj, M., Todd, M. C., & Washington, R. (2013). Meteorology and dust in the central sahara: Observations from fennec supersite-1 during the june 2011 intensive observation period. *Journal of Geophysical Research: Atmospheres*, *118*(10), 4069-4089. doi: 10.1002/jgrd.50211
- Meador, W. E., & Weaver, W. R. (1980). Two-stream approximations to radiative transfer in planetary atmospheres: A unified description of existing methods and a new improvement. *Journal of Atmospheric Sciences*, *37*(3), 630-643. doi: 10.1175/1520-0469(1980)037<0630:TSATRT>2.0.CO;2
- Meloni, D., di Sarra, A., Di Iorio, T., & Fiocco, G. (2005). Influence of the vertical profile of saharan dust on the visible direct radiative forcing. *Journal of Quantitative Spectroscopy and Radiative Transfer*, *93*(4), 397-413. doi: 10.1016/j.jqsrt.2004.08.035
- Meng, J., Huang, Y., Leung, D. M., Li, L., Adebisi, A. A., Ryder, C. L., Mahowald, N. M., & Kok, J. F. (2022). Improved parameterization for the size distribution of emitted dust aerosols reduces model underestimation of super coarse dust. *Geophysical Research Letters*, *49*(8). Retrieved from <https://agupubs.onlinelibrary.wiley.com/doi/abs/10.1029/2021GL097287> doi: <https://doi.org/10.1029/2021GL097287>
- Mikofski, M. (2016, 7 26). *Solar position calculator*. Retrieved from [https://urldefense.com/v3/_https://www.mathworks.com/matlabcentral/fileexchange/58405-solar-position-calculator_;!!Mih3wA!DJTFWPku9aF9CseM91XbKf_UkAc3bTasfphULI27xLCY1yHAc_T9YLmcx0eQD3A1220R7yeIyP9IeK4\\$](https://urldefense.com/v3/_https://www.mathworks.com/matlabcentral/fileexchange/58405-solar-position-calculator_;!!Mih3wA!DJTFWPku9aF9CseM91XbKf_UkAc3bTasfphULI27xLCY1yHAc_T9YLmcx0eQD3A1220R7yeIyP9IeK4$)
- Minnis, P., Sun-Mack, S., Chen, Y., Khaiyer, M. M., Yi, Y., Ayers, J. K., Brown, R. R., Dong, X., Gibson, S. C., Heck, P. W., Lin, B., Nordeen, M. L., Nguyen, L., Palikonda, R.,

- Smith, W. L., Spangenberg, D. A., Trepte, Q. Z., & Xi, B. (2011). CERES edition-2 cloud property retrievals using TRMM VIRS and Terra and Aqua MODIS data—Part II: Examples of average results and comparisons with other data. *IEEE Transactions on Geoscience and Remote Sensing*, 49(11), 4401–4430. doi: 10.1109/TGRS.2011.2144602
- Minnis, P., Sun-Mack, S., Young, D. F., Heck, P. W., Garber, D. P., Chen, Y., Spangenberg, D. A., Arduini, R. F., Trepte, Q. Z., Smith, W. L., Ayers, J. K., Gibson, S. C., Miller, W. F., Hong, G., Chakrapani, V., Takano, Y., Liou, K.-N., Xie, Y., & Yang, P. (2011). CERES edition-2 cloud property retrievals using TRMM VIRS and Terra and Aqua MODIS data—Part I: Algorithms. *IEEE Transactions on Geoscience and Remote Sensing*, 49(11), 4374–4400. doi: 10.1109/TGRS.2011.2144601
- Minnis, P., Trepte, Q. Z., Sun-Mack, S., Chen, Y., Doelling, D. R., Young, D. F., Spangenberg, D. A., Miller, W. F., Wielicki, B. A., Brown, R. R., et al. (2008). Cloud detection in nonpolar regions for CERES using TRMM VIRS and Terra and Aqua MODIS data. *IEEE Transactions on Geoscience and Remote Sensing*, 46(11), 3857–3884. doi: 10.1109/TGRS.2008.2001351
- Mirzabaev, J., A. andd Wu, Evans, J., García-Oliva, F., Hussein, I., Iqbal, M., Kimutai, J., Knowles, T., Meza, F., Nedjraoui, D., Tena, F., Türkeş, M., Vázquez, R., & Weltz, M. (in press). 2019: Desertification. In P. Shukla et al. (Eds.), *Climate change and land: an ipcc special report on climate change, desertification, land degradation, sustainable land management, food security, and greenhouse gas fluxes in terrestrial ecosystems* (chap. 3).
- Mlawer, E., & Clough, S. (1997). On the extension of rapid radiative transfer model to the shortwave region. In *Proceedings of the 6th atmospheric radiation measurement (arm) science team meeting, us department of energy, conf-9603149* (Vol. 510).
- Mlawer, E., & Clough, S. (1998). Shortwave and longwave enhancements in the rapid radiative transfer model. In *Proceedings of the 7th atmospheric radiation measurement (arm) science team meeting* (pp. 409–413).
- Mlawer, E. J., Taubman, S. J., Brown, P. D., Iacono, M. J., & Clough, S. A. (1997). Radiative transfer for inhomogeneous atmospheres: Rrtm, a validated correlated-k model for the longwave. *Journal of Geophysical Research: Atmospheres*, 102(D14), 16663–16682. Retrieved from <https://agupubs.onlinelibrary.wiley.com/doi/abs/10.1029/97JD00237> doi: <https://doi.org/10.1029/97JD00237>
- Moore, J. K., & Braucher, O. (2008). Sedimentary and mineral dust sources of dissolved iron to the world ocean. *Biogeosciences*, 5(3), 631–656. doi: 10.5194/bg-5-631-2008
- Münkel, C., Eresmaa, N., Räsänen, J., & Karppinen, A. (2007). Retrieval of mixing height and dust concentration with lidar ceilometer. *Boundary-Layer Meteorology*, 124(1), 117–128. Retrieved from <https://doi.org/10.1007/s10546-006-9103-3> doi: 10.1007/s10546-006-9103-3
- NASA/LARC/SD/ASDC. (2014a). *CERES Single Scanner Footprint (SSF) TOA/Surface Fluxes, Clouds and Aerosols Aqua-FM3 Edition4A* [Dataset]. NASA Langley Atmospheric Science Data Center DAAC. Retrieved from https://ceres-tool.larc.nasa.gov/ord-tool/products?CERESProducts=SSFlevel12_Ed4 doi: 10.5067/AQUA/CERES/SSF-FM3_L2.004A
- NASA/LARC/SD/ASDC. (2014b). *CERES Single Scanner Footprint (SSF) TOA/Surface Fluxes, Clouds and Aerosols Aqua-FM3 edition4A*. NASA Langley Atmospheric Science Data

- Center DAAC. Retrieved from <https://subset.larc.nasa.gov/ceres/login.php> (Accessed on 2022-10-13) doi: 10.5067/AQUA/CERES/SSF-FM3_L2.004A
- NASA/LARC/SD/ASDC. (2014c). *CERES Single Scanner Footprint (SSF) TOA/Surface Fluxes, Clouds and Aerosols NOAA20-FM6-VIIRS Edition1B*. NASA Langley Atmospheric Science Data Center DAAC. Retrieved from <https://subset.larc.nasa.gov/ceres/login.php> (Accessed on 2022-10-27) doi: 10.5067/NOAA20/CERES/SSF-FM6_L2.001A
- NASA/LARC/SD/ASDC. (2014d). *CERES Single Scanner Footprint (SSF) TOA/Surface Fluxes, Clouds and Aerosols NPP-FM5 Edition4A*. NASA Langley Atmospheric Science Data Center DAAC. Retrieved from <https://subset.larc.nasa.gov/ceres/login.php> (Accessed on 2022-10-27) doi: 10.5067/NPP/CERES/SSF-FM5_L2.002A
- NASA/LARC/SD/ASDC. (2014e). *CERES Single Scanner Footprint (SSF) TOA/Surface Fluxes, Clouds and Aerosols Terra-FM1 edition4A*. NASA Langley Atmospheric Science Data Center DAAC. Retrieved from <https://subset.larc.nasa.gov/ceres/login.php> (Accessed on 2022-11-04) doi: 10.5067/TERRA/CERES/SSF_Terra-FM1_L2.004A
- NASA/LARC/SD/ASDC. (2014f). *CERES Single Scanner Footprint (SSF) TOA/Surface Fluxes, Clouds and Aerosols Terra-FM2 Edition4A [Dataset]*. NASA Langley Atmospheric Science Data Center DAAC. Retrieved from https://ceres-tool.larc.nasa.gov/ord-tool/products?CERESProducts=SSFlevel2_Ed4 doi: 10.5067/TERRA/CERES/SSF-FM2_L2.004A
- Okada, K., Heintzenberg, J., Kai, K., & Qin, Y. (2001). Shape of atmospheric mineral particles collected in three chinese arid-regions. *Geophysical Research Letters*, 28(16), 3123-3126. Retrieved from <https://agupubs.onlinelibrary.wiley.com/doi/abs/10.1029/2000GL012798> doi: <https://doi.org/10.1029/2000GL012798>
- Okin, G. S., Mahowald, N., Chadwick, O. A., & Artaxo, P. (2004). Impact of desert dust on the biogeochemistry of phosphorus in terrestrial ecosystems. *Global Biogeochemical Cycles*, 18(2). doi: 10.1029/2003GB002145
- Pappagianis, D., & Einstein, H. (1978). Tempest from tehachapi takes toll or coccidioides conveyed aloft and afar. *Western Journal of Medicine*, 129(6), 527.
- Parkinson, C. L. (2003). Aqua: An earth-observing satellite mission to examine water and other climate variables. *IEEE Transactions on Geoscience and Remote Sensing*, 41(2), 173–183. doi: 10.1109/TGRS.2002.808319
- Pinty, B., Roveda, F., Verstraete, M. M., Gobron, N., Govaerts, Y., Martonchik, J. V., Diner, D. J., & Kahn, R. A. (2000). Surface albedo retrieval from meteosat: 2. applications. *Journal of Geophysical Research: Atmospheres*, 105(D14), 18113-18134. doi: 10.1029/2000JD900114
- Poudel, U., Ahmad, S., & Stephen, H. (2021). Studying the intra-annual variability in surface area and volume of salton sea, california, using remote sensing-based water indices and gis. In *World environmental and water resources congress 2021* (p. 769-783). Retrieved from <https://ascelibrary.org/doi/abs/10.1061/9780784483466.070> doi: 10.1061/9780784483466.070
- Ramana, M. V., & Ramanathan, V. (2006). Abrupt transition from natural to anthropogenic aerosol radiative forcing: Observations at the abc-maldives climate observatory. *Journal of Geophysical Research: Atmospheres*, 111(D20). Retrieved from <https://agupubs>

- .onlinelibrary.wiley.com/doi/abs/10.1029/2006JD007063 doi: <https://doi.org/10.1029/2006JD007063>
- Roberts, A. J., & Knippertz, P. (2014). The formation of a large summertime saharan dust plume: Convective and synoptic-scale analysis. *Journal of Geophysical Research*, *119*, 1766–1785. doi: [10.1002/2013JD020667](https://doi.org/10.1002/2013JD020667)
- Roman, J., Knuteson, R., August, T., Hultberg, T., Ackerman, S., & Revercomb, H. (2016). A global assessment of nasa airs v6 and eumetsat iasi v6 precipitable water vapor using ground-based gps suominet stations. *Journal of Geophysical Research: Atmospheres*, *121*(15), 8925–8948. Retrieved from <https://agupubs.onlinelibrary.wiley.com/doi/abs/10.1002/2016JD024806> doi: <https://doi.org/10.1002/2016JD024806>
- Rosenfeld, D., Rudich, Y., & Lahav, R. (2001). Desert dust suppressing precipitation: A possible desertification feedback loop. *Proceedings of the National Academy of Sciences*, *98*(11), 5975–5980. Retrieved from <https://www.pnas.org/doi/abs/10.1073/pnas.101122798> doi: [10.1073/pnas.101122798](https://doi.org/10.1073/pnas.101122798)
- Ruiz-Arias, J. A., Dudhia, J., & Gueymard, C. A. (2014). A simple parameterization of the short-wave aerosol optical properties for surface direct and diffuse irradiances assessment in a numerical weather model. *Geoscientific Model Development*, *7*(3), 1159–1174. Retrieved from <https://gmd.copernicus.org/articles/7/1159/2014/> doi: [10.5194/gmd-7-1159-2014](https://doi.org/10.5194/gmd-7-1159-2014)
- Ryder, C. L., Highwood, E. J., Rosenberg, P. D., Trembath, J., Brooke, J. K., Bart, M., Dean, A., Crosier, J., Dorsey, J., Brindley, H., Banks, J., Marsham, J. H., McQuaid, J. B., Sodemann, H., & Washington, R. (2013). Optical properties of saharan dust aerosol and contribution from the coarse mode as measured during the fennec 2011 aircraft campaign. *Atmospheric Chemistry and Physics*, *13*(1), 303–325. Retrieved from <https://acp.copernicus.org/articles/13/303/2013/> doi: [10.5194/acp-13-303-2013](https://doi.org/10.5194/acp-13-303-2013)
- Ryder, C. L., Highwood, E. J., Walser, A., Seibert, P., Philipp, A., & Weinzierl, B. (2019). Coarse and giant particles are ubiquitous in saharan dust export regions and are radiatively significant over the sahara. *Atmospheric Chemistry and Physics*, *19*(24), 15353–15376. Retrieved from <https://acp.copernicus.org/articles/19/15353/2019/> doi: [10.5194/acp-19-15353-2019](https://doi.org/10.5194/acp-19-15353-2019)
- Ryder, C. L., Marengo, F., Brooke, J. K., Estelles, V., Cotton, R., Formenti, P., McQuaid, J. B., Price, H. C., Liu, D., Ausset, P., Rosenberg, P. D., Taylor, J. W., Choulaton, T., Bower, K., Coe, H., Gallagher, M., Crosier, J., Lloyd, G., Highwood, E. J., & Murray, B. J. (2018). Coarse-mode mineral dust size distributions, composition and optical properties from aer-d aircraft measurements over the tropical eastern atlantic. *Atmospheric Chemistry and Physics*, *18*(23), 17225–17257. Retrieved from <https://acp.copernicus.org/articles/18/17225/2018/> doi: [10.5194/acp-18-17225-2018](https://doi.org/10.5194/acp-18-17225-2018)
- Saito, M., & Yang, P. (2021a). Advanced bulk optical models linking the backscattering and microphysical properties of mineral dust aerosol. *Geophysical Research Letters*, *48*(17). doi: [10.1029/2021GL095121](https://doi.org/10.1029/2021GL095121)
- Saito, M., & Yang, P. (2021b). *TAMUdust2020* [Software v1.1.0]. Department of Atmospheric Sciences, Texas A&M University. Retrieved from <https://github.com/masasaito/TAMUdust2020#readme>
- Saito, M., Yang, P., Ding, J., & Liu, X. (2021). A comprehensive database of the optical properties

- of irregular aerosol particles for radiative transfer simulations. *Journal of the Atmospheric Sciences*, 78(7), 2089 - 2111. Retrieved from <https://journals.ametsoc.org/view/journals/atasc/78/7/JAS-D-20-0338.1.xml> doi: <https://doi.org/10.1175/JAS-D-20-0338.1>
- San Diego County Water Authority. (n.d.). *Quantification settlement agreement*. Retrieved 4/4/2022, from <https://www.sdcwa.org/sites/default/files/qa-fs.pdf>
- Sassen, K., DeMott, P. J., Prospero, J. M., & Poellot, M. R. (2003). Saharan dust storms and indirect aerosol effects on clouds: Crystal-face results. *Geophysical Research Letters*, 30(12). doi: 10.1029/2003GL017371
- Satheesh, S., & Ramanathan, V. (2000). Large differences in tropical aerosol forcing at the top of the atmosphere and earth's surface. *Nature*, 405(6782), 60. doi: 10.1038/35011039
- Scanza, R. A., Mahowald, N., Ghan, S., Zender, C. S., Kok, J. F., Liu, X., Zhang, Y., & Albani, S. (2015). Modeling dust as component minerals in the community atmosphere model: development of framework and impact on radiative forcing. *Atmospheric Chemistry and Physics*, 15(1), 537–561. doi: 10.5194/acp-15-537-2015
- Schweitzer, M. D., Calzadilla, A. S., Salamo, O., Sharifi, A., Kumar, N., Holt, G., Campos, M., & Mirsaiedi, M. (2018). Lung health in era of climate change and dust storms. *Environmental Research*, 163, 36–42. doi: 10.1016/j.envres.2018.02.001
- Seinfeld, J. H., & Pandis, S. N. (2016). *Atmospheric chemistry and physics: from air pollution to climate change*. John Wiley & Sons.
- Shao, Y. (2008).
In *Physics and modelling of wind erosion* (pp. 303–360). Springer. Retrieved from https://doi.org/10.1007/978-1-4020-8895-7_9 doi: 10.1007/978-1-4020-8895-7_9
- Shao, Y., Zhang, J., Ishizuka, M., Mikami, M., Leys, J., & Huang, N. (2020). Dependency of particle size distribution at dust emission on friction velocity and atmospheric boundary-layer stability. *Atmospheric Chemistry and Physics*, 20(21), 12939–12953. doi: 10.5194/acp-20-12939-2020
- Sokolik, I. N., & Toon, O. B. (1996). Direct radiative forcing by anthropogenic airborne mineral aerosols. *Nature*, 381(6584), 681–683. doi: 10.1038/381681a0
- Song, Q., Zhang, Z., Yu, H., Kato, S., Yang, P., Colarco, P., Remer, L. A., & Ryder, C. L. (2018). Net radiative effects of dust in the tropical North Atlantic based on integrated satellite observations and in situ measurements. *Atmospheric Chemistry and Physics*, 18(15), 11303–11322. doi: 10.5194/acp-18-11303-2018
- Song, Q., Zhang, Z., Yu, H., Kok, J. F., Di Biagio, C., Albani, S., Zheng, J., & Ding, J. (2022). Size-resolved dust direct radiative effect efficiency derived from satellite observations. *Atmospheric Chemistry and Physics*, 22(19), 13115–13135. Retrieved from <https://acp.copernicus.org/articles/22/13115/2022/> doi: 10.5194/acp-22-13115-2022
- Stamnes, K., Tsay, S.-C., Wiscombe, W., & Jayaweera, K. (1988). Numerically stable algorithm for discrete-ordinate-method radiative transfer in multiple scattering and emitting layered media. *Applied Optics*, 27(12), 2502–2509. doi: 10.1364/ao.27.002502
- Stephen, M. F., & Gorsline, D. S. (1975). Sedimentary aspects of the new river delta, salton sea, imperial county, california. , 267–282.
- Su, W., Corbett, J., Eitzen, Z., & Liang, L. (2015a). Next-generation angular distribution models

- for top-of-atmosphere radiative flux calculation from CERES instruments: Methodology. *Atmospheric Measurement Techniques*, 8(2), 611–632. doi: 10.5194/amt-8-611-2015
- Su, W., Corbett, J., Eitzen, Z., & Liang, L. (2015b). Next-generation angular distribution models for top-of-atmosphere radiative flux calculation from ceres instruments: validation. *Atmospheric Measurement Techniques*, 8(8), 3297–3313. Retrieved from <https://amt.copernicus.org/articles/8/3297/2015/> doi: 10.5194/amt-8-3297-2015
- Tanre, D. e. a. (1986). *Simulation of the satellite signal in the solar spectrum (5s)*. 262 pp.
- Tegen, I., Lacis, A. A., & Fung, I. (1996). The influence on climate forcing of mineral aerosols from disturbed soils. *Nature*, 380, 419–422. doi: 10.1038/380419a0
- Thompson, D. R., Braverman, A., Brodrick, P. G., Candela, A., Carmon, N., Clark, R. N., Connelly, D., Green, R. O., Kokaly, R. F., Li, L., et al. (2020). Quantifying uncertainty for remote spectroscopy of surface composition. *Remote Sensing of Environment*, 247, 111898.
- Tian, L., Chen, L., Zhang, P., & Bi, L. (2021). Estimating radiative forcing efficiency of dust aerosol based on direct satellite observations: case studies over the sahara and taklimakan desert. *Atmospheric Chemistry and Physics*, 21(15), 11669–11687. doi: 10.5194/acp-21-11669-2021
- Tong, D. Q., Wang, J. X., Gill, T. E., Lei, H., & Wang, B. (2017). Intensified dust storm activity and valley fever infection in the southwestern united states. *Geophysical research letters*, 44(9), 4304–4312.
- Tsay, S.-C., Stamnes, K., & Jayaweera, K. (1989). Radiative energy budget in the cloudy and hazy arctic. *Journal of Atmospheric Sciences*, 46(7), 1002-1018. doi: 10.1175/1520-0469(1989)046<1002:REBITC>2.0.CO;2
- Valenzuela, A., Olmo, F. J., Lyamani, H., Antón, M., Quirantes, A., & Alados-Arboledas, L. (2012). Aerosol radiative forcing during african desert dust events (2005–2010) over southeastern spain. *Atmospheric Chemistry and Physics*, 12(21), 10331–10351. Retrieved from <https://acp.copernicus.org/articles/12/10331/2012/> doi: 10.5194/acp-12-10331-2012
- van der Does, M., Knippertz, P., Zschenderlein, P., Harrison, R. G., & Stuut, J.-B. W. (2018). The mysterious long-range transport of giant mineral dust particles. *Science Advances*, 4(12), eaau2768. doi: 10.1126/sciadv.aau2768
- Voss, K. K., & Evan, A. T. (2019). *Dust aerosol optical depth* [Dataset]. PANGAEA. (Supplement to: Voss, KK; Evan, AT (2019): A new satellite-based global climatology of dust aerosol optical depth. *Journal of Applied Meteorology and Climatology*, <https://doi.org/10.1175/JAMC-D-19-0194.1>) doi: 10.1594/PANGAEA.909140
- Voss, K. K., & Evan, A. T. (2020). A new satellite-based global climatology of dust aerosol optical depth. *Journal of Applied Meteorology and Climatology*, 59(1), 83–102. doi: 10.1175/JAMC-D-19-0194.1
- Wagner, T. J., & Kleiss, J. M. (2016). Error characteristics of ceilometer-based observations of cloud amount. *Journal of Atmospheric and Oceanic Technology*, 33(7), 1557 - 1567. Retrieved from <https://journals.ametsoc.org/view/journals/atot/33/7/jtech-d-15-0258.1.xml> doi: <https://doi.org/10.1175/JTECH-D-15-0258.1>
- Walkowiak, B. (2022). *Estimates of the direct radiative effect of sonoran desert dust from origin soil mineralogy-a multi-model study* (Unpublished master's thesis). University of

California, San Diego.

- Wang, J., Zhang, L., Dai, A., Van Hove, T., & Van Baelen, J. (2007). A near-global, 2-hourly data set of atmospheric precipitable water from ground-based gps measurements. *Journal of Geophysical Research: Atmospheres*, *112*(D11). Retrieved from <https://agupubs.onlinelibrary.wiley.com/doi/abs/10.1029/2006JD007529> doi: <https://doi.org/10.1029/2006JD007529>
- Wang, W., Evan, A. T., Lavaysse, C., & Flamant, C. (2017). The role the Saharan Heat Low plays in dust emission and transport during summertime in North Africa. *Aeolian Research*, *28*, 1–12. doi: [10.1016/j.aeolia.2017.07.001](https://doi.org/10.1016/j.aeolia.2017.07.001)
- Ware, R. H., Fulker, D. W., Stein, S. A., Anderson, D. N., Avery, S. K., Clark, R. D., Droegemeier, K. K., Kuettner, J. P., Minster, J. B., & Sorooshian, S. (2000). Suominet: A real-time national gps network for atmospheric research and education. *Bulletin of the American Meteorological Society*, *81*(4), 677 - 694. doi: [10.1175/1520-0477\(2000\)081<0677:SARNGN>2.3.CO;2](https://doi.org/10.1175/1520-0477(2000)081<0677:SARNGN>2.3.CO;2)
- Weir-Brush, J. R., Garrison, V. H., Smith, G. W., & Shinn, E. A. (2004). The relationship between gorgonian coral (Cnidaria: Gorgonacea) diseases and African dust storms. *Aerobiologia*, *20*(2), 119–126. doi: [10.1023/B:AERO.0000032949.14023.3a](https://doi.org/10.1023/B:AERO.0000032949.14023.3a)
- Wielicki, B. A., Barkstrom, B. R., Harrison, E. F., Lee, R. B., Smith, G. L., & Cooper, J. E. (1996). Clouds and the Earth's Radiant Energy System (CERES): An Earth observing system experiment. *Bulletin of the American Meteorological Society*, *77*(5), 853–868. doi: [10.1175/1520-0477\(1996\)077<0853:CATERE>2.0.CO;2](https://doi.org/10.1175/1520-0477(1996)077<0853:CATERE>2.0.CO;2)
- Xia, X., & Zong, X. (2009). Shortwave versus longwave direct radiative forcing by taklimakan dust aerosols. *Geophysical research letters*, *36*(7).
- Xiong, X., Butler, J., Chiang, K., Efremova, B., Fulbright, J., Lei, N., McIntire, J., Oudrari, H., Sun, J., Wang, Z., & Wu, A. (2014). Viirs on-orbit calibration methodology and performance. *Journal of Geophysical Research: Atmospheres*, *119*(9), 5065-5078. Retrieved from <https://agupubs.onlinelibrary.wiley.com/doi/abs/10.1002/2013JD020423> doi: <https://doi.org/10.1002/2013JD020423>
- Yang, E.-S., Gupta, P., & Christopher, S. A. (2009). Net radiative effect of dust aerosols from satellite measurements over sahara. *Geophysical Research Letters*, *36*(18). doi: [10.1029/2009GL039801](https://doi.org/10.1029/2009GL039801)
- Yoshioka, M., Mahowald, N. M., Conley, A. J., Collins, W. D., Fillmore, D. W., Zender, C. S., & Coleman, D. B. (2007). Impact of desert dust radiative forcing on sahel precipitation: Relative importance of dust compared to sea surface temperature variations, vegetation changes, and greenhouse gas warming. *Journal of Climate*, *20*(8), 1445–1467.
- Zhang, J., & Christopher, S. A. (2003). Longwave radiative forcing of saharan dust aerosols estimated from modis, misr, and ceres observations on terra. *Geophysical Research Letters*, *30*(23). Retrieved from <https://agupubs.onlinelibrary.wiley.com/doi/abs/10.1029/2003GL018479> doi: <https://doi.org/10.1029/2003GL018479>
- Zhao, A., Ryder, C. L., & Wilcox, L. J. (2022). How well do the cmip6 models simulate dust aerosols? *Atmospheric Chemistry and Physics*, *22*(3), 2095–2119. Retrieved from <https://acp.copernicus.org/articles/22/2095/2022/> doi: [10.5194/acp-22-2095-2022](https://doi.org/10.5194/acp-22-2095-2022)
- Zhou, M., Yu, H., Dickinson, R., Dubovik, O., & Holben, B. (2005). A normalized description

of the direct effect of key aerosol types on solar radiation as estimated from aerosol robotic network aerosols and moderate resolution imaging spectroradiometer albedos. *Journal of Geophysical Research: Atmospheres*, 110(D19). doi: 10.1029/2005JD005909